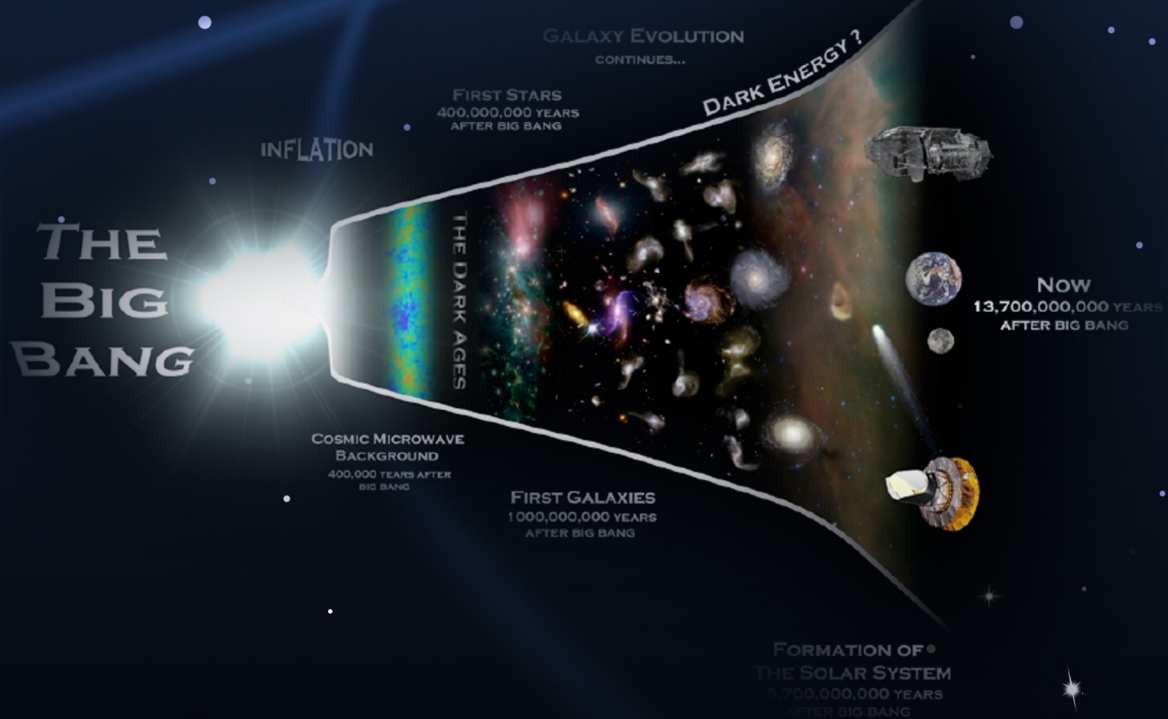


ESIC

Annual Report 2012



Elements Synthesis in Cosmos

创新研究群体

esic.ciae.ac.cn

Contents

Study of the primordial Lithium Abundances at CIAE -----	1
Determination of astrophysical $^{12}\text{N}(p, \gamma)^{13}\text{O}$ reaction rate from the $^2\text{H}(^{12}\text{N}, ^{13}\text{O})\text{n}$ reaction and its astrophysical implications -----	6
Study of the $^{22}\text{Na}+\text{p}$ Resonant Scattering at CRIB -----	20
Research status for the $^{12}\text{C} + ^{12}\text{C}$ fusion reaction in experiment -----	25
Nuclear uncertainties in s-process -----	35
Proton spectroscopic factor in ^9Be from the angular distribution of $^{13}\text{C}(^9\text{Be}, ^8\text{Li})^{14}\text{N}$ -----	43
Stellar neutron in laboratory -----	50
Study of the astrophysical $^4\text{He}(\text{np}, \gamma)^6\text{Li}$ reaction rate in a novel quasi-deuteron capture mechanism -----	54
Silicon abundances in nearby stars from the Si I infrared lines -----	58
Experimental study of key astrophysical $^{18}\text{Ne}(\alpha, \text{p})^{21}\text{Na}$ reaction -----	73

Study of the primordial Lithium Abundances at CIAE

Z. H. Li^{*†}, E. T. Li, J. Su, B. Guo, W. P. Liu, Y. J. Li, Y. S. Chen, S. Q. Hou, X. X. Bai, S. Q. Yan, Y. B. Wang, B. X. Wang, S. Zeng, G. Lian, X. Liu, S. J. Jin

China Institute of Atomic Energy, Beijing 102413, China

E-mail: zhli@ciae.ac.cn

(The present paper will be published in the conference proceedings of NIC2012.)

Lithium isotopes have attracted an intense interest because the abundances of both ^6Li and ^7Li from big bang nucleosynthesis (BBN) are the puzzles in nuclear astrophysics. Many investigations of astrophysical observation and BBN calculations have been carried out in order to solve the puzzles. Several nuclear reactions involving lithium have been determined at HI-13 tandem accelerator, Beijing, China. The BBN model calculations are then performed to investigate the primordial Lithium abundance. The result shows that these nuclear reactions have minimal effect on the primordial abundances of ^6Li and ^7Li .

Key Issues of Elements Synthesis in Cosmos

December, 2012

Beijing, China

^{*}Corresponding author.

[†]This work is supported by the National Natural Science Foundation of China under Grant Nos. 11021504 and 10975193, the National Basic Research Programme of China under Grant No. 2013CB834406.

1. Introduction

Since the pioneering work of M. Spite and F. Spite [1], the lithium abundance in the metal-poor halo stars was confirmed as a plateau, independent of metallicity and effective temperature. Up to now, the most widely accepted interpretation is that the lithium observed in metal-poor stars has been produced in the big bang nucleosynthesis (BBN). According to the standard Big Bang model, the relative abundances of the light elements (^1H , ^2H , ^3He , ^4He , ^6Li , and ^7Li) depend on only one parameter, namely, the baryon to photon ratio η . Using the precisely determined η from cosmic microwave background fluctuations, the lithium to hydrogen ratio is predicted to be $^7\text{Li}/\text{H} = (4.2 \pm 0.5) \times 10^{10}$ [2], which is higher than that observed in metal poor halo stars by roughly a factor of three. Even worse, the recent claims of detection of isotope-shifted Lithium absorption lines in a subset of the stars point to a ^6Li abundance some three orders of magnitude larger than that expected in BBN model [3].

In order to solve the Lithium problems from nuclear physics aspect, several nuclear reactions involving lithium, such as $^6\text{Li}(n, \gamma)^7\text{Li}$, $^7\text{Li}(n, \gamma)^8\text{Li}$, $^8\text{Li}(n, \gamma)^9\text{Li}$, $^6\text{Li}(p, \gamma)^7\text{Be}$, $^6\text{He}(p, \gamma)^7\text{Li}$, $^6\text{He}(p, n)^6\text{Li}$, $^6\text{He}(d, n)^7\text{Li}$, $^8\text{Li}(p, \gamma)^9\text{Be}$, $^8\text{Li}(p, d)^7\text{Li}$, $^8\text{Li}(p, t)^6\text{Li}$, $^8\text{Li}(d, p)^9\text{Li}$, $^8\text{Li}(d, n)^9\text{Be}$, $^7\text{Be}(d, ^3\text{He})^6\text{Li}$, and $^9\text{Be}(p, \alpha)^6\text{Li}$ were measured at HI-13 tandem accelerator, Beijing. The rates of these nuclear reactions were deduced and then used in the BBN network calculations.

2. Experiments

Figure 1 shows the reactions network of BBN, which is modified from the standard BBN model code [4]. The reactions labeled with the dashed line are determined at China institute of Atomic energy in about ten years.

The (n, γ) reactions were determined by the angular distributions of one neutron transfer reactions. Where, the $^6\text{Li}(n, \gamma)^7\text{Li}$ excitation function was deduced from the elastic transfer reaction of $^7\text{Li}(^6\text{Li}, ^7\text{Li})^6\text{Li}$ [5]. The $^6\text{Li}(n, \gamma)^7\text{Li}$ rates were derived to be $(8.1 \pm 0.6) \times 10^3 \text{ cm}^3 \text{ mol}^{-1} \text{ s}^{-1}$ at the energies of astrophysical interests. The angular distribution of $^{13}\text{C}(^7\text{Li}, ^8\text{Li})^{12}\text{C}$ was measured

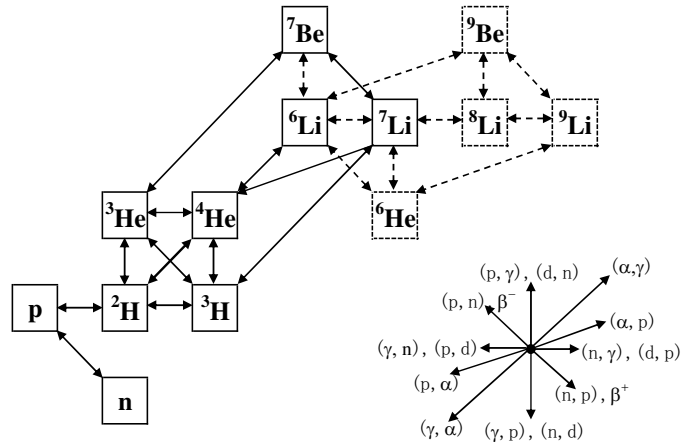


Figure 1: Reaction network for BBN calculation in the present work, as modified from Ref. [4].

and used to extract the ${}^8\text{Li}$ neutron spectroscopic factor with Distorted-Wave Born Approximation (DWBA) analysis. The ${}^7\text{Li}(n, \gamma){}^8\text{Li}$ cross sections are then deduced using the direct capture model calculations [6]. The angular distribution of the ${}^8\text{Li}(d, p){}^9\text{Li}$ reaction was measured at $E_{\text{c.m.}} = 7.8$ MeV in inverse kinematics using coincidence detection of ${}^9\text{Li}$ and the recoil proton. The neutron spectroscopic factor $S_{1,3/2}$ for ${}^9\text{Li} \rightarrow {}^8\text{Li} + n$ was derived to be 0.68 ± 0.14 . The astrophysical ${}^8\text{Li}(n, \gamma){}^9\text{Li}$ reaction rate for the direct capture was then deduced to be $3970 \pm 950 \text{ cm}^3 \text{mole}^{-1} \text{s}^{-1}$ at $T_9 = 1$ [7].

The (p, γ) reactions play important roles in nuclear astrophysics, but it is very difficult to measure directly since the small cross section at the energy of astrophysical interests. We determined the excitation function of (p, γ) by the measured angular distribution of one proton transfer reaction. The proton spectroscopic factor of ${}^7\text{Li}$ was extracted to be 0.42 ± 0.06 by the normalization of the calculated differential cross sections with the distorted-wave Born approximation to the measured ${}^2\text{H}({}^6\text{He}, {}^7\text{Li})n$ angular distribution [8]. The ${}^6\text{He}(p, \gamma){}^7\text{Li}$ cross section was then deduced with the newly extracted ${}^7\text{Li}$ proton spectroscopic factor [9]. According to charge symmetry of Mirror nuclei, we can deduce the proton spectroscopic factor from the neutron spectroscopic factor or the nuclear asymptotic normalization coefficient (ANC) of its mirror nucleus. The astrophysical ${}^6\text{Li}(p, \gamma){}^7\text{Be}$ S-factors were derived with the deduced ${}^7\text{Li}$ neutron spectroscopic factor from ${}^7\text{Li}({}^6\text{Li}, {}^7\text{Li}){}^6\text{Li}$ [5]. We determined the ${}^8\text{Li}(p, \gamma){}^9\text{Be}$ cross section by the angular distributions of ${}^2\text{H}({}^8\text{Li}, {}^9\text{Be})n$ and ${}^{13}\text{C}({}^9\text{Be}, {}^8\text{Li}){}^{14}\text{N}$. The spectroscopic factor of ${}^9\text{Be} = {}^8\text{Li} + p$ was extracted to be 0.64 ± 0.21 with the angular distribution of ${}^2\text{H}({}^8\text{Li}, {}^9\text{Be})n$ reaction in 2006 [10]. However, Camargo et al. extracted the proton spectroscopic factor of ${}^9\text{Be}$ to be 1.50 ± 0.28 with the measured angular distribution of ${}^9\text{Be}({}^8\text{Li}, {}^9\text{Be}){}^8\text{Li}$ elastic transfer reaction in 2008 [11]. Their value was larger than ours by a factor of 2. To clarify this dispersion, we measured the angular distribution of ${}^{13}\text{C}({}^9\text{Be}, {}^8\text{Li}){}^{14}\text{N}$ at HI-13 tandem accelerator this year, and the proton spectroscopic factor of ${}^9\text{Be}$ was extracted to be 0.72 ± 0.15 . The result proved the correctness of the ${}^9\text{Be}$ proton spectroscopic factor and ${}^8\text{Li}(p, \gamma){}^9\text{Be}$ cross section extracted from the ${}^2\text{H}({}^8\text{Li}, {}^9\text{Be})n$ reaction.

The ${}^4\text{He}(2n, \gamma){}^6\text{He}(p, n){}^6\text{Li}$ reactions were supposed to be a way to increase the primordial ${}^6\text{Li}$ abundance. The angular distributions of ${}^6\text{He}(p, n){}^6\text{Li}$ reaction leading to the ground and 3.563 MeV 0^+ states of ${}^6\text{Li}$ have been measured using the ${}^6\text{He}$ radioactive beam at energy of 4.17 AMeV [12]. The experiment reveals the proton-neutron halo structure of the secondary excited state of ${}^6\text{Li}$, which was predicted by Arai et al. [13]. The dependence of the cross section as a function of energy in the center of mass frame is calculated with the nuclear reaction code Talys [14]. In the similar way, the excitation functions of ${}^6\text{He}(d, n){}^7\text{Li}$, ${}^8\text{Li}(p, d){}^7\text{Li}$, ${}^8\text{Li}(p, t){}^6\text{Li}$, ${}^8\text{Li}(d, p){}^9\text{Li}$, ${}^8\text{Li}(d, n){}^9\text{Be}$, ${}^7\text{Be}(d, {}^3\text{He}){}^6\text{Li}$ were deduced by the measured cross section in inverse kinematics [8, 15, 7, 16].

The cross section of ${}^9\text{Be}(p, \alpha){}^6\text{Li}$ was extracted by means of the Trojan horse method (THM) using the ${}^2\text{H}({}^9\text{Be}, \alpha {}^6\text{Li})n$ reaction at a beam energy of 22.35 MeV [17]. In the analysis, ${}^9\text{Be} + {}^2\text{H} \rightarrow {}^9\text{Be} + p + n$ was assumed as an intermediate process in the quasifree condition, and the deuteron is used as "Trojan Horse" nucleus. The cross section relation between two-body and three-body reactions given by THM theory was applied to extract the energy dependance of the two body cross section. The $S(0)$ factor was then determined to be 21.0 ± 0.8 MeV b, which was in good agreement with the direct experiments [18, 19]. Furthermore, the electron screening potential energy U_e was also been extracted by comparing the direct and THM data [17].

3. Network calculations

With the cross sections of the above mentioned reactions, the thermonuclear reaction rates $\langle\sigma v\rangle$ can be calculated by

$$\langle\sigma v\rangle = \left[\frac{8}{\pi\mu} \right]^{1/2} [kT]^{-3/2} \int \sigma(E) E e^{-E/kT} dE, \quad (3.1)$$

where μ is the reduced mass of the system, E is the energy in the center of mass system, k is the Boltzmann constant, and T is the temperature in Kelvin.

The reaction network calculations have been done with the modification code based on the computational routines of Wagoner [4]. The rate for the abundance change of any nucleus i is determined by the rate equation

$$\frac{dY_i}{dt} = \sum_{i,k,l} N_i \left(-\frac{Y_i^{N_i} Y_j^{N_j}}{N_i! N_j!} [ij]_k + \frac{Y_l^{N_l} Y_k^{N_k}}{N_l! N_k!} [lk]_j \right), \quad (3.2)$$

where Y_i is the mass fraction contained in nucleus i , N_m is the number of nuclear m . $[ij]_k$ represents the reaction rate for the reaction between i and j , including the decay rate of nuclear i . The sum in Eq. (3.2) includes all reactions involving nucleus i .

The evolution of the abundance for ${}^6\text{Li}$, ${}^7\text{Li}$ and ${}^7\text{Be}$ of our calculations is shown in Figure 2. In general, it was found that the added reactions slightly changed the lithium abundance at $t < 1000$ s, but nearly no effect at $t > 1000$ s. This may be attributed to the small binding energies of lithium. The detailed study showed that ${}^6\text{Li}(p, \alpha){}^3\text{He}$ could have large effect for destroying ${}^6\text{Li}$, leading to the disappearance of the effect of the added reaction. The abundance of ${}^7\text{Li}$ is sensitive to the ${}^2\text{H}(p, \gamma){}^3\text{He}$, ${}^3\text{He}(\alpha, \gamma){}^7\text{Be}$, and ${}^7\text{Li}(p, \alpha){}^4\text{He}$ reaction rates. Unfortunately, the existing experimental data have large uncertainties.

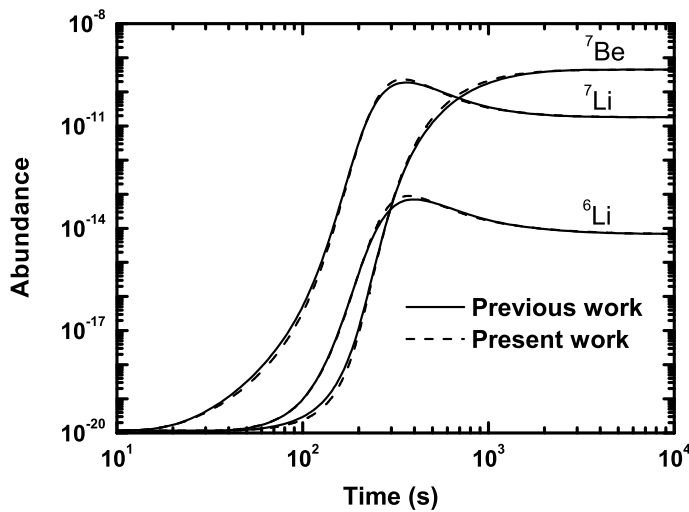


Figure 2: Nuclear abundance as a function of BBN times.

4. Conclusion and discussion

We have determined the rates of fourteen reactions involving lithium isotopes in the past ten years, and the BBN calculation with the expanded network shows that the attempts to solve the lithium abundance problem by measuring all the lithium involved reactions are failed. A series of fails indicates that the lithium puzzles may not be arisen from the determination of nuclear reaction rates, although some reactions, such as the reactions $^2\text{H}(p, \gamma)^3\text{He}$, $^3\text{He}(\alpha, \gamma)^7\text{Be}$ and $^7\text{Li}(p, \alpha)^4\text{He}$ mentioned above, need be determined more accurately.

It is very important to investigate the BBN model more carefully. The improvements of the lithium observations in very metal poor stars could also help us to solve the lithium problem. Very recently, J. C. Howk et al. reported their observation of interstellar lithium in the low-metallicity small Magellanic cloud [20]. The present-day ^7Li abundance is nearly equal to the BBN predictions. Measurements of ^6Li in stellar atmospheres are extremely difficult because the stellar line broadening is well in excess of the isotope shift. Their works give us a clue to understand the lithium puzzles.

References

- [1] M. Spite, F. Spite, *Nature*, **297** (1982) 483-485.
- [2] A. Coc, E. Vangioni-Flam, P. Descouvemont et al. *Astrophys J* **600** (2004) 544-552.
- [3] M. Asplund, D. L. Lambert, P. E. Nissen et al. *Astrophys J* **644** (2006) 229-259.
- [4] R. Wagoner, *Astrophys J* **18** (1969) 247-295.
- [5] J. Su, Z. H. Li, B. Guo et al. *Chin Phys Lett* **27** (2010) 052101.
- [6] Z. H. Li, B. Guo, Y. J. Li et al. *Plasma Science and Technology* **14** (2012) 488-491.
- [7] Z. H. Li, W. P. Liu, X. x. Bai et al. *Phys Rev C* **71** (2005) 052801(R).
- [8] Z. H. Li, E. T. Li, B. Guo et al. *Eur Phys J* **44** (2010) 1-5.
- [9] E. T. Li, Z. H. Li, J. Su et al. *Chin Phys Lett* **28** (2011) 052102.
- [10] J. Su, Z. H. Li, B. Guo et al. *Chin Phys Lett* **23** (2006) 55-57.
- [11] O. Camargo, V. Guimarães, R. Lichtenhäler et al. *Phys Rev C* **78** (2008) 034605.
- [12] Z. H. Li, W. P. Liu, X. X. Bai et al. *Phys Lett B* **527** (2002) 50-54.
- [13] K. Arai, Y. Suzuki, K. Varga, *Phys Rev C* **51** (1995) 2488-2493.
- [14] A. J. Koning, S. Hilaire, S. Goriely, *Nucl Phys A* **810** (2008) 13-76.
- [15] Y. J. Li, Z. H. Li, B. Guo et al. *Chin Phys Lett* **25** (2008) 455-457.
- [16] S. Zeng, W. P. Liu, Z. H. Li et al. *Chin Phys Lett* **22** (2005) 2219-2221.
- [17] Q. G. Wen, C. B. Li, S. H. Zhou et al. *Phys Rev C* **78** (2008) 035805.
- [18] A. J. Sierk and T. A. Tombrello, *Nucl Phys A* **210** (1973) 341-354.
- [19] D. Zahnow, C. Rolfs, S. Schmidt et al. *Z Phys A* **359** (1997) 211-218.
- [20] J. C. Howk, N. Lehner, B. D. Fields and G. J. Mathews, *Nature* **489** (2012) 121-123.

Determination of astrophysical $^{12}\text{N}(p, \gamma)^{13}\text{O}$ reaction rate from the $^2\text{H}(^{12}\text{N}, ^{13}\text{O})n$ reaction and its astrophysical implications

B. Guo^{1*}, J. Su¹, Z. H. Li¹, Y. B. Wang¹, S. Q. Yan¹, Y. J. Li¹, N. C. Shu¹, Y. L. Han¹, X. X. Bai¹, Y. S. Chen¹, W. P. Liu¹, H. Yamaguchi², D. N. Binh², T. Hashimoto², S. Hayakawa², D. Kahl², S. Kubono², J. J. He³, J. Hu³, S. W. Xu³, N. Iwasa⁴, N. Kume⁴, Z. H. Li⁵

¹China Institute of Atomic Energy, P.O. Box 275(10), Beijing 102413, China

²Center for Nuclear Study (CNS), the University of Tokyo, Wako Branch, 2-1 Hirosawa, Wako, Saitama 351-0198, Japan

³Institute of Modern Physics, Chinese Academy of Sciences (CAS), Lanzhou 730000, China

⁴Department of Physics, Tohoku University, 6-6 Aoba, Sendai, Miyagi 980-8578, Japan

⁵School of Physics and State Key Laboratory of Nuclear Physics and Technology, Peking University, Beijing 100871, China

The evolution of massive stars with very low-metallicities depends critically on the amount of CNO nuclides which they produce. The $^{12}\text{N}(p, \gamma)^{13}\text{O}$ reaction is an important branching point in the rap-processes, which are believed to be alternative paths to the slow 3α process for producing CNO seed nuclei and thus could change the fate of massive stars. In the present work, the angular distribution of the $^2\text{H}(^{12}\text{N}, ^{13}\text{O})n$ proton transfer reaction at $E_{\text{c.m.}} = 8.4$ MeV has been measured for the first time. Based on the Johnson-Soper approach, the square of the asymptotic normalization coefficient (ANC) for the virtual decay of $^{13}\text{O}_{\text{g.s.}} \rightarrow ^{12}\text{N} + p$ was extracted to be 3.92 ± 1.47 fm $^{-1}$ from the measured angular distribution and utilized to compute the direct component in the $^{12}\text{N}(p, \gamma)^{13}\text{O}$ reaction. The direct astrophysical S-factor at zero energy was then found to be 0.39 ± 0.15 keV b. By considering the direct capture into the ground state of ^{13}O , the resonant capture via the first excited state of ^{13}O and their interference, we determined the total astrophysical S-factors and rates of the $^{12}\text{N}(p, \gamma)^{13}\text{O}$ reaction. The new rate is two orders of magnitude slower than that from the REACLIB compilation. Our reaction network calculations with the present rate imply that $^{12}\text{N}(p, \gamma)^{13}\text{O}$ will only compete successfully with the β^+ decay of ^{12}N at higher (\sim two orders of magnitude) densities than initially predicted.

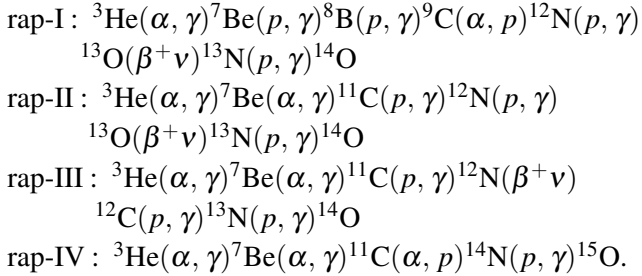
Key Issues of Elements Synthesis in Cosmos
December, 2012
Beijing, China

*Corresponding author.

1. Introduction

The first generation of stars formed at the end of the cosmic dark ages, which marked the key transition from a homogeneous and simple universe to a highly structured and complex one [1]. The first stars of zero metallicity are so-called Population III that formed before Population I in galactic disks and Population II in galactic halos [2, 3]. The most fundamental question about Population III stars is how massive they typically were since the mass of stars dominates their fundamental properties such as lifetimes, structures and evolutions. Recent numerical simulations of the collapse and fragmentation of primordial gas clouds indicate that these stars are predominantly very massive with masses larger than hundreds of M_{\odot} (see Ref. [1] and references therein).

A classic question on the evolution of supermassive stars is whether they contributed any significant material to later generations of stars by supernova explosions which ended the lives of Population III stars. In 1986, Fuller, Woosley and Weaver [4] studied the evolution of non-rotating supermassive stars with a hydrodynamic code KEPLER. They concluded that these stars will collapse into black holes without experiencing a supernova explosion. This is because the triple alpha process ($3\alpha \rightarrow ^{12}\text{C}$) does not produce sufficient amounts of CNO seed nuclei so that the hot CNO cycle and rp -process are unable to generate the nuclear energy enough to explode the stars. In 1989, Wiescher, Görres, Graff et al. [5] suggested the rap-processes as alternative paths which would permit these stars to bypass the 3α process and to yield the CNO material. The reactions involved in the rap-processes are listed as below:



It is crucial to determine the rates of the key reactions in the rap-processes in order to study if they play any significant role in the evolution of supermassive stars by producing CNO material. ${}^{12}\text{N}(p, \gamma){}^{13}\text{O}$ is an important reaction in the rap-I and rap-II processes.

Due to the low Q-value (1.516 MeV) of the ${}^{12}\text{N}(p, \gamma){}^{13}\text{O}$ reaction, its stellar reaction rate is dominated by the direct capture into the ground state in ${}^{13}\text{O}$. In addition, the resonant capture via the first excited state in ${}^{13}\text{O}$ could play an important role for determining the reaction rates. In 1989, Wiescher et al. [5] derived the direct astrophysical S-factor at zero energy, $S(0)$, to be ~ 40 keV b based on a shell model calculation. In 2006, Li [6] extracted the direct $S(0)$ factor to be 0.31 keV b by using the spectroscopic factor from the shell model calculation of Ref. [7], where the proton-removal cross section of ${}^{13}\text{O}$ on a Si target was well reproduced. It should be noted that there is a discrepancy of two orders of magnitude between the above two values of the direct $S(0)$ factor. In 2009, Banu, Al-Abdullah, Fu et al. [8] derived the asymptotic normalization coefficient (ANC) for the virtual decay of ${}^{13}\text{O}_{\text{g.s.}} \rightarrow {}^{12}\text{N} + p$ from the measurement of the ${}^{14}\text{N}({}^{12}\text{N}, {}^{13}\text{O}){}^{13}\text{C}$ angular distribution and then calculated the direct $S(0)$ factor to be 0.33 ± 0.04 keV b, which is consistent with that in Ref. [6]. As for the resonant capture component, the resonant parameters of the first excited state in ${}^{13}\text{O}$ have been studied through a thick target technique [9, 10] and R -matrix

method [10, 8]. In 1989, Wiescher et al. [5] derived the radiative width to be $\Gamma_\gamma = 24$ meV with one order of magnitude uncertainty based on a Weisskopf estimate of the transition strength. In 2007, Skorodumov, Rogachev, Boutachkov et al. [10] measured the excitation function of the resonant elastic scattering of $^{12}\text{N} + p$ and extracted the spin and parity to be $J^\pi = 1/2^+$ for the first excited state in ^{13}O via an *R*-matrix analysis. In addition, the excitation energy and the proton width were determined to be 2.69 ± 0.05 MeV and 0.45 ± 0.10 MeV, respectively. In 2009, Banu et al. [8] derived a radiative width $\Gamma_\gamma = 0.95$ eV by using the experimental ANC, based on the *R*-matrix approach.

This work aims at determining the astrophysical S-factors and rates of the $^{12}\text{N}(p, \gamma)^{13}\text{O}$ reaction through the ANC approach based on an independent proton transfer reaction. Here, the angular distribution of the $^{12}\text{N}(d, n)^{13}\text{O}$ reaction leading to the ground state in ^{13}O is measured in inverse kinematics, and used to extract the ANC for the virtual decay of $^{13}\text{O}_{\text{g.s.}} \rightarrow ^{12}\text{N} + p$ through the Johnson-Soper adiabatic approximation [11]. The (d, n) transfer system has been successfully applied to the study of some proton radiative capture reactions, such as $^7\text{Be}(p, \gamma)^8\text{B}$ [12, 13], $^8\text{B}(p, \gamma)^9\text{C}$ [14], $^{11}\text{C}(p, \gamma)^{12}\text{N}$ [15], and $^{13}\text{N}(p, \gamma)^{14}\text{O}$ [16]. The astrophysical S-factors and rates for the direct capture in the $^{12}\text{N}(p, \gamma)^{13}\text{O}$ reaction are then calculated by using the measured ANC. Finally, we obtain the total S-factors and rates by taking into account the direct capture, the resonant capture and their interference, and study the temperature-density conditions at which the $^{12}\text{N}(p, \gamma)^{13}\text{O}$ reaction takes place.

2. Measurement of the $^2\text{H}(^{12}\text{N}, ^{13}\text{O})n$ angular distribution

The experiment was performed with the CNS low energy in-flight Radio-Isotope Beam (CRIB) separator [17, 18] in the RIKEN RI Beam Factory (RIBF). A ^{10}B primary beam with an energy of 82 MeV was extracted from the AVF cyclotron. The primary beam impinged on a ^3He gas target with a pressure of 360 Torr and a temperature of 90 K; the target gas was confined in a small chamber with a length of 80 mm [19]. The front and rear windows of the gas chamber are Havar foils, each in a thickness of 2.5 μm . The secondary ^{12}N ions with an energy of 70 MeV were produced through the $^3\text{He}(^{10}\text{B}, ^{12}\text{N})n$ reaction and then selected by the CRIB separator, which mainly consists of two magnetic dipoles and a velocity filter (Wien filter).

A schematic layout of the experimental setup at the secondary reaction chamber (namely F3 chamber, see Ref. [18] for details) of CRIB separator is shown in Fig. 1. The cocktail beam which included ^{12}N was measured event-by-event using two parallel plate avalanche counters (PPACs) [20]; in this way, we determined the particle identification, precise timing information, and could extrapolate the physical trajectory of each ion in real space. In Fig. 2 we display the histogram of time of flight (TOF) vs. horizontal position (X) on the upstream PPAC in the F3 chamber for the particle identification of the cocktail beam. The main contaminants are ^7Be ions with the similar magnetic rigidities and velocities to the ^{12}N ions of interest. After the two PPACs, the ^{12}N secondary beam bombarded a deuterated polyethylene (CD_2) film with a thickness of 1.5 mg/cm^2 to study the $^2\text{H}(^{12}\text{N}, ^{13}\text{O})n$ reaction. A carbon film with a thickness of 1.5 mg/cm^2 was utilized to evaluate the background contribution from the carbon nuclei in the (CD_2) target. The target stand with a diameter of 8 mm also served as a beam collimator. The typical purity and intensity of the ^{12}N ions on target were approximately 30% and 500 pps after the collimator, respectively.

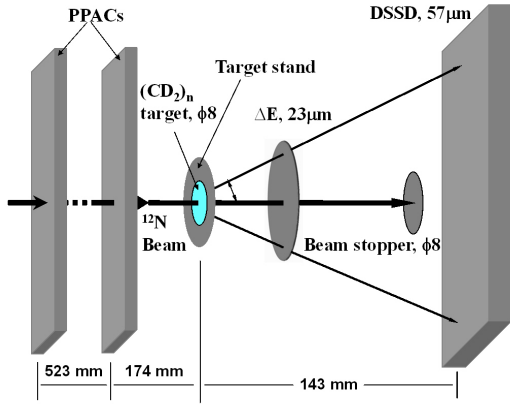


Figure 1: (Color online) Schematic layout of the experimental setup at the secondary reaction chamber (namely F3 chamber in Ref. [18]) of CRIB for the $^2\text{H}({}^{12}\text{N}, {}^{13}\text{O}_{\text{g.s.}})n$ reaction.

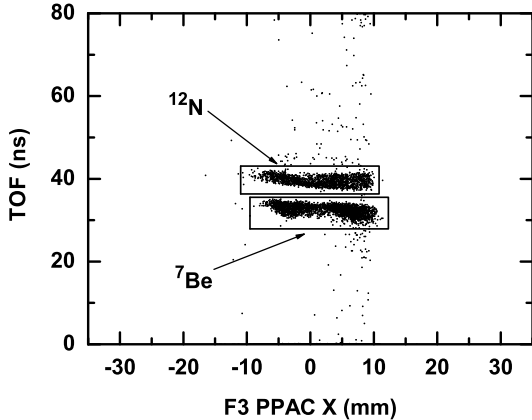


Figure 2: Two-dimensional histogram of TOF vs. horizontal position (X) on the upstream PPAC in the F3 chamber for the particle identification of the cocktail beam.

The ${}^{13}\text{O}$ reaction products were detected and identified with a telescope consisting of a $23\ \mu\text{m}$ silicon detector (ΔE) and a $57\ \mu\text{m}$ double-sided silicon strip detector (DSSD). In order to determine the energy of ${}^{12}\text{N}$ ions after they pass through two PPACs, a silicon detector with a thickness of $1500\ \mu\text{m}$ was placed between the downstream PPAC and the (CD_2) target, and removed after measuring the beam energy. The energy calibration of the detectors was carried out by combining the use of α -source and the magnetic rigidity parameters of ${}^{10}\text{B}$ and ${}^{12}\text{N}$ ions. The energy loss of the ${}^{12}\text{N}$ beam in the whole target was determined from the energy difference measured with and without the target. The ${}^{12}\text{N}$ beam energy in the middle of the (CD_2) target was derived to be $59\ \text{MeV}$ from the energy loss calculation by the program LISE++ [21], which was calibrated by the experimental energy loss in the whole target. In addition, a beam stopper (close to the DSSD) with a diameter of $8\ \text{mm}$ was used to block un-reacted beam particles in order to reduce radiation damage to the DSSD.

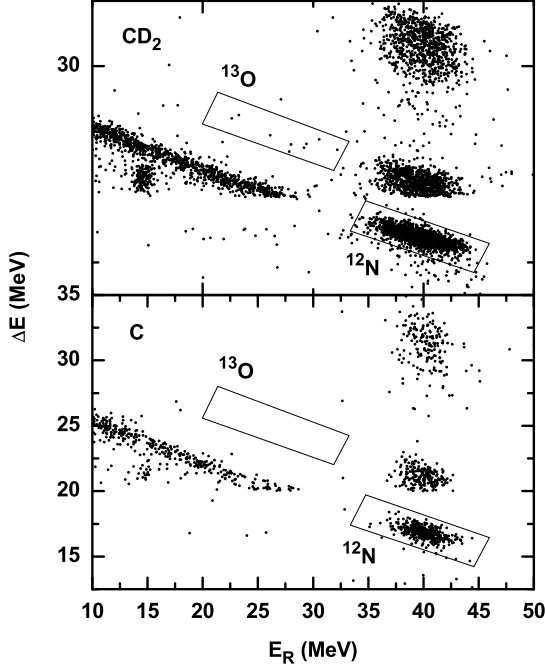


Figure 3: Two-dimensional histogram of energy loss ΔE vs. residual energy E_R for the events in the angular range of $3^\circ < \theta_{\text{c.m.}} < 4^\circ$. The top and bottom panels display the spectra for the measurement of the deuterated polyethylene (CD₂) and carbon (C) targets, respectively. The two-dimensional cuts for the ^{13}O events from the $^2\text{H}(^{12}\text{N}, ^{13}\text{O})n$ reaction were determined with a MC simulation. See text for details.

The emission angles of reaction products were determined by combining the position information from the DSSD and the two PPACs. As an example, Fig. 3 shows a two-dimensional histogram of energy loss (ΔE) vs. residual energy (E_R) for the events in the angular range of $3^\circ < \theta_{\text{c.m.}} < 4^\circ$. For the sake of saving CPU time in dealing with the experimental data, all the events below $\Delta E = 20$ MeV were scaled down by a factor of 100, and the ^{13}O events were not affected. The two-dimensional cuts of the ^{13}O events from the $^2\text{H}(^{12}\text{N}, ^{13}\text{O})n$ reaction were determined with a Monte Carlo (MC) simulation, which took into account the kinematics, geometrical factor, the energy diffusion of the ^{12}N beam, the angular straggling, and the energy straggling in the two PPACs, the secondary target and the ΔE detector. This simulation was calibrated by using the ^{12}N elastic scattering on the target. Such a calibration approach has been successfully used to study the $^2\text{H}(^8\text{Li}, ^9\text{Li})^1\text{H}$ reaction [22]. The ^{13}O events are clearly observed in the two-dimensional cut for the (CD₂) measurement, while no relevant events are observed in this cut for the background measurement. The ^7Be contaminants don't affect the identification of the ^{13}O events since these ions and their products are far from the ^{13}O region in the spectra of ΔE vs. E_R and have significantly different energies from the ^{13}O events. The effects of the pileup of ^7Be with ^{12}N can be estimated and subtracted through the background measurement. In addition, the detection efficiency correction from the beam stopper was also computed via the MC simulation also by considering the effects mentioned above. The resulting detection efficiencies range from 66% to 100% for different detection regions in the DSSD. After the beam normalization and background subtraction,

the angular distribution of the ${}^2\text{H}({}^{12}\text{N}, {}^{13}\text{O}_{\text{g.s.}})n$ reaction in the center of mass frame was obtained and is shown in Fig. 4.

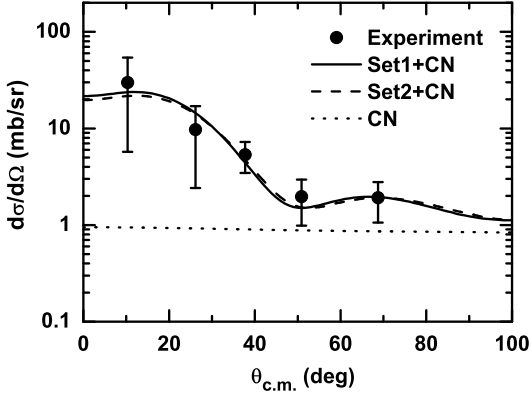


Figure 4: Measured angular distribution of ${}^2\text{H}({}^{12}\text{N}, {}^{13}\text{O}_{\text{g.s.}})n$ at $E_{\text{c.m.}} = 8.4$ MeV, together with the theoretical calculations on the direct-process contribution using two sets of optical potentials (Set1 and Set2) and the compound-nucleus (CN) contribution. See the text in the section for the details on the theoretical calculations.

3. Analysis of the ${}^2\text{H}({}^{12}\text{N}, {}^{13}\text{O})n$ angular distribution

For a peripheral transfer reaction, the ANC can be derived by the comparison of the experimental angular distribution with theoretical calculations,

$$\left(\frac{d\sigma}{d\Omega}\right)_{\text{exp}} = \sum_{j_i j_f} (C_{l_i j_i}^d)^2 (C_{l_f j_f}^{{}^{13}\text{O}})^2 R_{l_i j_i l_f j_f}, \quad (3.1)$$

where

$$R_{l_i j_i l_f j_f} = \frac{\sigma_{l_i j_i l_f j_f}^{th}}{(b_{l_i j_i}^d)^2 (b_{l_f j_f}^{{}^{13}\text{O}})^2}. \quad (3.2)$$

$(\frac{d\sigma}{d\Omega})_{\text{exp}}$ and $\sigma_{l_i j_i l_f j_f}^{th}$ are the experimental and theoretical differential cross sections, respectively. $C_{l_f j_f}^{{}^{13}\text{O}}$, $C_{l_i j_i}^d$ and $b_{l_f j_f}^{{}^{13}\text{O}}$, $b_{l_i j_i}^d$ represent the nuclear ANCs and the corresponding single particle ANCs for the virtual decays of ${}^{13}\text{O}_{\text{g.s.}} \rightarrow {}^{12}\text{N} + p$ and $d \rightarrow p + n$, respectively. l_i , j_i and l_f , j_f denote the orbital and total angular momenta of the transferred proton in the initial and final nuclei d and ${}^{13}\text{O}$, respectively. $R_{l_i j_i l_f j_f}$ is model independent in the case of a peripheral transfer reaction; therefore, the extraction of the ANC is insensitive to the geometric parameters (radius r_0 and diffuseness a) of the bound state potential.

In this work, the code FRESCO [23] was used to analyze the experimental angular distribution. In order to include the breakup effects of deuterons in the entrance channel, the angular distribution was calculated within the Johnson-Soper adiabatic approximation to the neutron, proton, and target three-body system [11]. In the present calculation, the optical potentials of nucleon-target

Table 1: Optical potential parameters used in the calculation, where V and W are in MeV, r and a in fm.

Set No.	1 [24]		2 [25]	
Channel	Entrance	Exit	Entrance	Exit
V_r	97.03	53.44	99.84	55.44
r_{0r}	1.152	1.154	1.127	1.131
a_r	0.722	0.69	0.708	0.676
W	1.73		0.86	0.77
r_w	1.693		1.693	1.131
a_w	0.716		0.711	0.676
W_s	14.01	9.61	14.2	9.54
r_{0s}	1.147	1.147	1.306	1.306
a_s	0.716	0.716	0.56	0.56
V_{so}	5.9	5.9	5.65	5.65
r_{0so}	0.816	0.83	0.903	0.907
a_{so}	0.661	0.63	0.622	0.622
r_{0c}	1.25		1.25	

were taken from Refs. [24, 25], which have been successfully applied to the study of some of the reactions on light nuclei [26, 27, 28]. The theoretical angular distributions of the direct process were calculated with these two sets of optical potentials, as shown in Fig. 4. The employed optical potential parameters are listed in Table 1. In addition, the UNF code [29] was used to evaluate the compound-nucleus (CN) contribution in the $^2\text{H}(^{12}\text{N}, ^{13}\text{O}_{\text{g.s.}})n$ reaction, as indicated by the dotted line in Fig. 4. The single-particle bound state wave functions were calculated with conventional Woods-Saxon potentials whose depths were adjusted to reproduce the binding energies of the proton in the ground states of the deuteron ($E_b = 2.225$ MeV) and ^{13}O ($E_b = 1.516$ MeV). To verify if the transfer reaction is peripheral, the ANC s and the spectroscopic factors were computed by changing the geometric parameters of Woods-Saxon potential for single-particle bound state, using one set of the optical potential, as displayed in Fig. 5. One sees that the spectroscopic factors depend significantly on the selection of the geometric parameters, while the ANC is nearly constant, indicating that the $^2\text{H}(^{12}\text{N}, ^{13}\text{O}_{\text{g.s.}})n$ reaction at the present energy is dominated by the peripheral process.

The spins and parities of $^{12}\text{N}_{\text{g.s.}}$ and $^{13}\text{O}_{\text{g.s.}}$ are 1^+ and $3/2^-$, respectively. Therefore, the $^2\text{H}(^{12}\text{N}, ^{13}\text{O}_{\text{g.s.}})n$ cross section could include two contributions from the proton transfers to $1p_{3/2}$ and $1p_{1/2}$ orbits in ^{13}O . The ratio of $1p_{3/2}:1p_{1/2}$ [$(C_{p_{3/2}}^{13}\text{O})^2/(C_{p_{1/2}}^{13}\text{O})^2$] was derived to be 0.16 based on a shell model calculation [7]. C_d^2 was taken to be 0.76 fm^{-1} from Ref. [30]. After the subtraction of the CN contribution, the first three data points at forward angles were used to derive the ANC by the comparison of the experimental data with the theoretical calculations. For one set of optical potential, three ANCs can be obtained by using three data points, and their weighted mean was then taken as the final value. The square of the ANCs for the $1p_{1/2}$ and $1p_{3/2}$ orbits were extracted to be $(C_{p_{1/2}}^{13}\text{O})^2 = 3.38 \pm 1.27 \text{ fm}^{-1}$ and $(C_{p_{3/2}}^{13}\text{O})^2 = 0.54 \pm 0.20 \text{ fm}^{-1}$, respectively. Consequently, the

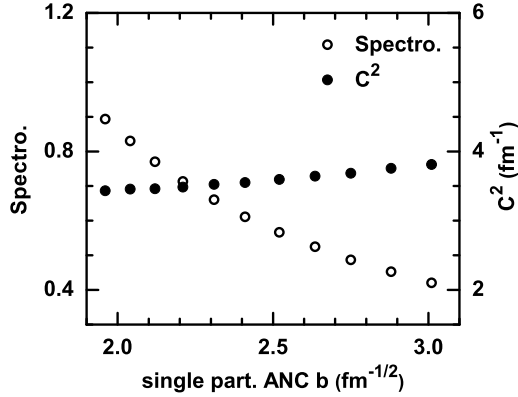


Figure 5: Variation of the spectroscopic factor (Spectro.) and the square of the ANC (C^2) for the virtual decay of $^{13}\text{O}_{\text{g.s.}} \rightarrow ^{12}\text{N} + p$ as a function of the single particle ANC b .

square of total ANC was $(C_{\text{tot}}^{13}\text{O})^2 = 3.92 \pm 1.47 \text{ fm}^{-1}$. The error resulted from the measurement (36%) and the uncertainty of the optical potentials (12%). This result is in agreement with the value of $(C_{p_{1/2}}^{13}\text{O})^2 = 2.53 \pm 0.30 \text{ fm}^{-1}$ obtained from the $^{14}\text{N}(^{12}\text{N}, ^{13}\text{O})^{13}\text{C}$ reaction [8].

4. Astrophysical rate of the $^{12}\text{N}(p, \gamma)^{13}\text{O}$ reaction and its astrophysical implications

The ANC, which defines the amplitude of the tail of the radial overlap function, determines the overall normalization of the direct astrophysical S-factors [31]. In the present work, the direct capture cross sections and astrophysical S-factors were computed based on the measured ANC by using the RADCAP code [32], which is a potential model tool for direct capture reactions. The resulting direct astrophysical S-factors as a function of $E_{\text{c.m.}}$ are displayed in Fig. 6, as indicated by the dashed line. The S-factor at zero energy was then found to be $S(0) = 0.39 \pm 0.15 \text{ keV b}$, which agrees with the values in Refs. [6, 8].

The astrophysical S-factors of the resonant capture can be obtained by using Breit-Wigner formula. In the present calculation, the resonant parameters ($J^\pi = 1/2^+$, $E_x = 2.69 \pm 0.05 \text{ MeV}$, $\Gamma_p = 0.45 \pm 0.10 \text{ MeV}$ [10], and $\Gamma_\gamma = 0.95 \pm 0.24 \text{ eV}$ [8]) were adopted. In Fig. 6, we display the resulting S-factors for the resonant capture, as indicated by the dotted line.

Interference effects will occur only in the case that the resonant and direct amplitudes have the same channel spin I and the same incoming orbital angular momentum [8, 33]. The direct capture amplitude for the $^{12}\text{N}(p, \gamma)^{13}\text{O}$ reaction is given by the sum of $I = 1/2$ and $3/2$ components. Since the channel spin for the first resonance is $1/2$, only the first component in the direct capture interferes with the resonant amplitude. Therefore, the total S-factors were calculated with

$$S_t(E) = S_d(E) + S_r(E) \pm 2[S_d^{1/2}(E)S_r(E)]^{1/2} \cos(\delta), \quad (4.1)$$

where $S_d(E)$, $S_r(E)$ and $S_d^{1/2}(E)$ denote the astrophysical S-factors for the direct capture, the resonant capture, and the $I=1/2$ component in the direct capture, respectively. δ is the resonance phase

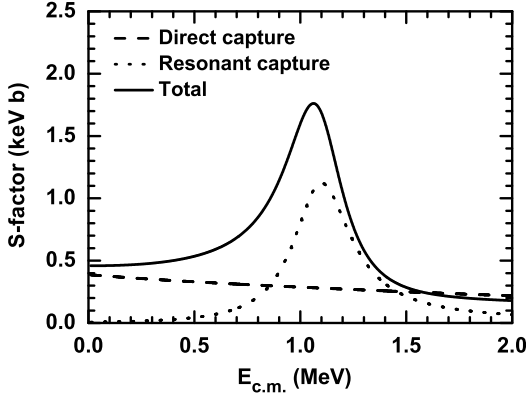


Figure 6: Astrophysical S-factors of the $^{12}\text{N}(p, \gamma)^{13}\text{O}$ reaction as a function of $E_{\text{c.m.}}$. The dashed and dotted curves represent the direct and resonant components, respectively. The solid curve denotes the total S-factor. See text for details.

shift, which can be given by

$$\delta = \arctan \left[\frac{\Gamma_p(E)}{2(E - E_R)} \right]. \quad (4.2)$$

Here, $\Gamma_p(E) = \Gamma_p \frac{P_l(E)}{P_l(E_R)}$, where $P_l(E)$ is the penetration factor. The ratio of the $I=1/2$ amplitude to the total amplitude in the direct capture was derived to be 2/3 using the RADCAP code. Generally, the sign of the interference in Equation 4.1 has to be determined experimentally. However, it is also possible to infer this sign via an R -matrix method. Recently, Banu et al. [8] found the constructive interference below the resonance and the destructive one above it using an R -matrix approach. Based on this interference pattern, the present total S-factors were then obtained, as shown in Fig. 6. In addition, we estimated the uncertainty of the total S-factors by taking into account the errors of the present ANC for the ground state in ^{13}O and the employed resonant parameters for the first excited state in ^{13}O .

The astrophysical $^{12}\text{N}(p, \gamma)^{13}\text{O}$ reaction rates ($\text{cm}^3 \text{s}^{-1} \text{mol}^{-1}$) were then calculated with [34, 35]

$$N_A \langle \sigma v \rangle = N_A \left(\frac{8}{\pi \mu} \right)^{1/2} \frac{1}{(kT)^{3/2}} \int_0^\infty S(E) \exp \left[- \left(\frac{E_G}{E} \right)^{1/2} - \frac{E}{kT} \right] dE, \quad (4.3)$$

where the Gamow energy $E_G = 0.978 Z_1^2 Z_2^2 \mu$ MeV, and N_A is Avogadro's number.

In Fig. 7 we display the resulting reaction rates as a function of temperature, together with the REACLIB compilation [5]. There is a discrepancy of up to a factor of ~ 100 between these two reaction rates for the temperatures below $T_9 = 3$ (T_9 is a temperature in unit of 10^9 K). In addition, our total rates are in good agreement with those in Fig. 9 of Ref. [8] since the similar contribution of the direct capture was found and the same resonant parameters were used in both works. From Fig. 7 one also sees that the direct capture dominates the $^{12}\text{N}(p, \gamma)^{13}\text{O}$ reaction for the temperatures below $T_9 = 1.5$.

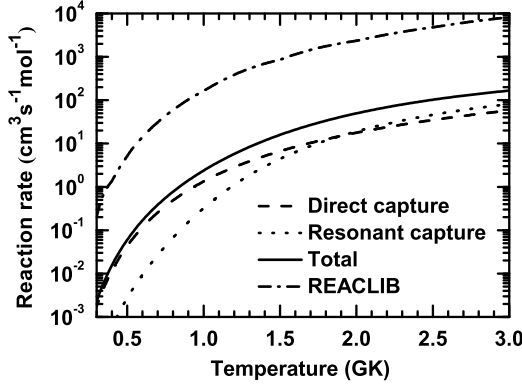


Figure 7: Astrophysical rates of the $^{12}\text{N}(p, \gamma)^{13}\text{O}$ reaction as a function of temperature. The dashed and dotted curves represent the present rates of the direct and resonant captures, respectively. The solid curve represents the total rates in the present work, while the dash-dotted curve denotes the REACLIB compilation [5]. See text for details.

Table 2: The coefficients a_i in Eq. 6 for the central value, lower limit and upper limit of the $^{12}\text{N}(p, \gamma)^{13}\text{O}$ reaction rate. The fitting errors are all less than 6% at $T_9 = 0.01\text{-}10$.

a_i	Central value	Upper limit	Lower limit
a_1	-5.91219	-3.77150	-4.48818
a_2	0.0400148	0.0224401	0.0253469
a_3	-22.2259	-20.3542	-20.5376
a_4	32.2983	28.2893	28.6331
a_5	-3.56352	-3.29024	-3.36174
a_6	0.261761	0.243627	0.252225
a_7	-10.1115	-8.37104	-8.49396
a_8	-10.0637	4.00598	-7.05380
a_9	-0.553380	0.190095	-0.291547
a_{10}	-20.7778	-31.6274	-20.5490
a_{11}	31.5635	31.0575	27.9040
a_{12}	-3.64300	-6.70434	-3.31062
a_{13}	0.248400	-0.399390	0.244458
a_{14}	-12.2610	-13.7936	-10.4292

We fitted the new rates with an expression used in the astrophysical reaction rate library REACLIB [36, 37]. The total reaction rates were fitted as

$$\begin{aligned} N_A \langle \sigma v \rangle = & \exp[a_1 + a_2 T_9^{-1} + a_3 T_9^{-1/3} + a_4 T_9^{1/3}] \\ & + a_5 T_9 + a_6 T_9^{5/3} + a_7 \ln(T_9)] \\ & + \exp[a_8 + a_9 T_9^{-1} + a_{10} T_9^{-1/3} + a_{11} T_9^{1/3}] \\ & + a_{12} T_9 + a_{13} T_9^{5/3} + a_{14} \ln(T_9)]. \end{aligned} \quad (4.4)$$

The coefficients a_i for the central value, lower limit and upper limit of the $^{12}\text{N}(p, \gamma)^{13}\text{O}$ reaction rate are listed in Table 2. The fitting errors are all less than 6% in a range from $T_9 = 0.01$ to $T_9 = 10$.

Since there is the large discrepancy between the rates in this work and those in Ref. [5], the temperature and density conditions at which the rap-processes are expected to operate need to be revised. We performed reaction network simulations with a series of constant temperatures (0.1-1.5 GK) and densities (1-10⁸ g/cm³), and a burning time of 100 s, and primordial abundances and reaction rates from REACLIB as an initial input.

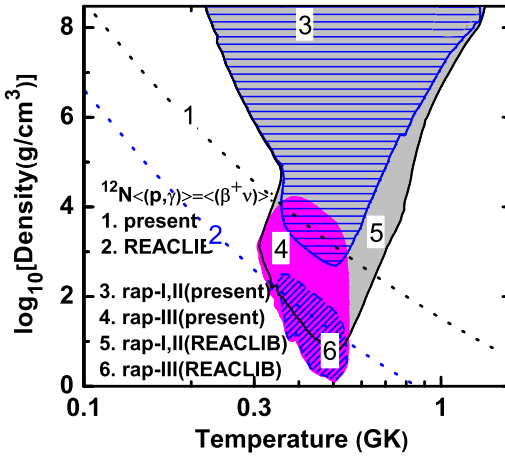


Figure 8: (Color online) Temperature and density conditions at which the $^{12}\text{N}(p, \gamma)^{13}\text{O}$ reaction could operate. Curve 1 represents the equilibrium lines between the rates of the $^{12}\text{N}(p, \gamma)^{13}\text{O}$ reaction and ^{12}N β^+ decay. Curve 2 shows the same result determined from Ref. [5]. Regions 3 and 4 denote the revised temperature-density conditions for rap-I,II and rap-III with the present $^{12}\text{N}(p, \gamma)^{13}\text{O}$ rate, respectively, while Regions 5 and 6 represent those with the REACLIB rate from Ref. [5]. Within these four regions more than 1×10^{-6} abundance (mass fraction/mass number) could be converted to CNO cycle. Note that when determining Regions 3 and 4, only the $^{12}\text{N}(p, \gamma)^{13}\text{O}$ rate was changed, all the rest were still taken from the REACLIB compilations.

In Fig. 8 we show the resulting temperature-density conditions for the rap-I,II and rap-III processes by using the present $^{12}\text{N}(p, \gamma)^{13}\text{O}$ rates and those of Ref. [5]. Curve 1 indicates the present conditions at which the $^{12}\text{N}(p, \gamma)^{13}\text{O}$ reaction has equal strength with the competing β^+ decay of ^{12}N . Below this curve, the ^{12}N β^+ decay will prevail over its proton capture and lead to ^{12}C . Curve 2 shows the same result determined from Ref. [5]. In Regions 3-6, more than 10^{-6} abundances (mass fraction/mass number) could be converted to CNO cycle. One sees that

the present region for rap-I and rap-II (Region 3), where the $^{12}\text{N}(p, \gamma)^{13}\text{O}$ reaction operates, was significantly reduced relative to that from the compilation (Region 5). Therefore, the lower limit of the density, where the 10^{-6} abundance can be converted to CNO cycle, was raised from ~ 10 to $\sim 1000 \text{ g/cm}^3$. This is because the new rates are about two orders of magnitude slower than the compilation. On the contrary, the present region for rap-III (Region 4), where the β -decay of ^{12}N prevails over its proton capture, was enlarged relative to Region 6, which led to an increase of the upper limit of the density from ~ 100 to $\sim 10000 \text{ g/cm}^3$.

In brief, the present rate of $^{12}\text{N}(p, \gamma)^{13}\text{O}$ shows that it will only compete successfully with the β^+ decay of ^{12}N at higher (\sim two orders of magnitude) densities than initially predicted in Ref. [5]. This finding is consistent with the result reported in Ref. [8], while is contrary to that in Ref. [10].

5. Summary and conclusion

In this work, the angular distribution of the $^2\text{H}(^{12}\text{N}, ^{13}\text{O}_{\text{g.s.}})n$ reaction was measured and utilized to derive the ANC for the virtual decay of $^{13}\text{O}_{\text{g.s.}} \rightarrow ^{12}\text{N} + p$. Our result is in agreement with that from the $^{14}\text{N}(^{12}\text{N}, ^{13}\text{O})^{13}\text{C}$ transfer reaction in Ref. [8]. The astrophysical S-factors and rates for the direct capture in the $^{12}\text{N}(p, \gamma)^{13}\text{O}$ reaction were then obtained from the measured ANC by using the direct radiative capture model. In addition, we determined the total S-factors and reaction rates by taking into account the direct capture into the ground state of ^{13}O , the resonant capture via the first excited state of ^{13}O and the interference between them. This work provides an independent examination to the existing results on the $^{12}\text{N}(p, \gamma)^{13}\text{O}$ reaction. We conclude that the direct capture dominates the $^{12}\text{N}(p, \gamma)^{13}\text{O}$ reaction for the temperatures below $T_9 = 1.5$.

We also performed reaction network simulations with the new rates. The results imply that $^{12}\text{N}(p, \gamma)^{13}\text{O}$ will only compete successfully with the $^{12}\text{N} \beta^+$ decay at higher (\sim two orders of magnitude) densities than initially predicted in Ref. [5]. Recent simulation of massive metal-free stars between 120 and 1000 solar masses shows that a metallicity as small as $\sim 1 \times 10^{-9}$ is sufficient to stop the contraction [38]. Therefore, this revise of temperature-density conditions may have substantial implications on the evolution of these massive metal-free stars.

Acknowledgments

We acknowledge the staff of AVF accelerator for the smooth operation of the machine. We thank the anonymous referee for the helpful comments. This work was supported by the National Natural Science Foundation of China under Grant Nos. 11021504, 10875175, 10720101076, 10975193 and 11075219, the 973 program under Grant No. 2013CB834406, KAKEHI of Japan under Grant No. 21340053.

References

- [1] V. Bromm and R. B. Larson, *Annu. Rev. Astron. Astrophys.* **42**, 79 (2004).
- [2] R. Cayrel, *Astron. Astrophys.* **168**, 81 (1986).
- [3] B. J. Carr, *Nature* **326**, 829 (1987).
- [4] G. M. Fuller, S. E. Woosley, and T. A. Weaver, *Astrophys. J.* **307**, 675 (1986).

- [5] M. Wiescher, J. Görres, S. Graff, L. Buchmann, and F.-K. Thielemann, *Astrophys. J.* **343**, 352 (1989).
- [6] Z. H. Li, *Chin. Phys. Lett.* **23**, 3219 (2006).
- [7] R. E. Warner, F. Carstoiu, J. A. Brown, F. D. Becchetti, D. A. Roberts, B. Davids, A. Galonsky, R. M. Ronningen, M. Steiner, M. Horoi, J. J. Kolata, A. Nadasen, C. Samanta, J. Schwartzenberg, and K. Subotic, *Phys. Rev. C* **74**, 014605 (2006).
- [8] A. Banu, T. Al-Abdullah, C. Fu, C. A. Gagliardi, M. McCleskey, A. M. Mukhamedzhanov, G. Tabacaru, L. Trache, R. E. Tribble, Y. Zhai, F. Carstoiu, V. Burjan, and V. Kroha, *Phys. Rev. C* **79**, 025805 (2009).
- [9] T. Teranishi, S. Kubono, S. Shimoura, M. Notani, Y. Yanagisawa, S. Michimasa, K. Ue, H. Iwasaki, M. Kurokawa, Y. Satou, T. Morikawa, A. Saito, H. Baba, J. H. Lee, C. S. Lee, Zs. Fülöp, and S. Kato, *Nucl. Phys. A* **718**, 207c (2003).
- [10] B. B. Skorodumov, G. V. Rogachev, P. Boutachkov, A. Aprahamian, V. Z. Goldberg, A. Mukhamedzhanov, S. Almaraz, H. Amro, F. D. Becchetti, S. Brown, Y. Chen, H. Jiang, J. J. Kolata, L. O. Lamm, M. Quinn, and A. Woehr, *Phys. Rev. C* **75**, 024607 (2007).
- [11] G. L. Wales and R. C. Johnson, *Nucl. Phys. A* **274**, 168 (1976).
- [12] W. Liu, X. Bai, S. Zhou, Z. Ma, Z. Li, Y. Wang, A. Li, Z. Ma, B. Chen, X. Tang, Y. Han, and Q. Shen, *Phys. Rev. Lett.* **77**, 611 (1996).
- [13] J. J. Das, V. M. Datar, P. Sugathan, N. Madhavan, P. V. Madhusudhana Rao, A. Jhingan, A. Navin, S. K. Dhiman, S. Barua, S. Nath, T. Varughese, A. K. Sinha, R. Singh, A. Ray, D. L. Sastry, R. G. Kulkarni, and R. Shyam, *Phys. Rev. C* **73**, 015808 (2006).
- [14] D. Beaumel, T. Kubo, T. Teranishi, H. Sakurai, S. Fortier, A. Mengoni, N. Aoi, N. Fukuda, M. Hirai, N. Imai, H. Iwasaki, H. Kumagai, H. Laurent, S.M. Lukyanov, J.M. Maison, T. Motobayashi, T. Nakamura, H. Ohnuma, S. Pita, K. Yoneda, and M. Ishihara, *Phys. Lett. B* **514**, 226 (2001).
- [15] W. Liu, Z. Li, X. Bai, B. Guo, S. Zeng, Y. Chen, S. Yan, B. Wang, G. Lian, Y. Lu, K. Wu, and N. Shu, *Nucl. Phys. A* **728**, 275 (2003).
- [16] Z. H. Li, B. Guo, S. Q. Yan, G. Lian, X. X. Bai, Y. B. Wang, S. Zeng, J. Su, B. X. Wang, W. P. Liu, N. C. Shu, Y. S. Chen, H. W. Chang, and L. Y. Jiang, *Phys. Rev. C* **74**, 035801 (2006).
- [17] S. Kubono, Y. Yanagisawa, T. Teranishi, S. Kato, T. Kishida, S. Michimasa, Y. Ohshiro, S. Shimoura, K. Ue, S. Watanabe, and N. Yamazaki, *Eur. Phys. J. A* **13**, 217 (2002).
- [18] Y. Yanagisawa, S. Kubono, T. Teranishi, K. Ue, S. Michimasa, M. Notani, J.J. He, Y. Ohshiro, S. Shimoura, S. Watanabe, N. Yamazaki, H. Iwasaki, S. Kato, T. Kishida, T. Morikawa, and Y. Mizo, *Nucl. Instrum. Methods Phys. Res. Sect. A* **539**, 74 (2005).
- [19] H. Yamaguchi, Y. Wakabayashi, G. Amadio, S. Hayakawa, H. Fujikawa, S. Kubono, J. J. He, A. Kim, and D. N. Binh, *Nucl. Instrum. Methods Phys. Res. Sect. A* **589**, 150 (2008).
- [20] H. Kumagai, A. Ozawa, N. Fukuda, K. S. ummerer, and I. Tanihata, *Nucl. Instrum. Methods Phys. Res. Sect. A* **470**, 562 (2001).
- [21] O. B. Tarasov and D. Bazin, *Nucl. Instrum. Methods Phys. Res. Sect. B* **266**, 4657 (2008).
- [22] B. Guo, Z. H. Li, W. P. Liu, X. X. Bai, G. Lian, S. Q. Yan, B. X. Wang, S. Zeng, J. Su, and Y. Lu, *Nucl. Phys. A* **761**, 162 (2005).
- [23] I. J. Thompson, *Comput. Phys. Rep.* **7**, 167 (1988).

- [24] R. L. Varner, W. J. Thompson, T. L. McAbee, E. J. Ludwig, and T. B. Clegg, Phys. Rep. **201**, 57 (1991).
- [25] A. J. Koning and J. P. Delaroche, Nucl. Phys. A **713**, 231 (2003).
- [26] M. B. Tsang, Jenny Lee, and W. G. Lynch, Phys. Rev. Lett. **95**, 222501 (2005).
- [27] X. D. Liu, M. A. Famiano, W. G. Lynch, M. B. Tsang, and J. A. Tostevin, Phys. Rev. C **69**, 064313 (2004).
- [28] B. Guo, Z. H. Li, W. P. Liu, and X. X. Bai, J. Phys. G: Nucl. Part. Phys. **34**, 103 (2007).
- [29] J. Zhang, Nucl. Sci. Eng. **142**, 207 (2002).
- [30] L. D. Blokhintsev, I. Borbely, and E. I. Dolinskii, Sov. J. Part. Nucl. **8**, 485 (1977).
- [31] A. M. Mukhamedzhanov, C. A. Gagliardi, and R. E. Tribble, Phys. Rev. C **63**, 024612 (2001).
- [32] C. A. Bertulani, Comput. Phys. Commun. **156**, 123 (2003).
- [33] A. M. Mukhamedzhanov, A. Azhari, V. Burjan, C. A. Gagliardi, V. Kroha, A. Sattarov, X. Tang, L. Trache, and R. E. Tribble, Nucl. Phys. A **725**, 279 (1999).
- [34] C. E. Rolfs and W. S. Rodney, *Cauldrons in the Cosmos* (The University of Chicago Press, Chicago 1988).
- [35] C. Iliadis, *Nuclear Physics of Stars* (WILEY-VCH Verlag GmbH & Co. KGaA, Weinheim 2007).
- [36] F.-K. Thielemann, M. Arnould, and J. Truran, Advances in Nuclear Astrophysics, ed. A. Vangioni-Flam (Gif-sur-Yvette: Editions Frontière), 525 (1987).
- [37] T. Rauscher and F.-K. Thielemann, At. Data Nucl. Data Tables **79**, 47 (2001).
- [38] A. Heger, S. E. Woosley, I. Baraffe, and T. Abel, in *Proceeding of the Mpa/Eso/Mpe/Usm Joint Astronom Conference on Lighthouses of the Universe: The Most Luminous Celestial Objects and Their Use for Cosmology*, edited by M. Gilfanov, R. Sunyaev, and E. Churazov (Springer-Verlag, Berlin, 2002), p. 369.

Study of the $^{22}\text{Na}+\text{p}$ Resonant Scattering at CRIB

S. J. Jin^{1*†}, Y. B. Wang¹, J. Su¹, S. Q. Yan¹, Y. J. Li¹, Z. H. Li¹, B. Guo¹, G. Lian¹,
S. Zeng¹, X. X. Bai¹, W. P. Liu¹, S. Kubono², H. Yamaguchi², D. Kahl², J. Hu²,
H. S. Jung³, J. Y. Moon³, T. Terenishi⁴, H. W. Wang⁵, H. Ishiyama⁶, H. Iwasa⁷,
H. Komatsubara⁸

¹*China Institute of Atomic Energy, Beijing 102413, China*

²*Center for Nuclear Study(CNS), University of Tokyo, RIKEN Campus, 2-1 Hirosawa, Wako,
Saitama 351-0918, Japan*

³*Department of Physics, Chung-Ang University, Seoul 156-756, Republic of Korea*

⁴*Department of Physics, Kyushu University, 6-10-1 Hakozaki, Fukuoka 812-8581, Japan*

⁵*Shanghai Institute of Applied Physics, Chinese Academy of Sciences, Shanghai 201800, China*

⁶*High Energy Accelerator Research Organization(KEK), 1-1 Oho, Tsukuba, Ibaraki
319-1195, Japan*

⁷*Department of Physics, Tohoku University, Aoba, Sendai, Miyagi 980-8578, Japan*

⁸*Department of Physics, University of Tsukuba, Tsukuba 305-8571, Japan*

The $^{22}\text{Na}+\text{p}$ resonant scattering was studied with a ^{22}Na radioactive ion beam bombarding a hydrogen gas target at the CRIB facility, University of Tokyo. The excitation function of the $^{22}\text{Na}+\text{p}$ elastic resonant scattering was obtained in the energy interval of 0.8–1.6 MeV in the center-of-mass frame. The experimental excitation function was analyzed with a multi-channel multilevel R -matrix code, three resonance states in the compound nucleus ^{23}Mg were revealed. Preliminary results on the deduced resonance parameters are presented.

Key Issues of Elements Synthesis in Cosmos

December, 2012

Beijing, China

*Corresponding author.

†This work is supported by the National Natural Science Foundation of China under Grant Nos. 11021504 and 11175261, and the National Basic Research Programme of China under Grant No. 2013CB834406.

1. Introduction

^{22}Na is one of the most important yet debatable cosmic γ -ray emitters. In 1972, Black found that in Orgueil meteorites the abundance ratio of $^{20}\text{Ne}/^{22}\text{Ne}$ is less than 1.5, which is much smaller than that of 9.8 on earth, this is the so-called Ne-Extraordinary problem[1]. The excessive ^{22}Ne abundances are commonly explained as originated from the β^+ decay of ^{22}Na , which are produced in nova and supernova outbursts. The relative short half-life of $^{22}\text{Na}(T_{1/2}=2.6\text{ y})$ and the delayed 1.275 MeV γ ray indicate that the ^{22}Na may be a very sensitive probe to the nova outburst, especially for the nearby ONe novae from the Sun.

A classical nova is produced by thermonuclear outburst that takes place on the surface of a white dwarf component in a closed binary system[2]. According to José *et al.*[3], at the onset of accretion of H-rich matter to the top of the white dwarf, the evolution of ^{22}Na is mainly dominated by the chain of nuclear reactions $^{20}\text{Ne}(p, \gamma)^{21}\text{Na}(\beta^+)^{21}\text{Ne}(p, \gamma)^{22}\text{Na}(\beta^+)^{22}\text{Ne}(p, \gamma)^{23}\text{Na}$. When the temperature at the burning shell reaches $T=5\times 10^7\text{ K}$, the main nuclear reaction of the NeNa cycle is $^{21}\text{Ne}(p, \gamma)^{22}\text{Na}$, which results in the significant production of ^{22}Na . When $T = 7\times 10^7\text{ K}$, the ^{22}Na abundance will begin to decrease near the burning shell due to the proton captures through $^{22}\text{Na}(p, \gamma)^{23}\text{Mg}$ reaction. When the temperature reaches 10^8 K , the reaction chain through $^{20}\text{Ne}(p, \gamma)^{21}\text{Na}(p, \gamma)^{22}\text{Mg}(\beta^+)^{22}\text{Na}$ starts to contribute, which plays a crucial role in the synthesis of ^{22}Na at the late stages of the outburst. While there are two formation modes for the production of ^{22}Na depending upon the temperature, the $^{22}\text{Na}(p, \gamma)^{23}\text{Mg}$ reaction rates affect crucially the overall ^{22}Na abundance in the ejected shells, see Fig. 1.

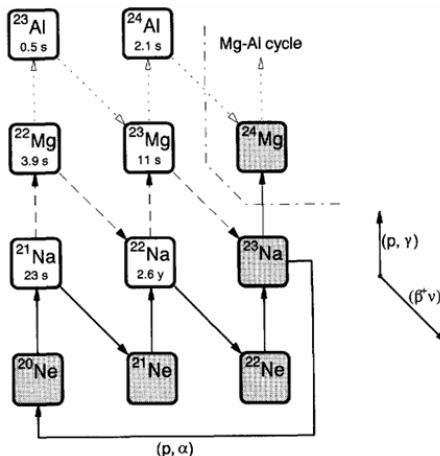


Figure 1: The reaction and decay network involving ^{22}Na in nova outburst.

To the $^{22}\text{Na}(p, \gamma)^{23}\text{Mg}$ reaction, large uncertainties still remain that directly affect the predicted ^{22}Na abundances[4]. This is mainly due to the densely-packed level structure of odd-mass ^{23}Mg close to the proton threshold. Very recently, a new direct measurement using radioactive ^{22}Na targets was reported with different strengths of the known resonances[5]. Because of the limitation of the overall target activities imposed by the tolerable counting rates, these measurements were made at separate energy ranges around the known resonances. To map the relevant resonances for the $^{22}\text{Na}(p, \gamma)^{23}\text{Mg}$ reaction, the $^{22}\text{Na}+p$ entrance channel plus the conventional thick-target

resonant scattering[6] is advantageous due to the feasibility to obtain the excitation function over a relatively wide energy region with a single-energy radioactive ion beam.

2. Experiment

The experiment was carried out at the low-energy RI beam facility CRIB (**CNS Radioactive Ion Beam separator**)[7], University of Tokyo. The CRIB separator has three focal planes, namely F1, F2 and F3, see Fig. 2. F1 is a momentum-dispersive focal plane where the secondary particles are selected by magnetic rigidity. At the achromatic focal plane F2, The secondary particles are focused into a spot of about 10-20 mm (FWHM). The Wien filter section between F2 and F3 is used to select particles by velocity.

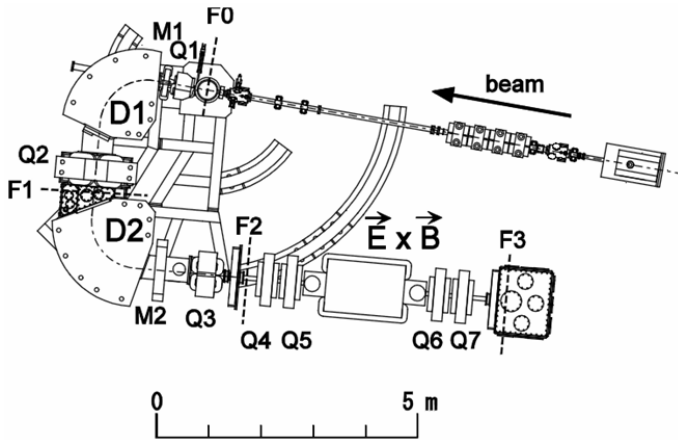


Figure 2: Plane view of the CNS radioactive ion beam facility CRIB.

The ^{22}Na radioactive beam was produced by the $^{22}\text{Ne}(p, n)^{22}\text{Na}$ reaction. The $^{22}\text{Ne}^{7+}$ primary beam was accelerated by the RIKEN AVF cyclotron up to an energy of 6.0 AMeV and had an intensity of about 500 enA. The hydrogen gas target in the F0 chamber was confined in an 80 mm-long cell by two Havar window foils, which were each 2.2 μm thick. The hydrogen gas was kept to 400 ± 3 Torr in pressure by a flow-gas system, and cooled down to about 90 K by liquid nitrogen. The $^{22}\text{Na}^{11+}$ particles were separated by the electromagnetic system of the CRIB facility. Nearly 100% pure ^{22}Na beam was produced with the intensity of about 2.5×10^5 pps, the tiny amount of contaminants was scattered $^{22}\text{Ne}^{10+}$.

The detection system for the $^{22}\text{Na} + p$ elastic scattering installed in the F3 chamber is shown in Fig. 3. The ^{22}Na beam particles went through two parallel plate avalanche counters (PPACs) before reaching the secondary proton target. The timing and position information from the two PPACs were used to determine the beam velocity vector on an event-by-event basis. The gas target chamber has an effective length of 300 mm. The front window of the gas target is a 2.5 μm -thick Havar with a diameter of 30 mm, while the rear one is a 26.5 μm -thick Mylar sealed in a wide slit shape. The energy of the ^{22}Na radioactive beam after the front window of the gas target is 37.1 ± 1.0 MeV, which is measured with a calibrated Single-pad Silicon Detector (SSD) in the beam tuning runs. During the $^{22}\text{Na} + p$ measurement runs, the hydrogen gas target was maintained within 310 ± 2 Torr by a flow-gas system, its effective thickness is enough to fully stop the ^{22}Na

particles. The lighter recoil particles coming out through the exit window were detected by three silicon detector telescopes. Each telescope consists of ΔE and E layers, where ΔE layer is position sensitive with double sided and orthogonally oriented 16+16 readout strips. The thickness of the ΔE detectors range from 50 to 75 μm , where the E detectors have thicknesses of larger than 1 mm. Recoil protons were identified using the $\Delta E - E$, and the time-of-flight information. The proton energy was deduced from the sum of ΔE and E , which was calibrated using proton beams from CRIB and using alpha sources of ^{237}Np , ^{241}Am , and ^{244}Cm . The proton spectrum with Argon gas of 75 Torr which has the equivalent stopping power, was also measured separately to evaluate the background proton events wherever produced other than from the hydrogen gas.

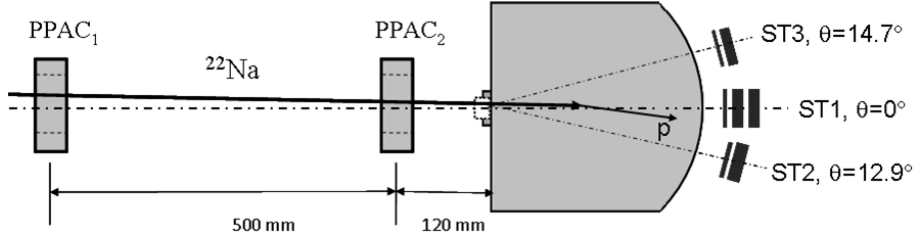


Figure 3: Experimental setup for the $^{22}\text{Na} + p$ scattering in the F3 chamber.

3. Data analysis

The center-of-mass energy $E_{c.m.}$ was deduced from the proton energy and the scattering angle on an event-by-event basis, by assuming the kinematics of elastic scattering and by considering the energy losses of beam and proton along their trajectories. The $E_{c.m.}$ resolution was estimated from the detector energy and angular resolutions and from the energy straggling in the foils and the target. Background proton events were mainly observed in the 0° silicon telescope ST1, which may come from the interaction of ^{22}Na with materials upstream of the target.

The experimental differential cross sections were calculated according to

$$\left(\frac{d\sigma}{d\Omega} \right)_{lab} = \frac{\frac{dN_p}{dE}}{I_{beam} \frac{dN_t}{dE} d\Omega}, \quad (3.1)$$

where dN_p/dE refers to the net proton yield of per $E_{c.m.}$ unit, dN_t/dE is the energy dependant hydrogen atom number, I_{beam} is the number of incident ^{22}Na particles, $d\Omega$ is the solid angle, which is dependent on the reaction point. The averaged cross sections in center-of-mass frame were obtained by

$$\left(\frac{d\sigma}{d\Omega} \right)_{c.m.} = \frac{1}{4\cos\theta_0} \left(\frac{d\sigma}{d\Omega} \right)_{lab}, \quad (3.2)$$

where θ_0 is 0° , 12.9° , 14.7° for ST1, ST2 and ST3, respectively. The excitation function of $^{22}\text{Na} + p$ elastic resonant scattering from $\theta_0=0^\circ$ silicon telescope ST1 is shown in Fig. 4.

Three resonance-like signatures are seen at $E_{c.m.} \sim 1.0$, 1.2 , and 1.35 MeV in the excitation function for ST1. For the $^{22}\text{Na} + p$ elastic channel, there are two channel spins of $7/2^+$ and $5/2^+$, respectively. The largest orbital angular momentum is 1 for the measured $E_{c.m.}$ range, therefore only $l = 0, 1$ needs to consider in the R -matrix analysis. One set of spin and parity assignments is shown in Fig. 4, with deduced resonance widths of 4.7, 3.3, and 1.5 keV, respectively.

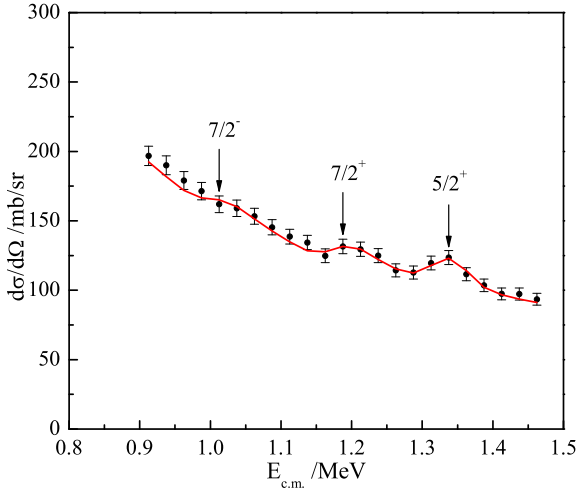


Figure 4: Excitation function of the $^{22}\text{Na}+\text{p}$ elastic resonant scattering.

4. Summary

The $^{22}\text{Na}+\text{p}$ resonant scattering was measured by using the conventional thick-target inverse kinematic method with a high-quality ^{22}Na beam, the excitation function for the $\theta_0=0^\circ$ silicon telescope ST1 was obtained. Further analysis of the experimental excitation functions for the ST2 and ST3, and the evaluation of the impact to the astrophysical $^{22}\text{Na}(\text{p}, \gamma)^{23}\text{Mg}$ reaction rates is being undertaken.

This work was performed at the RI Beam Factory operated by RIKEN Nishina Center and CNS, University of Tokyo. The authors are grateful to the CNS and RIKEN accelerator staff for the smooth operation of the machine.

References

- [1] D.C. Black, Geoch. Cosmochim. Acta **V36**, (1972)347.
- [2] C. E. Rolfs and W. S. Rodney, Cauldrons in the Cosmos, *The University of Chicago Press*, 1988.
- [3] J. José, A. Coc, M. Hernanz, *Astrophys J* (1999) 347.
- [4] W. R. Hix *et al.*, *Nucl Phys A* **718** (2003) 620c.
- [5] A. L. Sallaska *et al.*, *Phys Rev Lett* **105** (2010) 152501.
- [6] K. P. Artmov *et al.*, *Sov J Nucl Phys* **52** (1990) 408.
- [7] Y. Yanagisawa, *et al.*, *Nucl Instr Meth A* **539** (2005) 74.

Research status for the $^{12}\text{C} + ^{12}\text{C}$ fusion reaction in experiment

Yunju Li^{1,2}, Brian Bucher¹, Xiao Fang¹, Xiaodong Tang^{*1 †}

1, University of Notre Dame, Notre Dame, IN 46556, USA

2, China Institute of Atomic Energy, Beijing 102413, China

E-mail: xtang1@nd.edu

The total fusion cross sections of $^{12}\text{C} + ^{12}\text{C}$ in the energy range of 1 to 3 MeV are important for a number of astrophysical scenarios, such as the explosion of Type Ia supernovae, nucleosynthesis in massive stars and recently discovered superbursts. Since the 1960s, the carbon fusion reaction has been measured intensively at sub-barrier energies via detecting the light charged particles or characteristic gamma-rays. Because of the background and the complication of the decay schemes of the fusion residues, neither method is capable to provide the exact total cross sections. Based on the statistical model, the branching ratios between several observable channels and the total fusion cross sections have been predicted, and the calculation results in fair agreement with the existing experimental data. According to the calculation, a method to derive the total fusion cross sections from the observable cross sections is proposed based on the statistical model calculations. In addition, the cross section ratio between the proton and alpha channels is also discussed in this work.

Key Issues of Elements Synthesis in Cosmos

December, 2012

Beijing, China

*Corresponding author.

†This work is supported by the National Natural Science Foundation of China under Grant Nos. 11021504 and 10975193, the National Basic Research Programme of China under Grant No. 2013CB834406.

1. Introduction

$^{12}\text{C} + ^{12}\text{C}$ fusion reaction is the key reaction for the carbon burning phase in the massive stars with more than 8M_\odot in the main sequence stage. Its total cross sections at astrophysically relevant energies are important for the explosion of Type Ia supernovae, nucleosynthesis in massive stars and recently discovered superbursts. The T_9 at which carbon burns range from 0.8 to 1.2, corresponding to center of mass energies from 1 to 3 MeV for the carbon fusion reaction.

Since the molecular resonance phenomena discovered in the $^{12}\text{C} + ^{12}\text{C}$ system in 1960 [1], continuous improvement have been devote to the measurement of $^{12}\text{C} + ^{12}\text{C}$ fusion reaction at sub-barrier energies via detecting the light charged particles [2, 3, 4] or characteristic gamma-rays [5, 6, 7]. For the astrophysics interesting, the measurements have already reached down to 2.1 MeV [7].

For the light charged particles measurements, Becker and Mazarakis have gave the excitation functions for the ground and many excited states in fusion residues at sub-barrier energies separately, however, some of the high excited states will be affected by the background in the experiment. Thus the total cross sections have been derived in this way was only the sum of the observed partial cross sections. For the gamma ray spectroscopy, the cross sections for the ground state and some of the excited states which emitted particles rather than gamma rays cannot be obtained in this way. Thus the carbon fusion cross sections derived via those two ways at sub-barrier energies are not the exact total cross sections.

In Aguilera's work [6], he suggest that the total cross sections for the $^{12}\text{C}(^{12}\text{C}, \text{p})^{23}\text{Na}$ and $^{12}\text{C}(^{12}\text{C}, \alpha)^{20}\text{Ne}$ reactions is equal to the cross sections of 440 keV and 1634 keV gamma rays merge the cross sections of the ground states in the fusion residues ^{23}Na and ^{20}Ne , respectively. Therefore some experiments trend to only measure the cross sections of 440 keV and 1634 keV gamma rays. To examine this viewpoint, the branching ratios for the observable components in experiment have been calculated based on the statistical model and compared with the experimental results.

In addition, the cross section ratio between the proton and alpha channels is an important parameter for the nucleosynthesis network. It decide the ratio of the yield for ^{13}C and ^{16}O , and hence decide the main neutron source in shell carbon burning. Since no exact total cross sections for the proton and alpha evaporation channels of the carbon fusion reaction at astrophysics, the value 1 was adopted for this ratio [8]. We also wish to give a prediction for this ratio based on the statistical model calculation and data analysis.

2. Decay schemes and research status for the $^{12}\text{C} + ^{12}\text{C}$ fusion reaction

The Coulomb barrier height for the $^{12}\text{C} + ^{12}\text{C}$ system is about 6.3 MeV, much higher than the energies of astrophysical relevance (1 to 3 MeV). In that energies, the cross section falls rapidly below one nanobarn. This is the main reason why it is difficult to derive the fusion cross section at astrophysical energies.

The energy-level diagram for the $^{12}\text{C} + ^{12}\text{C}$ system is shown in Figure 1. The $^{12}\text{C} + ^{12}\text{C}$ fusion reaction can covers alpha, proton, neutron, ^8Be and radiative channels at 1 to 3 MeV. For alpha and proton channels, the carbon fusion reaction can populate many states of the residue nuclei. For the neutron channel only the ground state is opened at astrophysical energies, and will be closed

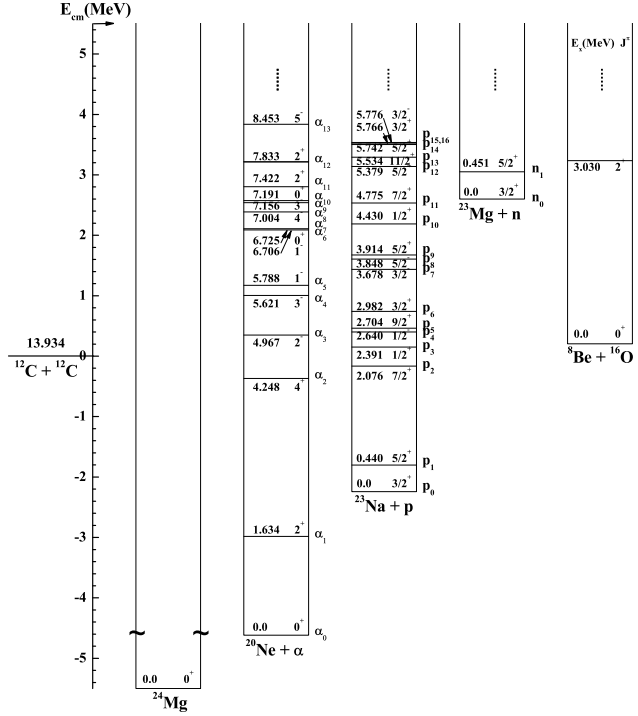


Figure 1: Energy-level diagram for the $^{12}\text{C} + ^{12}\text{C}$ system. α_i , p_i and n_i are corresponding to the relevant states in ^{20}Ne , ^{23}Na and ^{23}Mg .

at about 2.6 MeV. From some of the previous results for all these channels [2, 4, 7, 9, 10, 11], as shown in Figure 2, one can see that the alpha and proton channels dominate the total fusion cross sections. ^8Be channel has a relative small cross sections at 4 to 6 MeV, but it match with the alpha channel at lower energies. Whereas there is only one work for this channel, it still needs a double check in the experiment. In this work, we mainly discuss the alpha and proton channels.

Since the alpha emission threshold for ^{20}Ne nucleus is only 4.73 MeV, most of the excited states above it will emit alpha particle rather than gamma rays. For ^{23}Na , many of the excited states can direct transit to the ground states, then the total cross sections for the proton evaporation

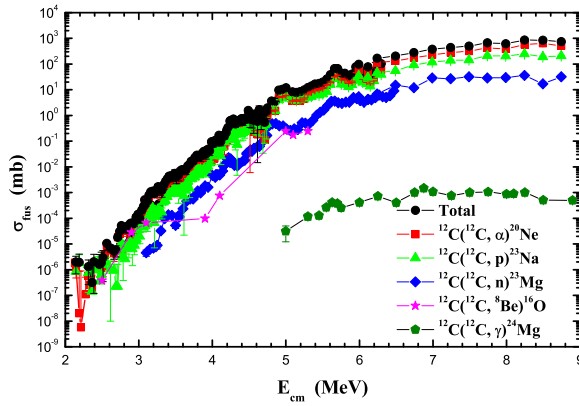


Figure 2: Cross sections for each channel of the $^{12}\text{C} + ^{12}\text{C}$ fusion reactions. Data from Ref.[2, 4, 7, 9, 10, 11]

of carbon fusion reaction should be the sum of the partial cross sections for the ground state and all the characteristic gamma rays which are emitted from the transitions to the ground state. So far, the gamma ray spectroscopy only focus on 440 and 1634 keV gamma rays which are emit from the first excited states in ^{23}Na and ^{20}Ne . Therefore the results are derived in this way not the exact total cross sections.

Table 1: Numerical factors for the yields of the characteristic gamma rays from partial cross sections of alpha evaporation channels (%).

	σ_{α_1}	σ_{α_2}	σ_{α_3}	σ_{α_4}	σ_{α_8}
$\sigma_{\gamma(1634)}$	100	100	99.4	6.47	76.6
$\sigma_{\gamma(4967)}$			0.6	0.002	0.07
$\sigma_{\gamma(5621)}$				0.53	0.13

To compare all the results of the carbon fusion reaction from light charged partial measurement and gamma ray spectroscopy, we need transfer the partial cross sections for each state to that of characteristic gamma rays. The cross sections for the yields of the characteristic gamma rays which directly transit to the ground states can be calculated from the expression

$$\sigma_\gamma = \sum_i f_i \sigma_i, \quad (2.1)$$

where σ_i are the partial cross sections for the i^{th} excited state in residue nucleus. f_i are the factors of which the values listed in Table 1 and 2 for alpha and proton evaporation channels, they are deduced based on the γ transition branching ratios from NNDC.

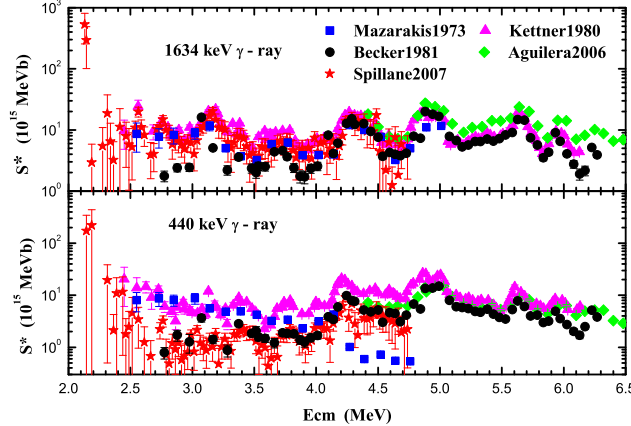


Figure 3: Comparisons for the derived astrophysical S^* factor of 1634 and 440 keV gamma rays from previous experiments.

Based on expression 2.1 and the numerical factors in Table 1 and 2, the astrophysical S^* factor for 1634 and 440 keV gamma rays are calculated by using Becker's and Mazarakis' data, and compared with other data from gamma ray spectroscopy as shown in Figure 3. It can be seen for 1634 keV gamma ray, Aguilera's results are a litter bit higher than others. For 440 keV gamma ray,

Table 2: Same as Table 1, but for proton evaporation channels (%).

	$\sigma_{\gamma(440)}$	$\sigma_{\gamma(2076)}$	$\sigma_{\gamma(2391)}$	$\sigma_{\gamma(2640)}$	$\sigma_{\gamma(2982)}$	$\sigma_{\gamma(3848)}$
σ_{p_1}	100					
σ_{p_2}	91.8	8.2				
σ_{p_3}	34.3		65.7			
σ_{p_4}				100		
σ_{p_5}	97.1	2.9				
σ_{p_6}	41.2		0.2		58.6	
σ_{p_7}	79.4		0.9	19.5	0.3	
σ_{p_8}	66.4	5.0	0.004	4.5	1.2	22.9
σ_{p_9}	17.7	0.7	0.7		1.35	
$\sigma_{p_{10}}$	2.8		0.7			
$\sigma_{p_{11}}$	97.4	2.6				
$\sigma_{p_{12}}$	80.9	1.8	0.01		4.2	
$\sigma_{p_{13}}$	96.0	4.0				
$\sigma_{p_{14}}$	29.1					
$\sigma_{p_{15}}$	43.1	0.08		4.5	0.02	0.3
$\sigma_{p_{16}}$	67.1		32.9			

the shape for Mazarakis' results are totally different from others, and Kettern's data much higher than the rest. All of these points should be checked in experiment.

3. Branching ratios calculated and data analysis

To analyze how much will missed for the total cross sections in previous measurements, we plan to calculate the partial cross sections based on the statistical model at first and derive the branching ratios which can be observed in the experiment such as branching ratios for the ground state, 440 and 1634 keV characteristic gamma rays, and then make comparison with the experimental data, hoping propose the method for deriving the total cross sections finally.

Reactions in which a compound nucleus is formed are the simplest cases for the application of the statistical model. To calculate the cross sections of the fusion and evaporation, the Hauser-Feshbach formula is involved. Let all quantum numbers that specify the colliding nuclei and the two nuclei in the exit channel be denoted by a and a' , respectively. Similarly, $\mathbf{I} + \mathbf{S} = \mathbf{J} = \mathbf{I}' + \mathbf{S}'$, $\mathbf{S} = \mathbf{I} + \mathbf{i}$, and $\mathbf{S}' = \mathbf{I}' + \mathbf{i}'$ denote the angular momentum coupling for orbital angular momentum I , channel spin S , and intrinsic angular momenta i and i' . Then the Hauser-Feshbach formula [12] is expressed as

$$\sigma_{aa'} = \pi \hat{\lambda}_\alpha^2 \sum_J \frac{2J+1}{(2I+1)(2i+1)} \frac{[\Sigma_{Sl} T_l(\alpha)]^J [\Sigma_{S'l'} T_{l'}(\alpha')]^J}{[\Sigma_{a''S''l''} T_{l''}(\alpha'')]^J}, \quad (3.1)$$

where T_l denotes the optical model transmission coefficient.

The spin populations of $^{24}\text{Mg}^*$ compound nucleus are calculated by using CCFull code [13] as shown in Fig.4. It can be seen that at low energy, 0^+ , 2^+ , 4^+ and 6^+ have the relative high population, thus only these components are considered in the cross section calculations.

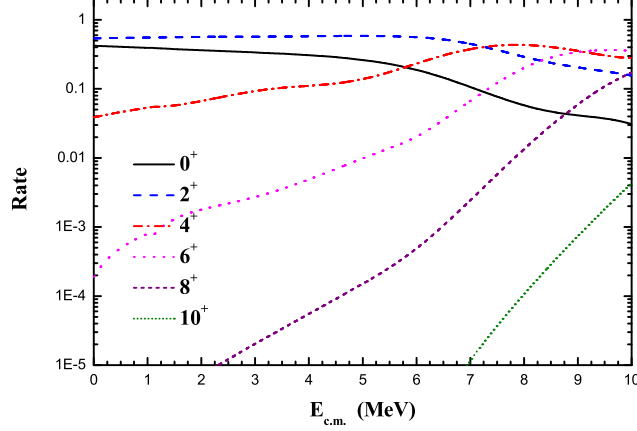


Figure 4: Spin populations of $^{24}\text{Mg}^*$ compound nucleus, calculated with CCFull code [13].

Based on expression 3.1, the relative cross sections of carbon fusion reaction corresponding to each total angular momentum of $^{24}\text{Mg}^*$ compound nucleus are calculated by using Talys code [14]. According to the calculated spin population of $^{24}\text{Mg}^*$ compound nucleus for carbon fusion as shown in Figure 4, then the branching ratios of each alpha and proton evaporation channels are derived and shown in Figure 5, respectively. It can be seen that the branching ratios for high excited states falls rapidly as the energy decrease. For the alpha channel, the ground and first excited states dominate the total alpha evaporation cross sections at astrophysical energies. But for the proton channel, except the main parts of the ground and first excited states, the third, fourth and other excited states also have an observable contributions on the total proton evaporation cross sections at astrophysical relevant energy region.

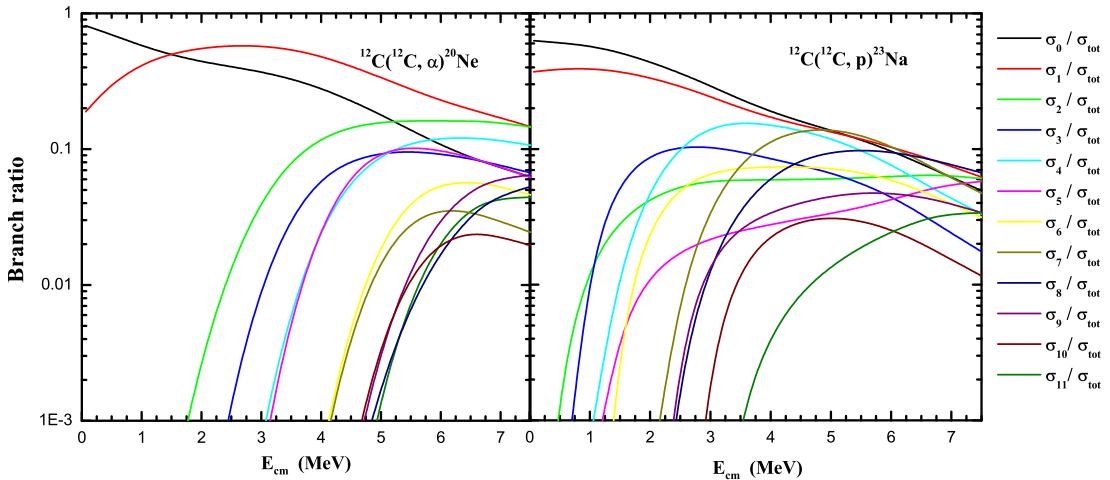


Figure 5: Partial branching ratios for each state of alpha and proton evaporation channels for carbon fusion reaction.

To check our calculated results, we make a comparison for the theoretical and experimental branching ratios of the ground state, 1634 and 440 keV characteristic gamma rays, respectively. Because Becker's experimental results [4] contain many states and much more close to the total cross sections, his data are used in the comparison and the sum of the observed partial cross sections used as the total cross sections in the branching ratio calculations.

The pure calculations of the branching ratios without free parameter are shown in Figure 6 with the solid lines and denote as Theory1. Since much cut-off exist in the charged particle measurement, we also take this condition into account in the calculations and the results are also derived as shown in Figure 6 with dashed lines and describe as Theory2.

As can be seen in Figure 6, the calculated results are well predicting the average trend of experimental data at sub-barrier energies even though there are irregular fluctuations exist. As the predicted, the contributions for the ground state of alpha and proton channels take about 30 to 60 percent in the total cross sections at astrophysical energies, respectively. Thus the cross sections for the ground states should be an important component for the carbon fusion reaction, which should not be omitted in the experiment and only focus on the 1634 and 440 keV characteristic gamma rays are much more insufficient for deriving the total carbon fusion cross sections.

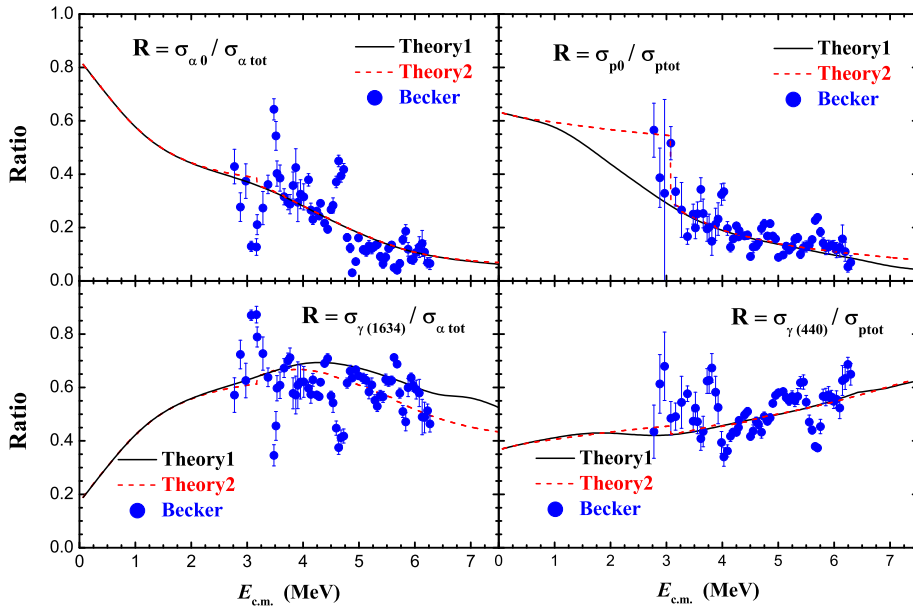


Figure 6: Comparison of the branching ratios for the ground states, 1634 and 440 keV characteristic gamma rays. Theory1 is the pure calculations without free parameter, Theory2 consider the condition of the cut-off exist in the experiment. The total cross sections used for the experimental data are the sum of the observed partial cross sections from Becker's work [4].

Then we can check Aguilera's suggestions on the total cross sections for the alpha and proton channels as mentioned in first section. As can be seen in Figure 7, for the alpha channel, the ground state and 1634 keV gamma ray take only 60% ~ 90% of the total cross sections at 4 ~ 6 MeV in the centre of mass frame. Fortunately, the sum of $\sigma_{\alpha 0}$ and $\sigma_{\gamma(1634)}$ equal to the total cross sections at astrophysical energies, thus only measure these two components can effectively derived the total cross sections at such important energy range. But the proton channel is not so optimistic, only

measure the ground state and 440 keV characteristic gamma ray will lost 40% at 3 to 7 MeV in the centre of mass frame, and will lost about 10% to 30% at astrophysical energies. Thus the gamma ray spectroscopy results should be revised or other independent components should be taken into account in the experiment.

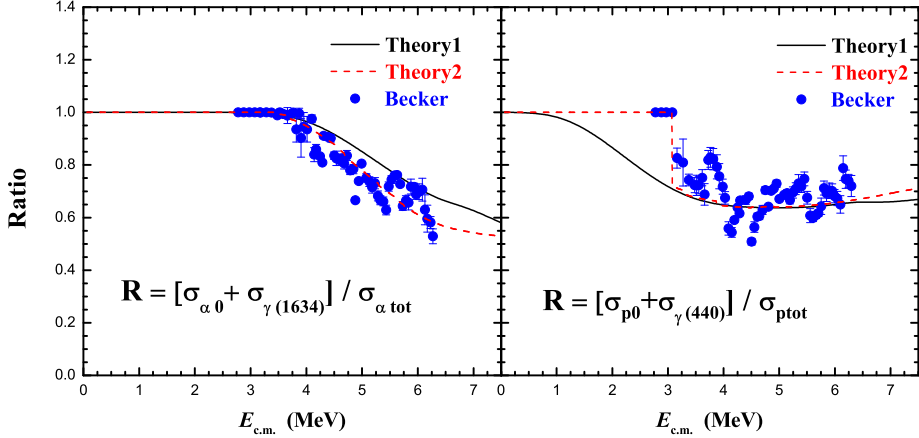


Figure 7: Comparison of $[\sigma_{\alpha 0} + \sigma_{\gamma(1634)}] / \sigma_{\alpha \text{tot}}$ and $[\sigma_{p0} + \sigma_{\gamma(440)}] / \sigma_{p\text{tot}}$ for theoretical and experimental data.

Based on the ground state data from Becker's work and the calculated ratios for $[\sigma_{\alpha 0} + \sigma_{\gamma(1634)}] / \sigma_{\alpha \text{tot}}$ and $[\sigma_{p0} + \sigma_{\gamma(440)}] / \sigma_{p\text{tot}}$, Kettner's, Aguilera's and Spillane's data were revised and compared with the total cross sections derived from Becker's and Patterson's charged particle measurements shown in Figure 8. After revised, Aguilera's and Spillane's data make a fair agreement with Becker's for the proton channel, Kettner's data are much higher than others but agree with Patterson's below 4 MeV. For the alpha channel, only Aguilera's results higher than others above 5.2 MeV and Becker's data a little lower below 4 MeV, except that, the rest are agree well with each other within the uncertainty. By the way, those differences also should be double checked in the experiment.

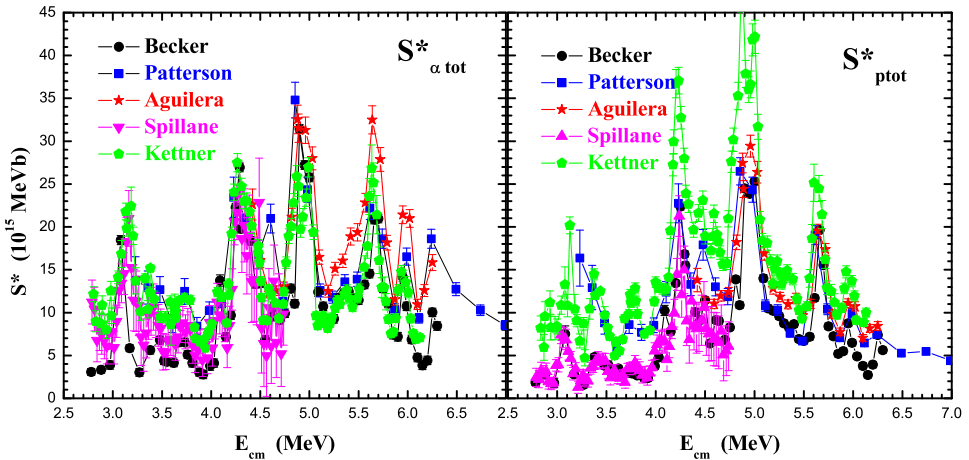


Figure 8: Revised total S^* factors for Kettner's, Spillane's and Aguilera's results, and compared with the total S^* factors of alpha and proton channels from Becker's and Patterson's charged particle measurement.

Whereas the revised method may lead an additional fluctuation above 20% into the total cross sections for the proton channel, thus other independent components should be taken into account in the experiment for deriving the precise total cross sections. From Figure 5, for all the individual exit channels of proton evaporation, the fraction of the third, fourth and sixth excited states have the relative large branching ratios, and the direct transit to ground state for these mention states also have the relative large gamma transition branching ratios as shown in Table 2. Therefore if these three components also take into account in the experiment as well as the ground state and the 440 keV gamma ray, one can see that from Figure 9, more than 97% of the total cross sections will be grasped at astrophysical energies.

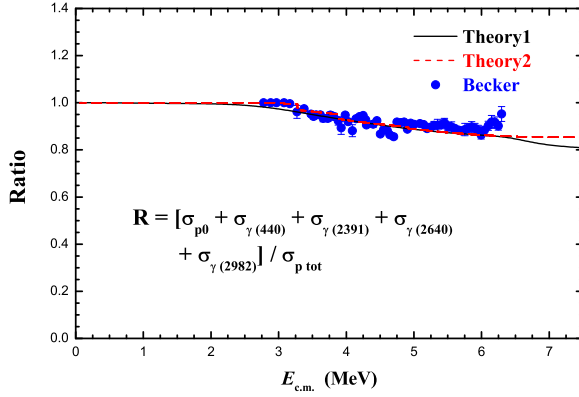


Figure 9: Calculated branching ratio for $[\sigma_{p0} + \sigma_{\gamma(440)} + \sigma_{\gamma(2391)} + \sigma_{\gamma(2640)} + \sigma_{\gamma(2982)}] / \sigma_{p\text{tot}}$ and the comparison with the experimental data.

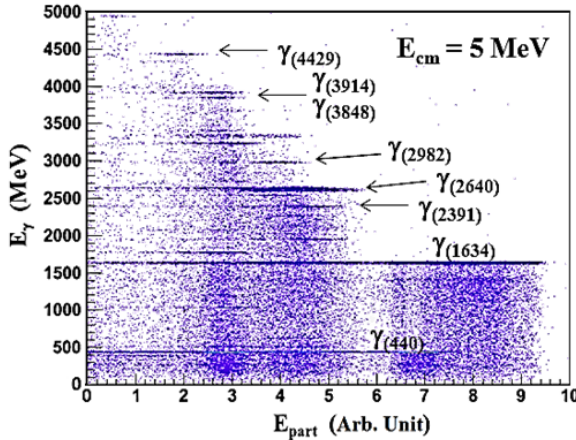


Figure 10: Two-dimensional (energy of gamma rays vs energy of particles) coincidence spectrum at $E_{cm} = 5$ MeV from Ref. [15].

The recent particle-gamma coincidence measurement has been carried out at Argonne [15] by using the gammasphere coincidence with the silicon detector. From the particle-gamma coincidence spectrum at $E_{cm} = 5$ MeV as shown in Figure 10, the mentioned characteristic gamma rays can be found clearly. Thus for effectively deriving the total carbon fusion cross sections for alpha and proton channels, we propose to measure the ground state of these two channels, the 440, 1634, 2391, 2640 and 2982 keV characteristic gamma rays in experiment at low energies.

4. Ratio between $\sigma_{p\text{tot}}$ and $\sigma_{\alpha\text{tot}}$

In the previous section, the statistical model can well predict the average trend of the branching ratios for $R_{\gamma(440)} = \sigma_{\gamma(440)} / \sigma_{p\text{tot}}$ and $R_{\gamma(1634)} = \sigma_{\gamma(1634)} / \sigma_{\alpha\text{tot}}$. Then based on the ratio of these two branching ratios, we can give a way to derive the total cross section ratio as the expression:

$$\frac{\sigma_{p\text{tot}}}{\sigma_{\alpha\text{tot}}} = \frac{\sigma_{\gamma(440)}}{\sigma_{\gamma(1634)}} / \frac{R_{\gamma(440)}}{R_{\gamma(1634)}}. \quad (4.1)$$

Thus if the average trend of $\sigma_{\gamma(440)} / \sigma_{\gamma(1634)}$ can be well predicted by statistical model calculation, then the average trend of $\sigma_{p\text{tot}} / \sigma_{\alpha\text{tot}}$ also can be predicted. The calculated $\sigma_{\gamma(440)} / \sigma_{\gamma(1634)}$ and the comparison with experimental data are shown in Figure 11. The experimental data are much different and separated into two groups [4, 5, 6, 7, 16]. If Aguilera's and Spillane's data of $\sigma_{\gamma(440)} / \sigma_{\gamma(1634)}$ time a factor of 2, all of the data agree with each other within the uncertainty.

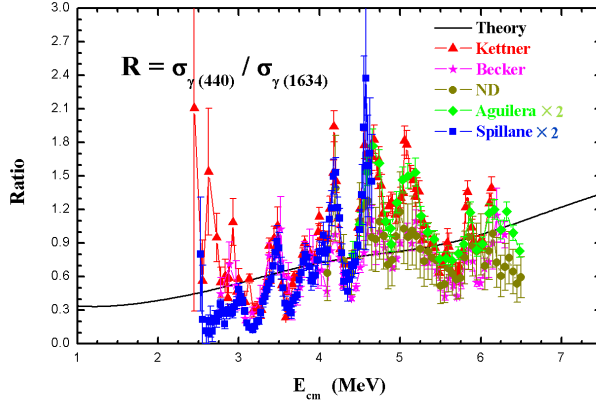


Figure 11: Ratio between $\sigma_{\gamma(440)}$ and $\sigma_{\gamma(1634)}$ calculated from statistical model and experimental data [4, 5, 6, 7, 16].

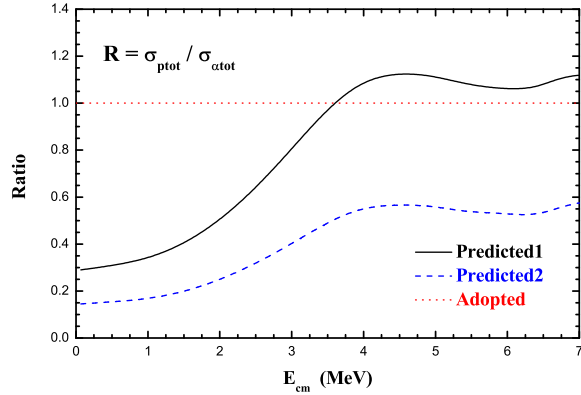


Figure 12: Predicted $\sigma_{p\text{tot}} / \sigma_{\alpha\text{tot}}$ together with the adopted value. Predicted1 is derived based on the experimental data of Kettner, Becker and ND. Predicted2 is derived based on Aguilera's and Spillane's results.

According to these experimental data, two predictions on $\sigma_{p\text{tot}} / \sigma_{\alpha\text{tot}}$ are obtained based on the statistical model calculation as shown in Figure 12, both of them fall rapidly with the energy

decrease at astrophysical energies and much lower than the adopted. Which one is advisable? It is highly needed the reliable experimental certification.

5. Summary

From 1960s, intensive effort have devoted to the carbon fusion experiments at sub-barrier energies, but it is still obvious divergence exist for the absolute cross sections and the cross section ratio of the 440 and 1634 keV characteristic gamma rays. Furthermore it is highly needed the exact total carbon fusion cross sections at astrophysical energies and even at sub-barrier energies.

In the present work, the branching ratios of several observable channels have been calculated based on the statistic model. The theory results well predict the average trend of the branching ratios for carbon fusion reaction. The previous results for the carbon fusion reaction are not the exact total cross sections. For the most important part of this work, we propose measure the ground state of alpha and proton channels, the 440, 1634, 2391, 2640 and 2982 keV characteristic gamma rays in the experimental for effectively deriving the total carbon fusion cross sections. The cross section ratio between the alpha and proton evaporation for the carbon fusion reaction is also predicted, but it still needs the experimental certification.

References

- [1] E. Almqvist, D.A. Bromley, J.A. Kuehner, *Phys. Rev. Lett.* **4** (1960) 515.
- [2] J.R. Patterson, H. Winkler, C.S. Zaidins, *Astrophys. J* **157** (1969)
- [3] M.G. Mazarakis, W.E. Stephens, *Phys. Rev. C* **7** (1973) 1280. 367.
- [4] H.W. Becker, K.U. Kettner, C. Rolfs, et al., *Z. Phys. A* **303** (1981) 305.
- [5] K.U. Kettner, H. Lorenz-Wirzba, C. Rolfs, *Z. Phys. A* **298** (1980) 65.
- [6] E.F. Aguilera, P. Rosales, E.M. Quiroz, et al., *Phys. Rev. C* **73** (2006) 064501.
- [7] T. Spillane, F. Raiola, C. Rolfs, et al., *Phys. Rev. Lett.* **98**(2007)122501.
- [8] W.A. Fowler, G.R. Caughlan, B.A. Zimmerman, et al., *Annual Review of Astronomy and Astrophysics* **13** (1975) 69.
- [9] A.M. Nathan, A.M. Sandorfi, T.J. Bowles, *Phys. Rev. C* **24** (1981) 932.
- [10] B. Čujec, I. Hunyadi, and I. M. Szöghy, *Phys. Rev. C* **39** (1989) 1326.
- [11] B. Bucher, et al., Private communication.
- [12] E. Vogt, in *Advances in Nuclear Physics*, Vol. I (M. Baranger and E. Vogt, cd.), Plenum, New York (1968), p. 261.
- [13] K. Hagino, N. Rowley, A.T. Kruppa, *Comp. Phys. Comm.* **123** (1999) 143.
- [14] A.J. Koning, S. Hilaire, M.C. Duijvestijn, in *Proceedings of the International Conference on Nuclear Data for Science and Technology, Santa Fe New Mexico(USA), 2004*, edited by R.C. Haight, M.B. Chadwick, T. Kawano, and P. Talou (AIP Conf. Proc. 769, New York, 2005), p. 1154.
- [15] C.L. Jiang, K.E. Rehm, X.Fang, et al., *Nucl. Instr. Meth. Phys. Res. A* **682** (2012) 12.
- [16] X. Tang, et al., to be submitted.

Nuclear uncertainties in s-process

Y.J. Zhang^{1,2}, Y.S. Chen^{*1†}, J.Y. Guo², S.Q. Hou^{1,3}, J.R. Shi⁴, M. Smith⁵

¹*China Institute of Atomic Energy, Beijing 102413, China*

²*Anhui University, Hefei 231000, China*

³*Institute of Modern Physics, Chinese Academy of Sciences, Lanzhou 730000, China*

⁴*National Astronomy and Astrophysics, Chinese Academy, Beijing 100012, China*

⁵*Physic Division, Oak Ridge National Laboratory, Oak Ridge, Tennessee 37831-6354*

E-mail: yschen@ciae.ac.cn

The heavy elements are produced by the s- and r-processes, and their astrophysical sites are mainly the AGB star and the supernova, respectively. The description of nucleosynthesis of heavy elements critically depends on the nuclear inputs of neutron capture cross sections and weak decay rates for nuclei on the s- and r-process paths. The uncertainties of nucleosynthesis simulations originated from the uncertainties of nuclear data are still too large for the accurate description of creation of matter in the stellar evolution. The present work analyzes systematically the neutron cross sections and the weak decay rates for the s-process. The network calculations for the constant temperature s-process have been performed by using the different data sets and then the results are compared to investigate the nuclear uncertainties in the s-process calculations. It is found that among the available data some neutron capture cross sections may have a large uncertainty, of a factor of 2~4. The calculated abundances for those unique isobar nuclei where the cross sections have such a large uncertainty present a similar large uncertainty.

Key Issues of Elements Synthesis in Cosmos

December, 2012

Beijing, China

*Corresponding author.

†This work is supported by the National Natural Science Foundation of China under Grant Nos. 11021504, 11175258 and 11275068.

1. Introduction

The heavy elements are only 6-10 percent of the solar matter but they have 54 stable nuclides ($Z>30$, $\tau_{1/2} > 10^6$ yrs) while there are only 30 stable nuclides with $A<30$. The production of heavy elements plays uniquely important role in understanding of creation of matter and evolution of stellar in the universe. The heavy elements are synthesized by the progressive neutron capture reactions, called as the s- and r- processes. The description of the nucleosynthesis of heavy elements critically depend on the nuclear inputs of neutron capture cross sections and weak decay rates for nuclei on the s- and r- process pathes. The uncertainties of the results in s- and r- nucleosynthesis simulations are still too large for an accurate description of creation of matter in the stellar evolution because the nuclear input data have a large uncertainty, especially for the r-process where the path goes through the region of neutron rich unstable nuclei. The present work analysis systematically the neutron cross sections and the weak decay rates for the s-process. The data have been collected and sorted into the sets for the s-process chain, and then the selected different data sets are used as the inputs in the s-process network calculations for a comparison. For this purpose, the constant temperature s-process calculation has obviously an advantage to focus on the test of nuclear data by avoiding the uncertainties in the stellar modeling. The assumption of constant temperature is, moreover, a first approximation to a more general problem in the s-process. We will see that the calculated abundances of some unique isobar nuclei could have a large uncertainty up to a factor of 2~4 when the different data sets are used. A brief description of the network equations for the s-process is given in section 2. The results of calculations and discussions are in section 3. A summary in section 4.

2. brief description of the s-process equations

The s-process is formed with certain progressive neutron capture reactions and the weak decays of nuclei of atomic mass $A>50$ near the valley of stability. The s-process occurs at a typical temperature of 3×10^8 K, which places it in helium burning in AGB star. The time scale for neutron capture of a nucleus on the s-process path is typically of the order of 10 years. The competition between neutron capture and the weak decay is thus significant for many of the longer lived beta-unstable nuclei. The differential equations of the s-process chain of neutron captures is

$$\frac{dN(A)}{dt} = n_n(t) \langle \sigma v \rangle (A-1)N(A-1) - n_n(t) \langle \sigma v \rangle (A)N(A). \quad (2.1)$$

Where $N(A)$ is the abundance of the unique isobar of atomic weight A on the s-process path, $n_n(t)$ is the free neutron density and $\langle \sigma v \rangle$ stands for the neutron capture reaction rate. The s-process chain may branch at the unique isobar of atomic weight A due to competition between neutron capture and beta decay and the resulting equation is then

$$\frac{dN(A)}{dt} = \lambda_n(A-1)N(A-1) - [\lambda_-(A) + \lambda_n(A)]N(A), \quad (2.2)$$

where $\lambda_n = n_n(t) \langle \sigma v \rangle$ and λ_- is the beta decay rate. When an unique isobar of A undergoes competitive beta decay , positron decay and electron capture, the equation is written as

$$\frac{dN(A)}{dt} = \lambda_n(A-1)N(A-1) - [\lambda_{ec}(A) + \lambda_+(A) + \lambda_-(A)]N(A), \quad (2.3)$$

where λ_{ec} and λ_+ is electron capture and positron decay rates, respectively. In the case where the nucleus of (A,Z) is created also by the positron decay and electron capture of (A,Z+1), the equation becomes to more complicated,

$$\frac{dN(A,Z)}{dt} = \lambda_n(A-1,Z)N(A-1,Z) + [\lambda_{ec}(A,Z+1) + \lambda_+(A,Z+1)]N(A,Z+1) - \lambda_n(A,Z)N(A,Z). \quad (2.4)$$

As long as the s-process chain is given one can construct straightforwardly the set of equations by using the equations of types given above.

Usually, by changing the variable time t to irradiation (or exposure),

$$\tau \equiv \int_0^t n_n(t') V_{Th} dt', \quad (2.5)$$

the equation (2.1) is reduced to

$$\frac{dN(A)}{d\tau} = \bar{\sigma}(A-1)N(A-1) - \bar{\sigma}(A)N(A). \quad (2.6)$$

Where V_{Th} is the thermal velocity (value is determined by temperature T) and $\bar{\sigma} = <\sigma>$ stands for the Maxwell average cross section. For the simplicity we use the symbol " σ " hereafter to denote the Maxwell average cross section. Similarly, changing the variable time t to the irradiation τ in Eq.s(2.2, 2.3, 2.4) is straightforward by using Eq.(2.5).

3. results of calculations and discussions

For solving the net work equations of s-process it is convenient to define the function $\Phi(A) = \sigma(A)N(A)/N_0(^{56}Fe)$ which has an advantage of convergency of the solution in numerical calculation. As the s-process solutions of different seed nuclei can be superposed it is the usual way to consider the most important single seed nucleus ^{56}Fe . The abundances are normalized with respect to the initial abundance of ^{56}Fe as presented in the definition of Φ . In the present calculation we use the typical temperature of $T = 3.1 \times 10^8$ K and the neutron density of $n_n = 1.6 \times 10^7 cm^{-3}$, which are average conditions for the solar-system s-process environment.

Two different sets of nuclear data are used as inputs in the s-process simulation for the same s-process path. One set contains the cross sections of neutron capture and the weak decay rates available around 1971, taken from Ref.[1] and is denoted by 1971set. Another set has the cross sections and weak rates which are available around 2000, taken from Ref.[2] and is denoted by 2000set. In the 1971set, cross sections for ^{63}Ni , ^{79}Se , ^{81}Kr , ^{93}Zr , ^{107}Pd , ^{151}Sm , ^{193}Pt , ^{204}Pb and ^{209}Bi are missing and we adopt the corresponding data from the 2000set, namely, so that the cross sections for these nuclei are the same in the two sets. The cross sections of neutron capture for unique isobar nuclei on the s-process path are shown in Fig.(1) for a comparison between the two data sets. The two sets are significantly different in the cross sections for the majority of nuclei on the s-process path. It is seen that some important neutron cross sections differ by a factor of 2~4 between the two sets. We will see that the large uncertainties in the nuclear input cause the similar large uncertainties in predictions of the s-abundances.

The iron-family nuclei are located at the beginning in the chain and their abundances calculated in function of neutron irradiation are shown in Fig.(2). It is seen that the two data sets give very

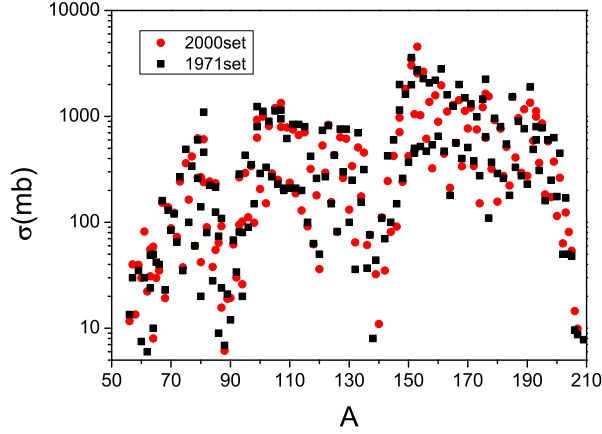


Figure 1: Comparison between the two data sets for cross sections of neutron capture for *s*-process nuclei.

different abundance distributions, especially for ^{58}Fe . The difference is originated from the large difference between neutron capture cross sections of ^{58}Fe in the two sets. The cross section for ^{58}Fe is 13.5mb and 4.5mb in the 2000set and 1971set, respectively. The much smaller cross section value in the 1971set leads to a much larger abundance of ^{58}Fe . The rate of the reaction chain of $^{58}\text{Fe}(n, \gamma)^{59}\text{Fe}(\beta^-)^{59}\text{Co}$ is similar to the rate of neutron capture on ^{58}Fe because the half-life time of ^{59}Fe is very short, only 44.5 days. For this mechanism the calculated abundances of ^{59}Co with the two sets are much different because the abundances of ^{58}Fe are much different. It is obvious that the abundance of ^{57}Fe is not much different between the two sets because its cross sections in the two sets are similar and they are located before ^{58}Fe in the chain.

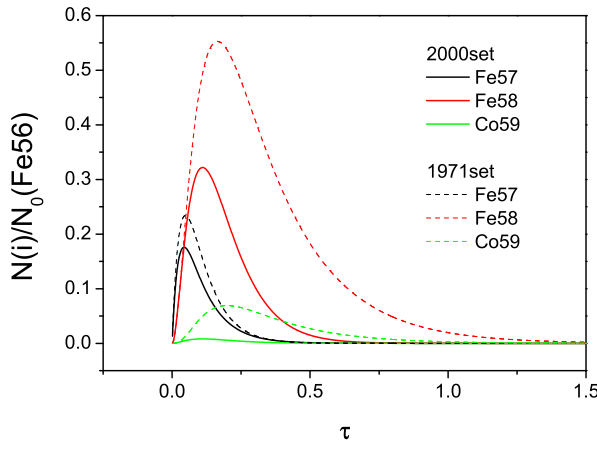


Figure 2: Calculated abundances in function of τ for the iron-family nuclei.

The cross sections of neutron capture in the two sets are also much different for some heavier

nuclei. For example, the neutron capture cross section for ^{140}Ce is 11.0mb and 3.0mb in the 2000set and the 1971set, respectively. Such different cross section data as the inputs can result in much different abundances of ^{140}Ce . As shown in Fig.(3), the 1971set leads to a much larger abundance of ^{140}Ce than the 2000set by a factor of ~ 3 , note that the integrated abundance can be estimated by viewing the area under the curve.

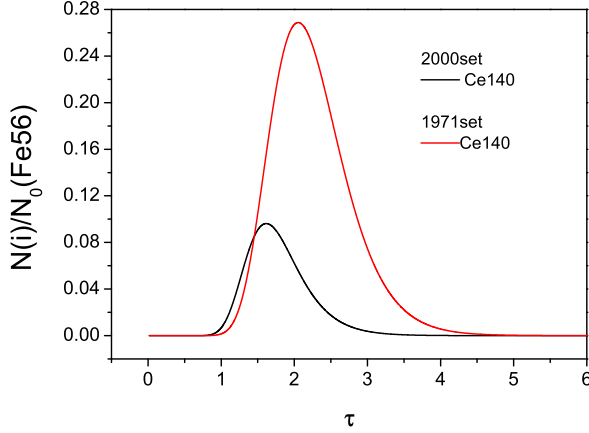


Figure 3: Calculated abundances in function of τ for ^{140}Ce .

About three thousands cross sections of neutron capture on s-process nuclei which are available in the literature are collected and analyzed. Large differences of the cross sections are found not only between the 2000set and the 1971set, as shown in Fig.1, but also between the data from resent years. For example, the cross section of neutron capture on ^{88}Sr is 0.853mb [3]and 5.22mb [4] evaluated in 2004 and 2006, respectively. The s-process simulations have been carried out by using these two values of the cross sections to replace the related data for ^{88}Sr in the 2000set, and the results are shown in Fig.4. These two different cross sections result in very different abundances for ^{88}Sr and nuclei after ^{88}Sr in the chain. The abundance of ^{87}Sr does not change because the input data before ^{88}Sr are exactly same in the two simulations. The ^{89}Y is created through the reaction chain of $^{88}\text{Sr}(n, \gamma)^{89}\text{Sr}(\beta^-)^{89}\text{Y}$ and, therefore, its abundance is much different for the two data sets.

The termination nuclei in the s-process are ^{206}Pb , ^{207}Pb , ^{208}Pb and ^{209}Bi which belong to the Pb-Bi-Po cycle. Their abundances can be changed by changing a single cross section of neutron capture of one of termination nuclei because they are in the cycle. The cross sections of $^{208}\text{Pb}(n, \gamma)^{209}\text{Pb}$ has a value of 0.656mb, evaluated recently (2006) [4] and an alternative value of 0.214mb, evaluated recently (2005) [5], calculated with Hauser-Feshbach method. Each of these two values of cross sections for ^{208}Pb is used to replace the corresponding value in the 2000set, and the resulting two data sets are denoted by the Pb208-2006 and the Pb208-2005, corresponding to $\sigma(^{208}\text{Pb})=0.656\text{mb}$ and 0.214mb , respectively. The $\Phi(\tau)$ for the termination nuclei are calculated by solving the network equations with these two data sets, and the results are shown in Fig.(5) to demonstrate the sensitivity of the abundances of all the termination nuclei to a single cross section

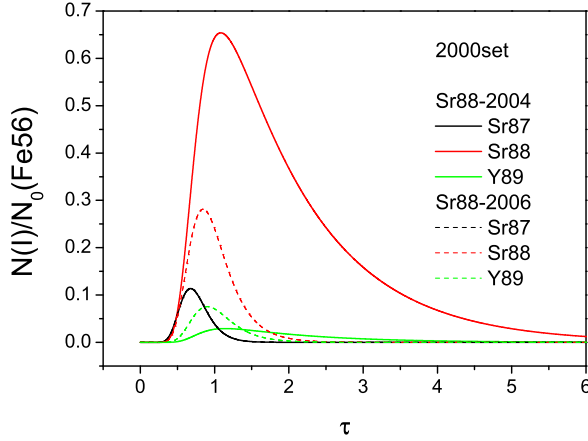


Figure 4: Calculated abundances in function of τ for ^{87}Sr , ^{88}Sr and ^{89}Y by using different cross sections of ^{88}Sr

of neutron capture. It is seen that the saturations of $\Phi(\tau)$ for the termination nuclei are reached at irradiation $\tau > 4\text{mb}^{-1}$ and the saturation values are larger by a factor of ~ 2.5 for the Pb208-2006 set than for the Pb208-2005 set. These results indicate that the nuclear uncertainties in predictions of abundances of *s*-process termination nuclei are large because the cross sections of neutron capture for termination nuclei are still not accurate enough although they have been intensively studied for many years.

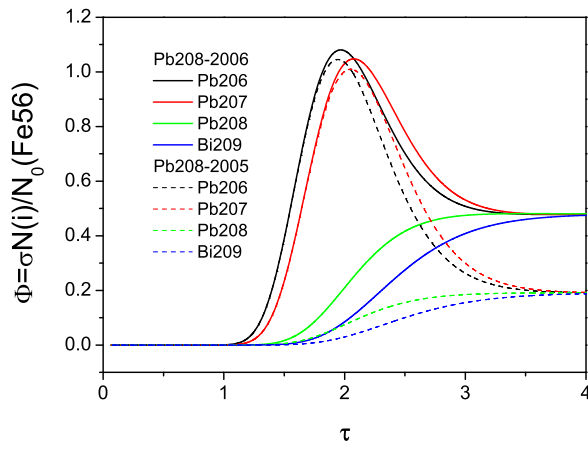


Figure 5: Calculated $\Phi(\tau)$ for the *s*-termination nuclei by using the different cross sections of ^{208}Pb .

4. Summary

In summary, about three thousands of neutron capture cross sections for s-process nuclei available in the literature are collected and analyzed. In order to investigate the nuclear uncertainties in the s-process simulation, the different sets of cross section data are used as the inputs of rates in the network equations with constant temperature and constant neutron density. It has been found that some important neutron cross sections have a large uncertainty, of a factor of 2~4. The calculated abundances for those unique isobar nuclei where their cross sections have such a large uncertainty present a similar large uncertainty. The present results indicate that the nuclear uncertainties in predictions of abundances of quite many s-process nuclei are still large because the corresponding cross sections of neutron capture are not accurate enough. The more accurate measurements of the cross sections of neutron capture on the s-process nuclei which are magic or nearly magic and/or at the branching points are particularly important in more sensitive studies of the s-process problems.

References

- [1] Z.Y. BAO, H. BEER, F. KÄPPELER, F. VOSS, K. WISSHAK and T. RAUSCHER Atomic Data and Nuclear Data Tables **76** (2000) 70.
- [2] B. J. Allen, J. H. Gibbons, and R. L. Macklin, Adv. Nucl. Phys., **4** (1971) 205.
- [3] A. J. Koning, O. Bersillon, R. A. Forrest, R. Jacqmin, M. A. Kellett, A. Nouri, and P. Rullhusen, in Proceedings of the International Conference on Nuclear Data for Science and Technology, Santa Fe, 2004, p. 177.
- [4] M. B. Chadwick, P. Oblozinsky, and M. Herman et al., Nucl. Data Sheets **107** (2006)2931 .
- [5] S. Goriely, Hauser-Feshbach rates for neutron capture reactions (version 8/29/2005), (2005).

Proton spectroscopic factor in ${}^9\text{Be}$ from the angular distribution of ${}^{13}\text{C}({}^9\text{Be}, {}^8\text{Li}){}^{14}\text{N}$

Z. H. Li^{*†}, Y. J. Li, J. Su, B. Guo, K. J. Dong, E. T. Li, X. X. Bai, Z. C. Li, J. C. Liu, S. Q. Yan, B. X. Wang, Y. B. Wang, S. Zeng, G. Lian, X. Liu, S. J. Jin, Q. W. Fan, W. P. Liu
China Institute of Atomic Energy, Beijing 102413, China
E-mail: zhli@ciae.ac.cn
(The present article will be submitted to Phys. Rev. C)

The angular distributions of the ${}^{13}\text{C}({}^9\text{Be}, {}^9\text{Be}){}^{13}\text{C}$ and ${}^{13}\text{C}({}^9\text{Be}, {}^8\text{Li}){}^{14}\text{N}$ reaction were measured with a ${}^9\text{Be}$ beam of 40 MeV for the first time. The proton spectroscopic factor of ${}^9\text{Be}$ ground state was extracted to be 0.73 ± 0.15 by the normalization of the calculational differential cross sections with the distorted-wave Born approximation (DWBA) to the experimental data. The spectroscopic factor was compared to the theoretical and experimental values.

Key Issues of Elements Synthesis in Cosmos
December, 2012
Beijing, China

^{*}Corresponding author.

[†]This work is supported by the National Natural Science Foundation of China under Grant Nos. 11021504 and 10975193, the National Basic Research Programme of China under Grant No. 2013CB834406.

1. Introduction

The ${}^8\text{Li}(p, \gamma){}^9\text{Be}$ capture reaction plays an important role in the inhomogeneous Big Bang nucleosynthesis models, where reactions involving ${}^8\text{Li}$ have a direct bearing on bridging the $A = 8$ mass gap and heavier elements synthesis in the early universe [1]. The cross section of ${}^8\text{Li}(p, \gamma){}^9\text{Be}$ is difficult to be determined directly because of the low intensity of ${}^8\text{Li}$ radioactive beam and the small cross section at the energies of astrophysical interests. Some indirect methods have been employed to extract the direct capture cross section using the direct capture model and the spectroscopic factor. Su et al. firstly deduced the astrophysical S-factors and reaction rates of the ${}^8\text{Li}(p, \gamma){}^9\text{Be}$ reaction by the measurement of the ${}^8\text{Li}(d, n){}^9\text{Be}$ angular distribution in inverse kinematics with a 40-MeV ${}^8\text{Li}$ radioactive ion beam [2]. The extracted proton spectroscopic factor of ${}^9\text{Be}$ is 0.64 ± 0.21 , which is well agreement within experimental error with the values obtained from the ${}^9\text{Be}(t, \alpha){}^8\text{Li}$ angular distribution by both shallow and deep real well potentials[3], but smaller than the shell model calculation of Ref. [4] and the experimental result from the ${}^9\text{Be}(d, {}^3\text{He}){}^8\text{Li}$ reaction at 52 MeV [5]. In 2008, Camargo et al. obtained a larger value of ${}^9\text{Be}$ proton spectroscopic factor from the angular distribution of ${}^9\text{Be}({}^8\text{Li}, {}^9\text{Be}){}^8\text{Li}$ elastic transfer reaction at the angular region of 30-70 degree [6]. Their value is different from the shell model calculation by a factor of C^2 , where $C = \sqrt{2/3}$ is the Clebsch-Gordan coefficient coupling the isospins of ${}^8\text{Li}$ and proton to that of ${}^9\text{Be}$. The authors confused the theoretic value S with C^2S . Up to now, the experimental values of ${}^9\text{Be}$ proton spectroscopic factor disagree with each other by a factor of 1-4. Therefore, a new determination of ${}^9\text{Be}$ proton spectroscopic factor with high precision is desirable.

In this article, we present our resent determination of ${}^9\text{Be}$ proton spectroscopic factor via the measurement of the ${}^{13}\text{C}({}^9\text{Be}, {}^8\text{Li}){}^{14}\text{N}$ angular distribution at $E({}^9\text{Be}) = 40$ MeV with Q3D magnetic spectrometer of HI-13 tandem accelerator, Beijing [7]. The experimental setup has the following advantages to measure the angular distribution precisely. Firstly, the ${}^9\text{Be}$ stable beam is used instead of ${}^8\text{Li}$ radioactive beam, the beam intensity is higher by 5-7 orders of magnitude, the statistics of the reaction production will be high. Secondly, the first peak of the angular distribution can be obtained, which is propitious to the extraction of the spectroscopic factor, since the experimental angular distribution at the backward angles is more sensitive to the inelastic coupling effects and other high-order ones, which cannot be well described theoretically. Thirdly, the energy resolution of the Q3D magnetic spectrometer is 0.02%, it is very well for the identification of the reaction productions.

2. Measurement of the angular distribution

The measurement was performed at the HI-13 tandem accelerator, Beijing. A 40-MeV ${}^9\text{Be}$ beam was delivered and utilized to measure the angular distributions of ${}^{13}\text{C}({}^9\text{Be}, {}^8\text{Li}){}^{14}\text{N}$ and the elastic scattering of its entrance channel (${}^9\text{Be} + {}^{13}\text{C}$). A self-supporting ${}^{13}\text{C}$ target with a purity of 94% and a thickness of $90 \mu\text{g}/\text{cm}^2$ was used in the present experiment. A ${}^{12}\text{C}$ target with the same thickness served as the background measurement. The thickness of the targets was confirmed with the well known angular distribution and an analytical balance with a precision of 1/10000. A movable Faraday cup was placed behind the target to collect the beam for normalization. It covered an angular range of 0-6 degree and thus restricted the attainable minimum angle. The relative

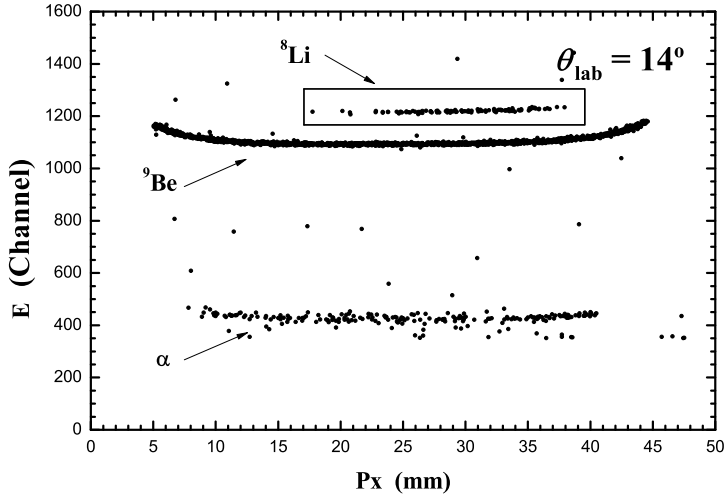


Figure 1: Two dimensional scatter plot of E vs. P_x , which was measured by the PSSD at the magnetic focal plane.

normalization of beam at angles of $\theta_{\text{lab}} \leq 6^\circ$ was carried out by monitoring the elastic scattering events with a $\Delta E - E$ counter telescope placed at 25° downstream of the target. The accepted solid angle of Q3D magnetic spectrometer was set to be 0.34 mSr for a good angular resolution. The reaction products were focused and separated by Q3D, and measured by a $50\text{mm} \times 50\text{mm}$ two-dimensional position sensitive silicon detector (PSSD) at the focal plane. The X-Y information from PSSD enabled the products emitted into the accepted solid angle of Q3D to be fully recorded, and the corresponding energy signals were used to remove the impurities with the same magnetic rigidity.

The ${}^{13}\text{C}({}^9\text{Be}, {}^9\text{Be}){}^{13}\text{C}$ elastic scattering and the ${}^{13}\text{C}({}^9\text{Be}, {}^8\text{Li}){}^{14}\text{N}$ transfer reactions were measured in the angular ranges of $9^\circ \leq \theta_{\text{lab}} \leq 37^\circ$ and $2^\circ \leq \theta_{\text{lab}} \leq 21^\circ$ in steps of 1° , respectively. The typical two dimensional spectrum of kinetic energy versus the position of X-axis at 14° is shown in Fig. 1. One can see that the object ions from the reactions can be clearly identified via the energy and position information. In order to test the correctness of our experiment system, the ${}^{12}\text{C}({}^9\text{Be}, {}^9\text{Be}){}^{12}\text{C}$ angular distribution was firstly be measured and compared with the exist result in Ref. [9]. As can be seen from Fig. 2, the two data agree with each other very well. The obtained ${}^{13}\text{C}({}^9\text{Be}, {}^9\text{Be}){}^{13}\text{C}$ elastic scattering angular distribution is also shown in Fig. 2. The experimental angular distribution of ${}^{13}\text{C}({}^9\text{Be}, {}^8\text{Li}){}^{14}\text{N}$ transfer is shown in Fig. 4 with solid circles. The first peak of ${}^{13}\text{C}({}^9\text{Be}, {}^8\text{Li}){}^{14}\text{N}$ is fully measured with uncertainties of 7%. The uncertainties are mainly from the statistics and uniformity of the target thickness.

3. The proton spectroscopic factor of ${}^9\text{Be}$

The ${}^{13}\text{C}({}^9\text{Be}, {}^8\text{Li}){}^{14}\text{N}$ angular distribution was reproduced with the DWBA code PTOLEMY [8]. Two sets of optical potential parameters with real and imaginary potentials of Woods-Saxon form for the entrance channel were employed in the calculations. They are labeled as En1 and En2 respectively. En1 was determined by fitting the elastic scattering of ${}^{12}\text{C} + {}^9\text{Be}$ at forward angles for incident energies between 20 and 40 MeV [9]. En2 is extracted by fitting the present

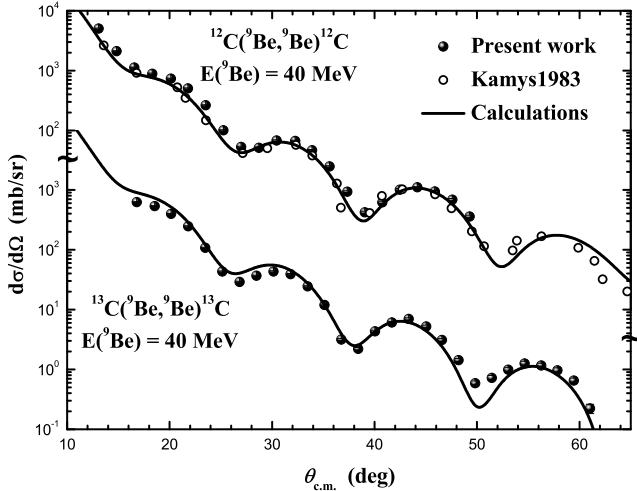


Figure 2: Angular distributions of the ${}^{12,13}\text{C}({}^9\text{Be}, {}^9\text{Be}){}^{12,13}\text{C}$ reaction. The data with solid circles are measured in present work, and that with open circles are from Ref. [9].

${}^{13}\text{C}({}^9\text{Be}, {}^9\text{Be}){}^{13}\text{C}$ angular distribution. Two sets of potential parameters can reproduce the angular distribution very well, as can be seen in Fig. 2. Since no experimental data exist for the ${}^8\text{Li} + {}^{14}\text{N}$ elastic scattering, the angular distributions of the ${}^{13}\text{C}({}^7\text{Li}, {}^7\text{Li}){}^{13}\text{C}$ at $E({}^7\text{Li})= 34$ MeV were used to derive the potential parameters for the exit channels. We can see from Fig. 3 that the optical potential parameters labeled with Ex1 and Ex2 can reproduce the experimental data very well. Where Ex1 is chosen from Ref. [10], and Ex2 is extracted by our previous work [11]. All the potential parameters are listed in table 1. For calculating the wave functions of the bound states, the Woods-Saxon potentials with the standard geometrical parameters $r_0 = 1.25$ fm and $a = 0.65$ fm were adopted, and the potential depths were adjusted automatically to reproduce the proton binding energies of ${}^9\text{Be}$ ground state.

The ${}^{13}\text{C}({}^9\text{Be}, {}^8\text{Li}){}^{14}\text{N}$ reaction leading to the ground state of ${}^9\text{Be}$ is a $(3/2^-, 1/2) \rightarrow (2^+, 1)$ transition. Both $p_{1/2}$ and $p_{3/2}$ orbital will contribute to the ${}^{13}\text{C}({}^9\text{Be}, {}^8\text{Li}){}^{14}\text{N}$ reaction. According to our previous work [11] and the theoretical calculations [4, 12]. The $p_{3/2}$ component in ${}^{14}\text{N}$ is less than 1% and can be neglect in the DWBA analysis. The relationship among the experimental differential cross sections, the calculations and the spectroscopic factors can be expressed as

$$\left(\frac{d\sigma}{d\Omega}\right)_{exp} = S_{14\text{N}} \left[S_{9\text{Be}}^{3/2} \left(\frac{d\sigma}{d\Omega}\right)_{3/2} + S_{9\text{Be}}^{1/2} \left(\frac{d\sigma}{d\Omega}\right)_{1/2} \right], \quad (3.1)$$

where $\left(\frac{d\sigma}{d\Omega}\right)_{exp}$ is the experimental differential cross section, $\left(\frac{d\sigma}{d\Omega}\right)_{3/2}$ and $\left(\frac{d\sigma}{d\Omega}\right)_{1/2}$ are the calculational differential cross sections contribute by the $p_{3/2} \rightarrow p_{1/2}$ and $p_{1/2} \rightarrow p_{1/2}$ transition, respectively. $S_{14\text{N}}$ is the spectroscopic factor for ${}^{14}\text{N} \rightarrow {}^{13}\text{C} + p$, which is derived to be 0.67 ± 0.09 from Ref. [11]. $S_{9\text{Be}}^{3/2}$ and $S_{9\text{Be}}^{1/2}$ are the proton spectroscopic factors of the $p_{3/2}$ and $p_{1/2}$ components in ${}^9\text{Be}$ ground state, and their ratio is determined to be 8.81 by the shell model calculations in Ref. [4]. The proton spectroscopic factors in ${}^9\text{Be}$ can be extracted through Eq. (3.1) by the normalization of DWBA calculations to the experimental differential cross sections.

The normalized angular distributions calculated with the above mentioned optical potentials are presented in Fig. 4 together with the experimental data. The solid, dashed, dotted and dash-

Table 1: Optical potential parameters used in DWBA calculations, the depths are in MeV, the geometry parameters in fm, the geometrical parameters of single particle bound state are set to be $r_0 = 1.25$ fm and $a = 0.65$ fm.

Set No.	En1	En2	Ex1	Ex2
V	33.69	127.0	159.0	198.75
r_r	0.97	0.80	0.63	0.52
a_r	0.92	0.78	0.81	0.90
W_V	6.52	13.9	8.16	8.7
r_v	1.51	1.25	1.33	1.31
a_v	0.48	0.70	0.78	0.73
Ref.	[9]	This work	[10]	[11]

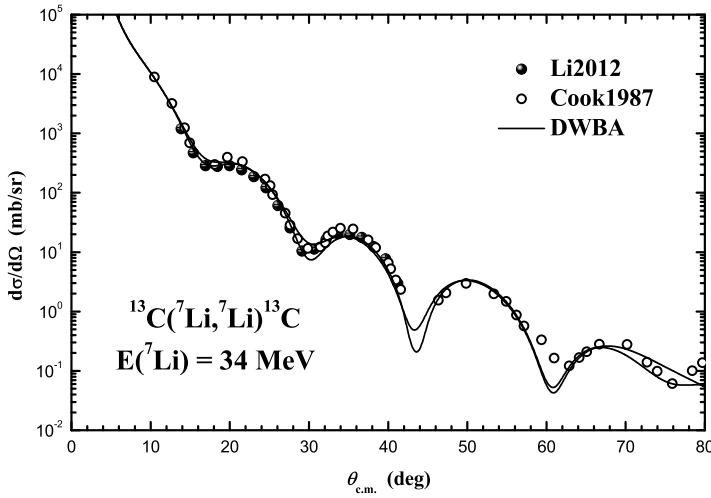


Figure 3: Angular distributions of the ${}^{13}\text{C}({}^7\text{Li}, {}^7\text{Li}){}^{13}\text{C}$ elastic scattering at $E_{lab} = 34$ MeV. The experimental data are taken from Ref. [11] (solid circles) and Ref. [10] (open circles).

dotted curves are the angular distribution calculated with the combination of En1-Ex1, En1-Ex2, En2-Ex1 and En2-Ex2 optical potential parameters. One can see that the first peak of the experimental angular distribution is well reproduced by all the optical potentials. The extracted spectroscopic factors are 0.71, 0.77, 0.76 and 0.67, respectively. Their average is 0.73 ± 0.15 . The uncertainties are mainly from the measurement (10%), the divergence of optical potential parameters (7%), the uncertainties of geometric potential parameters (10%) and the error of the ${}^{14}\text{N}$ proton spectroscopic factors (13%).

The spectroscopic factors in ${}^9\text{Be}$ ground state obtained in theoretical and experimental investigations are plotted in Fig. 5, together with the previous results in Refs. [4, 3, 5, 2, 6]. The present value is in good agreement with those derived from the ${}^9\text{Be}(t, \alpha){}^8\text{Li}$ [3] and ${}^8\text{Li}(d, n){}^9\text{Be}$ [2] reactions within the experimental error, and slightly smaller than that from the shell model calculation [4] and the ${}^9\text{Be}(d, {}^3\text{He}){}^8\text{Li}$ reaction [3]. The value obtained from ${}^9\text{Be}({}^8\text{Li}, {}^9\text{Be}){}^8\text{Li}$ elastic transfer reaction is larger than the present result by a factor of 2.3. With the experimental data having errors, a weighted average value of ${}^9\text{Be}$ proton spectroscopic factor is deduced to be 0.93 ± 0.25 . The

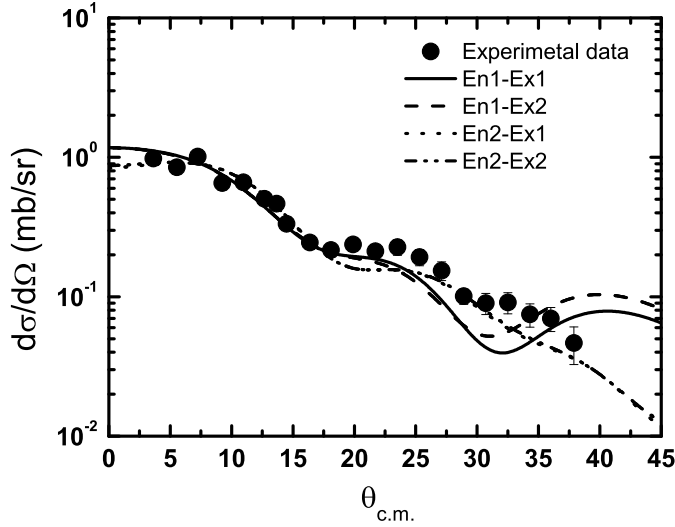


Figure 4: The experimental and calculated ${}^{13}\text{C}({}^9\text{Be}, {}^8\text{Li}){}^{14}\text{N}$ angular distributions at $E_{lab} = 40.0$ MeV.

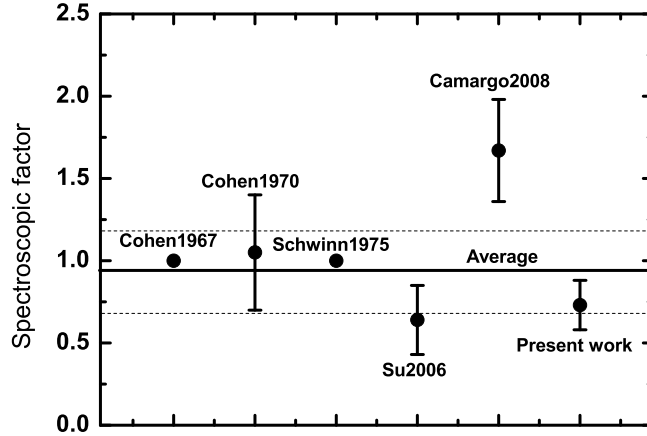


Figure 5: Comparison of the present ${}^9\text{Be}$ proton spectroscopic factor with the previous results in Refs. [2, 3, 4, 5, 6]. The solid line is the weighted average value of the experimental results and the dashed line represents the weighted errors.

appropriate value can be used for the calculation of the ${}^8\text{Li}(p, \gamma){}^9\text{Be}$ cross section.

4. Summary

The angular distributions of the ${}^{13}\text{C}({}^9\text{Be}, {}^9\text{Be}){}^{13}\text{C}$ elastic scattering and the ${}^{13}\text{C}({}^9\text{Be}, {}^8\text{Li}){}^{14}\text{N}$ transfer reaction at $E_{lab} = 40$ MeV have been determined with a high precision Q3D magnetic spectrometer. The optical model calculations can reproduce the angular distributions of elastic scattering and transfer reactions. The proton spectroscopic factor of ${}^9\text{Be}$ ground state was extracted from the comparison between the experimental differential cross sections and optical model calculations with DWBA code PTOLEMY. The present value was compared to the theoretical and

experimental ones. A weighted average value was deduced and will be used to calculate the astrophysical S-factor for the direct capture of the ${}^8\text{Li}(p, \gamma){}^9\text{Be}$ reaction.

Acknowledgments

The authors thank the staff of Tandem Accelerator for their technical assistance during accelerator operations. This work is supported by the National Natural Science Foundation of China under Grant Nos. 11021504 and 10975193, the National Basic Research Program of China under Grant No. 2013CB834406.

References

- [1] T. Kajino and R. N. Boyd, *Astrophys. J.* **359**, 267(1990).
- [2] J. Su, Z. H. Li, B. Guo et al. *Chin. Phys. Lett.* **23**, 55(2006).
- [3] L. Cohen and G. H. Herling, *Nucl. Phys.* **A141**, 595(1970).
- [4] S. Cohen and D. Kurath, *Nucl. Phys.* **A101**, 1(1967).
- [5] U. Schwinn, G. Mairle, G. J. Wagner et al. *Z. Phys.* **A275**, 241(1975).
- [6] O. Camargo, V. Guimarães, R. Lichtenthäler et al. *Phys. Rev. C*, **78**, 034606(2008).
- [7] Z. C. Li, Y. H. Cheng, C. Yan et al. *Nucl. Instrum. Methods Phys. Res. A* **336**, 150(1993).
- [8] I. J. Thompson, *Comput. Phys. Rep.* **7**, 167(1998).
- [9] B. Kamys, L. Jarczyk, A. Strzalkowski et al. *Nucl. Phys.* **A406**, 193(1983).
- [10] J. Cook, M. N. Stephens, and K. W. Kemper. *Nucl. Phys.* **A466**, 168(1987).
- [11] Y. J. Li, Z. H. Li, E. T. Li et al. *Eur. Phys. J. A* **48**, 13(2012).
- [12] N. K. Timofeyuk, *Phys. Rev. C* **81**, 064306(2010).

Stellar neutron in laboratory

Yan Shengquan*, Zhang Weijie, Jin Sunjun, Li yunju, Bai Xixiang, Li Zhihong, Wang Youbao, Lian Gang, Zeng Sheng, Guo Bing, Su Jun

Chinese Institution of Atomic Energy, Beijing 102413, China

E-mail: yanye7703@sina.com

A Maxwell-boltzmann distribution neutron flux at $kT=22$ keV was obtained via the $^7\text{Li}(p, n)^7\text{Be}$ reaction, the experiment was carried out on 1.7×2 MV tandem-accelerator in China Institute of Atomic Energy. 3.4 MeV proton from accelerator passed through a $60.5 \mu\text{m}$ aluminum foil and impinged on natural LiF target, where, proton energy was reduced and shaped as a gaussian distribution with mean nearly 1.90 MeV and deviation 0.05 MeV. Neutron with emission angle $65 \pm 2.6^\circ$ was collected.

Key Issues of Elements Synthesis in Cosmos
December, 2012
Beijing, China

*Corresponding author.

1. Introduction

Slow neutron capture process(s-process) play an important role in stellar nucleosynthesis, nearly 50% elements heavier than iron are produced by s-process in stars. $^{13}\text{C}(\alpha, \text{n})^{16}\text{O}$ and $^{22}\text{Ne}(\alpha, \text{n})^{25}\text{Mg}$ are considered the main neutron source for s-process. Because neutrons will be quickly thermal populated in the dense stellar plasma, energy of neutrons could be described by a Maxwell-Boltzmann distribution,

$$\phi(E) \sim E_n \exp(-E_n/kT),$$

where k is Boltzmann's constant and T is the absolute temperature in kelvins. The sites where nuclide capture neutron are believed in He and C shell of stars, temperature there is about 90 MK to 1 GK. After thermal population, energy region of neutron inside will cover about 0.1 to 500 keV.

To study the stellar nucleosynthesis in s-process, reaction rate is needed as a fundamental input for network. reaction rate per particle pair could be written as

$$\langle \sigma v \rangle = \left(\frac{8}{\pi \mu} \right)^{1/2} \frac{1}{(kT)^{3/2}} \int_0^\infty \sigma_{(n,\gamma)}(E_n) E_n \exp(-\frac{E_n}{kT}) dE \quad (1.1)$$

Usually, Neutron capture cross section is measured by Time of flight(TOF) method with pulse neutron source, then reaction rate could be calculated by convolution integral of (n, γ) cross-section and Maxwell-Boltzmann energy distribution of neutrons. However, for (n, γ) cross-section of heavy nuclide, there are many narrow-resonances crowded near about 5-80 keV, TOF technique could not measure the narrow-resonances very precisely because of resolution of TOF. There are many stellar (n, γ) cross-section with the uncertainty larger than 10%, one of the reasons is the cross-section uncertainty due to narrow-resonances.

A technique that measured the reaction rate directly with Maxwell-Boltzmann neutrons was established early by Kappler etc in 1980[1], where the neutron could simulate thermal neutron at $kT=25$ keV in stars. With technique, the measurement of cross-section for each energy point is not necessary and cross-section uncertainty due to narrow-resonance could be avoided in reaction rate measurement. In Kappler's work, neutron was produced by $^7\text{Li}(p,n)^7\text{Be}$ with proton energy $E_p=1.912$ MeV, the Maxwell-boltzmann neutron was collected by integrating all neutron in forward cone with angle 120° . Activation method was used to measure the (n, γ) reaction rate and measurement was limited in reactions with unstable residual nuclei.

Comparing Kappler's work, we obtained a Maxwell-Boltzmann neutron with $E=KT=22$ keV, and the emission angle of neutrons was $65 \pm 2.6^\circ$. Because of the small solid angle and different Maxwell-Boltzmann neutron energy in our work, different stellar temperature could be simulated, and the measurement of reaction rate for all s-process nuclide is possible.

2. Measurement

The experiment was carried out at 1.7×2 MV tandem accelerator in China Institute of Atomic Energy, the experimental terminal had been optimized for neutron experiment with low background. $^7\text{Li}(p,n)^7\text{Be}$ was used to produce the Maxwell-boltzmann neutron, As figure 1 showed, proton beam with energy $E_p=3.4$ MeV from tandem accelerator passed through a 60.5 micron aluminum foil and then bombarded on the nature LiF target. A $\phi 2 \times 1$ inch ^6Li glass detector was used to measure neutron with time of flight technique.

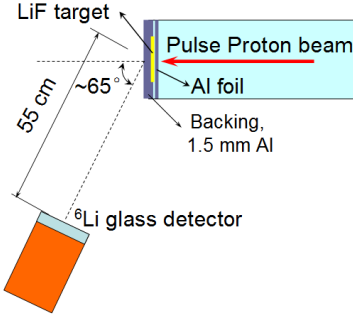


Figure 1: Experiment setup

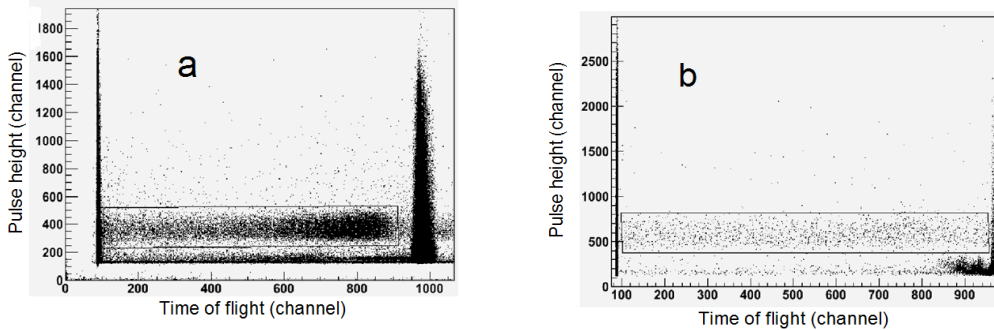


Figure 2: Time of flight spectrum for the ${}^6\text{Li}$ -glass detector, box is the neutron area.(a) is the measurement without shadow cone, (b) is the measurement with a shadow cone in front of detector.

In measurement, Al foil was used to reduce energy and expand energy distribution of proton from accelerator. After the Al foil, proton beam would be shaped as gaussian energy distribution with the mean nearly 1.886 MeV, which is the energy threshold of ${}^7\text{Li}(\text{p},\text{n}){}^7\text{Be}$ reaction. LiF target was evaporated on a 1.5 mm Al backing, target thickness was 2.0 mg/cm^2 . Proton with gaussian energy distribution would be expended again because the different reaction depth in target, the expanded proton with different energy will produce neutron in deferent energy in same emission angle. Neutron with the emission angle 65 degree and solid angle 5.2 degree will be obtained.

${}^6\text{Li}$ glass detector was mounted on an arm that could be rotated around target, the distance between target and detector was 55 cm. The repetition rate of proton beam from accelerator was 1 MHz, and pulse width was 3 ns. Time of flight spectrum of neutron was shown in figure 2,

In background measurements, a shadow cone with size $\phi 20 \times 50 \text{ cm}$ was placed between detector and target. With the shadow cone, neutron from target will be stopped and scattering neutron from other place will be measured as background. The background TOF spectrum was shown in figure 2(b).

3. Neutron spectrum

The detector used in experiment is the GS20 ${}^6\text{Li}$ -glass detector from Saint-Gobain company,

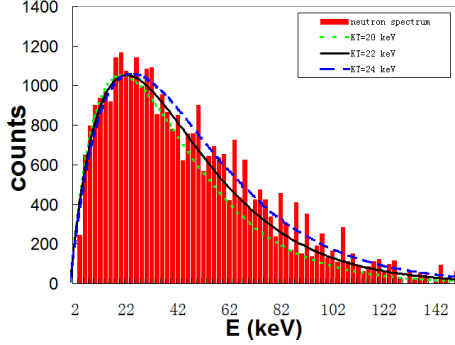


Figure 3: neutron spectrum with 2 keV energy bin, the emission angle was 65 ± 2.6 degree. Curves were theoretical Maxwell-boltzmann distributions

the size of crystal is $\phi 2 \times 1$ inch and ${}^6\text{Li}$ content is 1.58×10^{22} atom/cm 3 . With the parameters of ${}^6\text{Li}$ -glass detector, MCNP code was used to calculate the efficiency of neutron detection. After the efficiency correction, neutron spectrum could be obtained by subtracting normalized background with shadow cone, as figure 3 show,

The neutron spectrum was agree well with the Maxwell-boltzmann distribution at $kT=22$ keV, as figure 3 showed. Comparing our work to Kappler's, the neutrons had different thermal energy and small solid angle. With small solid angle, secondary target for (n, γ) reaction could be set far away from the primary LiF target and shielding management could be adopted for γ detection in (n, γ) reaction, in this case, reaction rate measurement for all s-process nuclide is possible.

References

- [1] H. Beer and F. Kappler. Phys. Rev. C, 1980, **21**: 534—544

Study of the astrophysical ${}^4\text{He}(\text{np},\gamma){}^6\text{Li}$ reaction rate in a novel quasi-deuteron capture mechanism

Hou Su-qing^{1,2,3*}, He Jian-jun¹, Chen Yong-shou³, Li Zhi-hong³

¹ Institute of Modern Physics, Chinese Academy of Sciences, Lanzhou 730000, China

² University of Chinese Academy of Sciences, Beijing 100049, China

³ China Institute of Atomic Energy, Beijing 102413, China

E-mail: sqhou@impcas.ac.cn

Enlightened by the dineutron-capture mechanism, recalculation of the astrophysical ${}^4\text{He}(\text{np},\gamma){}^6\text{Li}$ reaction rate was recalculated in a similar framework in which a quasi-deuteron is captured by ${}^4\text{He}$ and subsequently formed ${}^6\text{Li}$. We have attempted to study the effect of this new rate on the lithium abundance in a standard Big Bang Nucleosynthesis (BBN) model, some preliminary results are reported.

Key Issues of Elements Synthesis in Cosmos
December, 2012
Beijing, China

*Corresponding author.

1. introduction

The consistency of the measured abundances of deuterium and ${}^4\text{He}$ relative to hydrogen with the predictions of the standard Big-Bang Nucleosynthesis (BBN) model is a major triumph of modern cosmology. However, there remain significant discrepancies between observations and predictions for the absolute abundances in ${}^7\text{Li}$ and ${}^6\text{Li}$ nuclide. Similar to the ${}^7\text{Li}$ case, the ${}^6\text{Li}$ abundance observed in metal-poor halo stars exhibits a plateau as a function of metallicity, suggesting a big bang origin. While inferred primordial abundance of ${}^6\text{Li}$ is larger than BBN prediction by 3 orders of magnitude. Also, the inferred ${}^7\text{Li}$ abundance is 3 times smaller than the BBN prediction. In the past 20 years, those discrepancies between the prediction and the observation were not solved. In the standard BBN model, possible solutions of the "lithium problems" from nuclear physics aspect might rely on still are that a larger reaction network. An exhausted BBN network, involving those reactions induced by the short-lived nuclei, was implemented for solving the ${}^6\text{Li}$ problem by Boyd et al [1], and it was found that these additions only had little effect on the final BBN abundances. All reactions involved in the past BBN calculation are two-body reactions. In this work we introduce a three-body ${}^4\text{He}(np,\gamma){}^6\text{Li}$ reaction into our network calculation and try to address the ${}^6\text{Li}$ problem in an attentive way.

In the past, two mechanisms for three-body reaction ${}^4\text{He}(2n,\gamma){}^6\text{He}$ were devised [2]. One is a sequential neutron-capture mechanism which the unbound ${}^5\text{He}$ is formed as an intermediate state; another is the formation of an intermediate state of in a form of dineutron. Although both mechanisms form an intermediate particle-unbound component, in equilibrium between formation and decay, their time sequence is totally different. It shows that the ${}^4\text{He}(2n,\gamma){}^6\text{He}$ rate can be enhanced by several orders of magnitude by dineutron-capture mechanism relative to sequential two neutron-capture mechanism. Enlightened by this dineutron-capture mechanism, the ${}^4\text{He}(np,\gamma){}^6\text{Li}$ reaction rate is studied via the quasi-deuteron one-step capture mechanism.

2. Quasi-deuteron formation rate

In previous study [3], the quasi-deuteron formation of ${}^6\text{Li}$ which pictures ${}^6\text{Li}$ as an alpha core with an orbiting deuteron was investigated experimentally, however, the expected results had not been achieved. But still no strong evidence does show that this type of mechanism don't exist in nature. Here we propose the n-p correlated nucleus(quasi-deuteron) exists in a quasi-deuteron form, which is very loosely bounded. With the experimental n-p scattering cross-section data, we calculated the reaction rate of quasi-deuteron as shown in Fig. 1. The rate of ${}^1\text{H}(n,\gamma){}^2\text{H}$ is also shown for comparision. It is found that the rate of forming quasi-deuteron is larger than that of ${}^1\text{H}(n,\gamma){}^2\text{H}$ by 4 orders of magnitude. However, this might not enhance the abundance of ${}^6\text{Li}$ dramatically as the binding energy of quasi-deuteron is so small that it will be dissociated by the photons quickly. Its practical impact should be checked by the later BBN calculation.

3. Three-body rate of ${}^4\text{He}(np,\gamma){}^6\text{Li}$

Nowadays, the three-body reaction rate following the method used in the dineutron capture in Ref [5] is being calculated. The reaction rate of the three-body reaction can be described by a

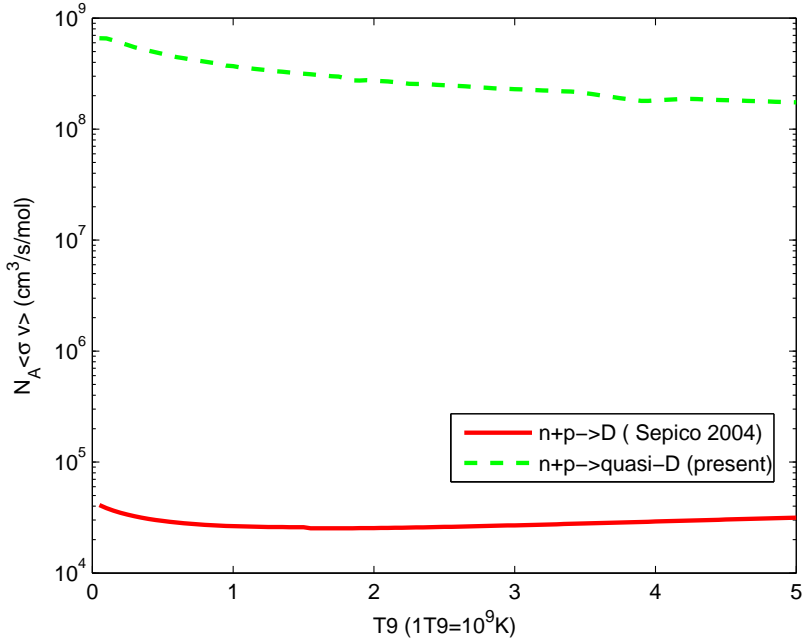


Figure 1: Reaction rate for quasi-deuteron forming via n-p scattering. The recent rate [4] for $p(n,\gamma){}^2\text{H}$ is shown for comparison.

double integral,

$$N_A^2 \langle 1pn \rangle = N_A^2 \int_{E_1} \frac{d \langle (p,n) \rangle (E_1)}{dE_1} \frac{2\hbar}{\Gamma_2(E_1)} \times \left[\int_{E_2} \frac{d \langle (d,\gamma) \rangle (E_1, E_2)}{dE_2} dE_2 \right] dE_1 \quad (3.1)$$

Here, $\Gamma_2(E_1)$ is the energy-dependent width of quasi-deuteron, and E_1 and E_2 denotes the collision energy in the center-of-mass system. The differential represent the integrands of the $\langle \sigma v \rangle$ integration for the single-step reaction rate and is described by

$$\frac{d \langle \sigma v \rangle}{dE} = \sqrt{\frac{8}{\pi\mu}} \frac{1}{(kT)^{3/2}} \sigma(E) E \exp\left(-\frac{E}{kT}\right) \quad (3.2)$$

The cross section of the formation of quasi-deuteron was calculated as discussed above, and the analytic expression is obtained by fitting the n-p scattering data. The width of quasi-deuteron virtual state of a 0^+ resonance was about $\Gamma_2(E_1) = 9e-8$ MeV derived from the n-p scattering curve. The loosely bounded quasi-deuteron might have a bigger radius than a real deuteron, and this possibly results in a larger (α, γ) cross section as well. The detail effect is now under evaluation. For simplicity, here we can take the cross section of ${}^2\text{H}(\alpha, \gamma){}^6\text{Li}$ as that of quasi-deuteron capture on ${}^4\text{He}$, which gives the lower limit of ${}^4\text{He}(np, \gamma){}^6\text{Li}$ rate. The calculation of the ${}^4\text{He}(np, \gamma){}^6\text{Li}$ rate is still in progress.

References

- [1] R.N.Boyd et al., Phys. Rev. D. , **82** (2004) 105005

- [2] Amy Bartlett et al., Phys. Rev. C. **74** (2006) 015802
- [3] D.G.Proctor, W.H.Voelker, Phys. Rev. , **118** (1960) 217
- [4] P.D.Serpico et al., JCAP **12** (2004) 010
- [5] K.Nomoto et al., Astron. Astrophys. **149** (1985) 239

Silicon abundances in nearby stars from the Si I infrared lines

J.R. Shi^{*†}, M. Takada-Hidai², Y. Takeda³, K.F. Tan¹, S.M. Hu⁴, G. Zhao¹, C. Cao⁴

¹Key Laboratory of Optical Astronomy, National Astronomical Observatories, Chinese Academy of Sciences, Beijing 100012, P. R. China

²Liberal Arts Education Center, Tokai University, 4-1-1 Kitakaname, Hiratsuka, Kanagawa 259-1292, Japan

³National Astronomical Observatory of Japan 2-21-1 Osawa, Mitaka, Tokyo 181-8588, Japan

⁴Shandong Provincial Key Laboratory of Optical Astronomy and Solar-Terrestrial Environment, Shandong University at Weihai, 264209, P. R. China

E-mail: sjr@bao.ac.cn

We have used high-resolution, high signal-to-noise ratio infrared spectra from the Subaru Telescope atop Mauna Kea. Line formation calculations of Si I infrared lines in the atmospheres of nearby stars are presented. All abundance results of [Si/Fe] are derived from local thermodynamic equilibrium (LTE) and NLTE statistical equilibrium calculations and spectrum synthesis methods. We found that NLTE effects for Si I infrared lines are important even for metal-rich stars (>0.1 dex), and the NLTE effects may depend on the surface gravities. A good agreement of silicon abundances between the optical and infrared lines are obtained when the NLTE effects are included, while a large difference found for the LTE results. The derived silicon abundances show overabundant for metal-poor stars.

Key Issues of Elements Synthesis in Cosmos
December, 2012
Beijing, China

*Corresponding author.

†This research was supported by the National Natural Science Foundation of China under grant Nos. 11021504, 10878024, 10973016, 10821061, 10778701 and 11103034, by the foundation of Shandong University at Weihai No. 2010ZRYB003. One of the authors (M. T.-H.) is grateful for a financial support from a Grant-in-Aid for scientific research (C, No. 22540255) from the Japan Society for the Promotion of Science.

1. Introduction

Silicon is an important α -capture element, whose abundances play a key role in studying the Galactic chemical evolution. It is believed that silicon is made during oxygen and neon burning in massive stars [52, 37], and type Ia supernovae also produce significant amounts of silicon [50, 24, 47, 33].

The previous abundance determinations of Si have been based on the optical lines and the assumption of local thermodynamic equilibrium (LTE). For extreme-metal poor stars, the only optical lines at 3905 and 4103 Å can be used to determine Si abundances. Recently, it is found that the infrared SiI lines can also be observed [25] for metal-poor stars. However, we noted that the infrared lines are sensitive to the NLTE effects even in the solar spectrum [40]. Thus, it is important to investigate the NLTE effects for these infrared lines in metal-poor stars.

The present work is based on a sample of nearby stars and aims at exploring their [Si/Fe] abundance ratios based on the SiI infrared lines, applying a full spectrum synthesis based on level populations calculated from the statistical equilibrium equations, and to investigate whether similar silicon abundances can be obtained from the infrared and optical lines. In Sect. 2 we present the observational technique and the atmospheric models, and stellar parameters are discussed in Sect. 3. NLTE line formation is discussed in Sect. 4. The results and comparison with these from the optical lines are shown in Sec. 5. The discussion and conclusions are presented in Sect. 6.

2. Observations

The high-resolution spectra analyzed in our present investigation were obtained with the Infrared Camera and Spectrograph [26, 49, IRCS] along with the 188-element curvature-based adaptive optics system (AO188), which is mounted on the IR Nasmyth focus of the 8.2 m Subaru Telescope atop Mauna Kea on 2009 July 29 and 30 (UT). The observations cover a spectral range from 10 100 to 11 900 Å. The spectra were taken in the échelle spectrograph mode of IRCS, which is equipped with a Raytheon 1024×1024 InSb array with an Aladdin II multiplexer. The spectral resolution of R is $\simeq 20\,000$. All stars were observed with S/N ~ 100 to 300.

For HD 131156, high-resolution and high S/N optical spectra were obtained with the fiber optics échelle spectrograph attached to the 2.16 m telescope at National Astronomical Observatories (Xinglong China) on 2011 August 3. The observations cover a spectral range from 3700 Å to 9200 Å. The spectra were exposed on a 4096² CCD chip with 12 μm pixel size, providing a spectral resolving power of R $\sim 50\,000$. It were observed six times with S/N ~ 200 .

Data extraction followed the standard “échelle” package of the software IRAF¹ including subtraction for background cancelation, flat-fielding, bad-pixel correction, cosmic-ray events correction, scattered-light subtraction, aperture extraction, wavelength calibration, co-adding of spectrum frames, and continuum normalization [45, 46, for details].

¹ IRAF is distributed by the National Optical Astronomy Observatories, which is operated by the Association of Universities for Research in Astronomy, Inc. under cooperative agreement with the National Science Foundation.

3. Method of calculation

3.1 Model atmospheres

We use line-blanketed LTE model atmospheres, generated by [19]. As shown by [18] this model is almost identical to the more generally known model of [29]. The main characteristics are: the iron opacity was calculated with the improved meteoritic value $\log \varepsilon_{\text{Fe}} = 7.51$ [4]; opacities for metal-poor stars with $[\text{Fe}/\text{H}] < -0.6$ were calculated using α -element abundances enhanced by 0.4 dex, and the mixing-length parameter l/H_p was adopted to be 0.5, in order to determine consistent temperatures for H_{α} and the higher Balmer lines [18]. [23] discussed in detail our MAFAGS-OS and ODF models, and the differences with the MARCS and Kurucz models.

3.2 Stellar parameters

We adopt the stellar parameters for the sample stars determined by [21, 22] and [42], where the effective temperatures are derived from the wings of the Balmer lines based on the hydrogen resonance broadening calculated with [2] theory. The surface gravities are based on the HIPPARCOS parallaxes. Iron abundances are obtained from Fe2 lines, and the microturbulence velocities are estimated by requiring that the iron abundance derived from Fe 2 lines should not depend on equivalent width. For G 29-23, fortunately, high-resolution and high S/N spectra covering a wide wavelength range were available from the archived ESO VLT/UVES [15] spectra database. In order to keep our analysis consistent, for G 29-23 and HD 131156 we determined the stellar parameters using the method described above. The estimated uncertainties for the temperature, surface gravity, metal abundance, and microturbulence velocity are for most of the stars as ± 80 K, 0.10 dex, 0.05 dex and 0.2 km s^{-1} , respectively.

3.3 Atomic line data

Table 1 lists the relevant line data with their final solar NLTE fit values [40]. Collisional broadening through van der Waals interaction with hydrogen atoms is important for infrared Si lines. The damping constants $\log C_6$ for Si1 infrared lines are computed according to the table from [5, 6] and [9]. It is found by [20, 21] that the values of the van der Waals damping constants, such as Fe, Na, Mg and Al etc, can be best described by those calculated from the tables of [5, 6] and [9]. In our analysis, the absolute value of the oscillator strengths is unimportant because the abundances are evaluated in a fully differential way with respect to the sun.

4. NLTE calculations

4.1 Atomic model

The silicon model atom includes the most important levels of Si1 and Si2 and comprises 132 terms of Si1, 41 terms of Si2, plus the Si3 ground state. As usual, the *level system* of silicon was extracted from the NIST data bank². Silicon in cool stars is fully represented by the first three ionization stages, where for the purpose of NLTE calculations Si3 reduces to the ground state, $3s^2 1S$. The atomic properties are documented in [40, 41].

²<http://www.physics.nist.gov/>

Line transitions are based on the work of the Opacity Project [39], in particular the calculations of [35]. The total number of lines included is 786 for Si1 and 182 for Si2. For NLTE transfer calculations simple Gauss profiles were used with 9 wavelength points each.

Bound-free transition cross-sections with complex structure are available from calculations at the TOPbase³ (see also[35]). The cross-sections of the lowest three terms, $3p^3P$, $3p^1D$ and $3p^1S$ are an order of magnitude greater than those of the next terms, which is very similar to the configuration of Mg [53]. It tends to decouple the metastable terms efficiently from the excited ones.

Background opacities are calculated with an opacity sampling code based on the hydrogen lines, the line lists made available by [30], and on the important bound-free cross-sections of hydrogen and the most abundant metals. The background opacities are sampled on a *random grid* of between 5000 and 10 000 wavelengths, to which are added the wavelengths of the line profiles. The final NLTE line formation program thus samples roughly 14 000 wavelengths. In the UV, where most of the background opacity is expected, the wavelength intervals of the random grid are between 1 and 4 Å. We emphasise that the choice of this frequency grid affects only the *bound-free* radiative interaction rates. The earlier experiments with a finer frequency mesh of up to 40 000 randomly sampled frequencies for Fe1 [20] showed that the influence of a very dense frequency sampling is less than marginal. This is similar to the sampling situation for OS model atmospheres, where changes in temperature corrections drop below a few K when the number of frequencies is increased to values beyond 10 000 [23, Fig. 8]. Background opacities for *bound-bound* transitions are sampled at the corresponding line frequencies.

Inelastic collisions with electrons and hydrogen atoms for both excitation and ionization are taken into account in our Si NLTE calculations. The formulae of [51] and [3] are used to describe the excitation of allowed and forbidden transitions by electron collisions, respectively. Ionization cross-sections for electron collisions are calculated applying the formula of [38]. [16, 17] formula as described by [44] is used to calculate neutral hydrogen collisions, with a similar formula for bound-free hydrogen collisions. To allow for some empirical correction to the Drawin approximations, a scaling factor S_H is applied to the formula in our calculations.

The variation of the hydrogen collision scaling factor S_H between 0 and 1 allows us to introduce similar changes as those resulting from electron collisions. Due to the large number of hydrogen atoms, the neutral hydrogen collision rates can be significantly stronger than the electron collision rates. *For the Sun*, in the range of S_H parameters considered here, they do not lead to significant changes in the line profiles in the visible, where, abundance differences for the two extremes ($S_H=0$ and 1) stay within 0.03 ... 0.04 dex. This situation changes significantly, when the Si1 near-infrared lines are analyzed. As is evident from Table1 most of these are absorbed from either $4s^3P^o$, $4p^1P$, or $4p^3D$. Since all the excited terms are only loosely coupled to each other and to other high-excitation terms, their departure coefficients tend to diverge from each other at $\log \tau \simeq -2$, see [40, Fig.4], i.e. where the *cores* of the relatively strong near-infrared lines form. This is the reason for a slightly increased abundance trend going with the hydrogen collision scaling factor. For lines beyond 1 μm the corresponding abundance variations can reach more than 0.1 dex, and their cores suggest the choice of $S_H = 0.1$ (Fig.1).

³<http://vizier.u-strasbg.fr/topbase/topbase.html>

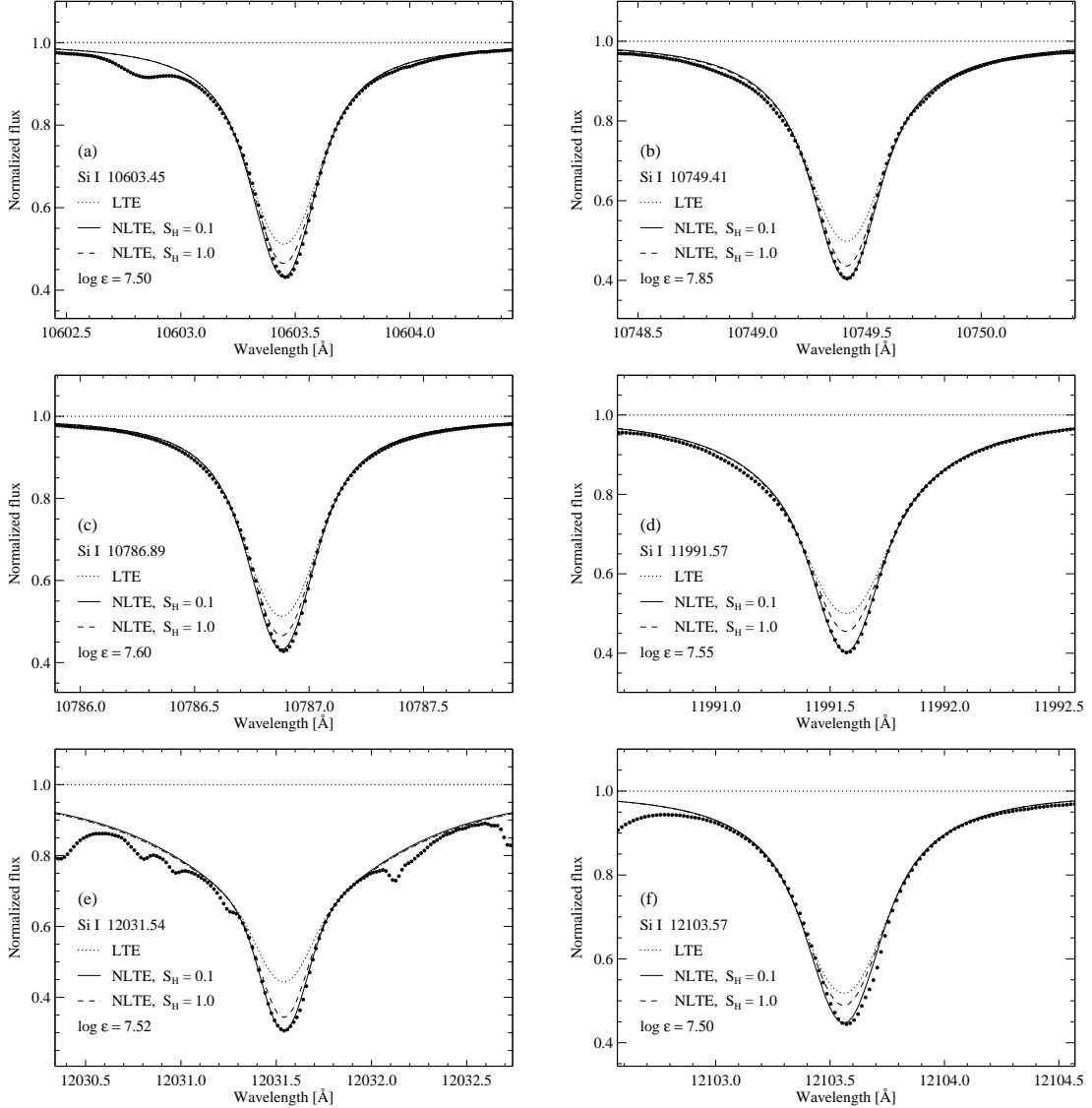


Figure 1: Near-infrared Si1 solar line profiles. NLTE and LTE profiles are calculated for the same abundance, where the NLTE profile with $S_H = 0.1$ refers to the best fit.

All calculations are carried out with a revised version of the DETAIL program [14] using accelerated lambda iteration [20, 21, for details].

4.2 NLTE effects

Fig.2 shows the behavior of the departure coefficients $b_i = n_i^{NLTE}/n_i^{LTE}$ of the important levels of Si1 and Si2 ground state as a function of continuum optical depth (τ_{5000} referring to $\lambda = 5000 \text{ Å}$) in the model atmosphere of HD 19445. Here, n_i^{NLTE} and n_i^{LTE} are the statistical equilibrium and thermal (Saha-Boltzmann) number densities, respectively. We can see that the three lowest levels of Si1 are underpopulated in the deep atmosphere, while the levels $4s^3P^o$ of Si1 and Si2 ground state

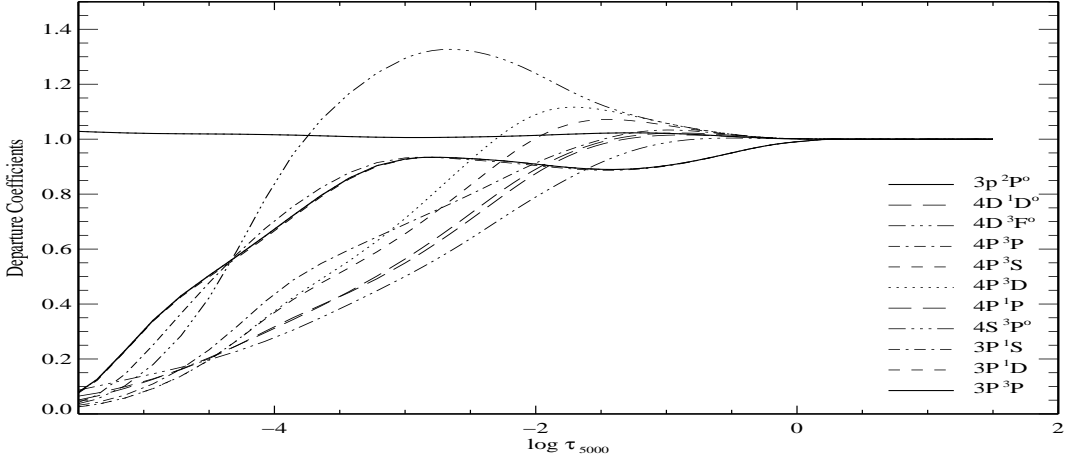


Figure 2: Departure coefficients as a function of $\log \tau$ for selected levels of Si1 and Si2 ground state in the model atmosphere of HD 19445.

are overpopulated in the line formation region, which is due to the ionization cross-sections of the lowest three terms, $3p\ ^3P$, $3p\ ^1D$ and $3p\ ^1S$ are an order of magnitude greater than those of the next terms. It tends to efficiently decouple the metastable terms from the excited ones. The thresholds of the three terms are 1500, 1700 and 2000 Å, respectively [40][Fig.2]. In this wavelength region, the most important continuous absorption is the free-free quasi-molecular absorption and satellites in Ly α due to collisions with H and H $^{+}$ [1], especially for warm metal-poor stars [41, see for details]. As already discussed in [40], there is an unusually large energy gap between the ground state, $3p\ ^3P$, the two metastable terms $3p\ ^1D$ and $3p\ ^1S$, and the first excited levels of neutral silicon. These gaps are about 5, 4, and 3 eV, respectively, and they shift all lines emerging from those levels into the UV, most of them below 2000 Å. Therefore, the interaction of the three most populated Si1 levels with the Si2 ion is completely based on bound-free processes, where photoionization and ionization by electron collisions compete in strength. Due to the large photoionization cross-sections for the three lowest levels, the departure coefficients of Si1 are very sensitive to the UV radiation field. When the Ly α continuum absorption is not included, the extreme underpopulation of Si1 levels in the atmospheres of warm metal-poor stars is clearly seen [41, see Fig.5].

The abundance analyzes of Si1 infrared lines clearly show the NLTE effects. It should be noted that the NLTE effects differ from line to line, the strong 10 585 and 10 827 Å lines show large NLTE effects for our program stars, while the weak lines show the smallest NLTE abundance effects (< 0.02 dex, Table 2). The differences of abundance between LTE and NLTE analyses for the two strong Si1 lines at 10 585 and 10 827 Å are plotted in Fig. 3 as a function of metal abundance, temperature and surface gravity, respectively. There is a trend that the NLTE effects increase with decreasing surface gravity. However, it should be noted that we only include one giant star (HD 122563) in our sample, this trend should be confirmed by more sample stars.

The important uncertainties of the NLTE effects are due to the lack of suitable cross-section data for collisional excitation and ionization by electrons and hydrogen. Of the two, the treatment of the hydrogen collision is the most uncertain. Hydrogen collisions are important and may well

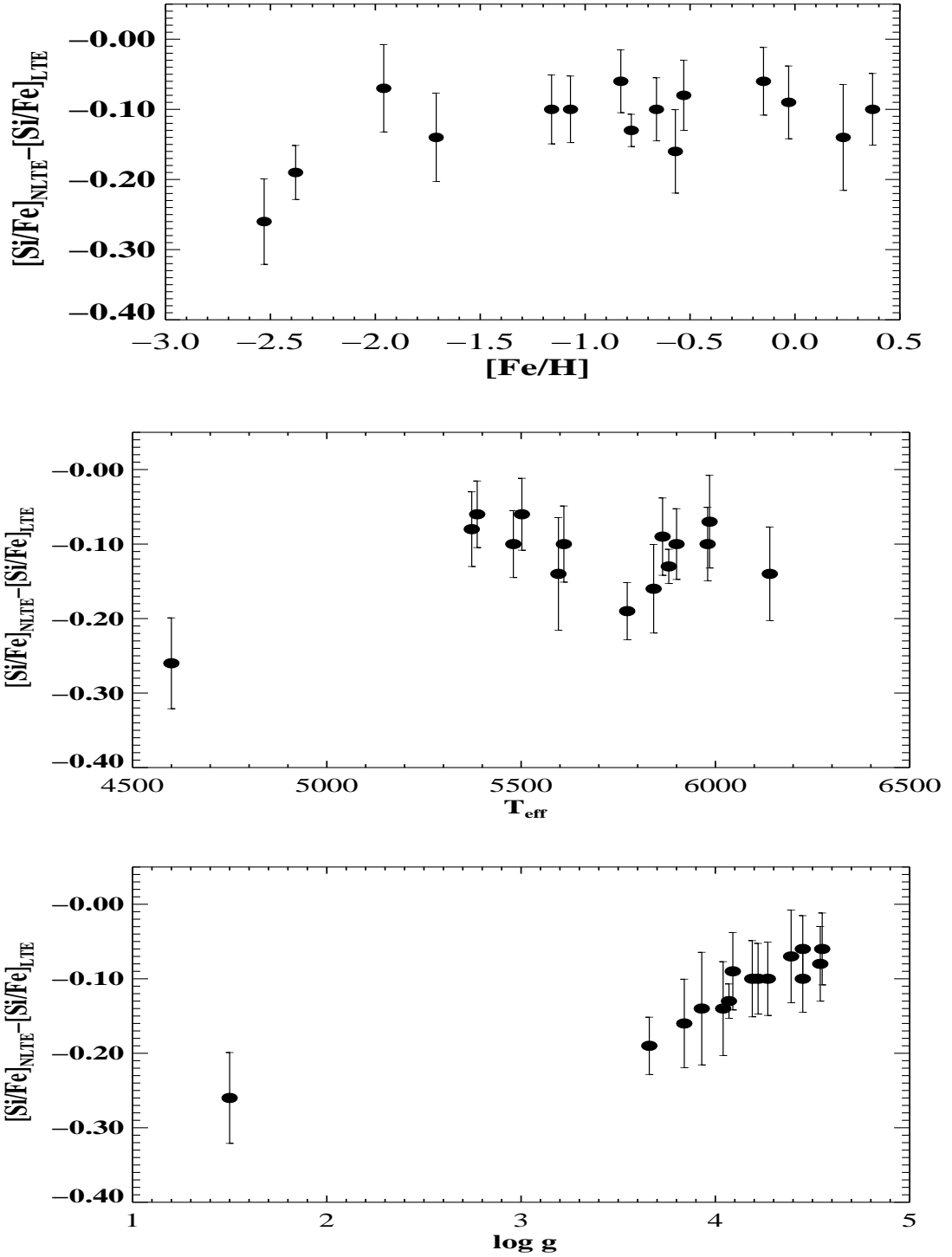


Figure 3: Difference of [Si/Fe] abundance ratios calculated under NLTE and LTE assumptions for the two strong SiI lines (10 585 and 10 827 Å) as a function of metal abundance (a), temperature (b), and surface gravity (c).

dominate the collision rates in hot metal-poor stars [7]. Only limit information on selected transitions in a few elements has so far been gained from laboratory measurements and detailed quantum mechanical calculations. Those results show that the Drawin formula overestimates the inelastic hydrogen collisional cross-sections by one to six orders of magnitude [12, 11, 8]. We apply a scaling factor S_H to the Drawin formula and calibrat it based on solar stellar observations. Fortunately, for Si, as we already discussed in Sect. 4.1, we can determine the S_H scale from the fitting of the strong solar infrared lines. Thus, we estimate that the uncertainties in the NLTE corrections are less than 0.1 dex.

5. Results

5.1 Stellar silicon abundances

The abundance determinations for our program stars are made using spectral synthesis. Some examples of the profile fitting are presented in Fig.4 and Fig.5. Consistent abundance results are obtained between different lines when NLTE effects are included, the final abundance scatter of single lines is between 0.01 and 0.12 for our program stars, while the scatter can reach to 0.3 dex for the extreme case under the LTE situation (See Table2 for details). The derived abundance results based on both the infrared and optical lines are presented in Table 3.

5.2 Comparison with the optical results

We have also been determined the silicon abundances from the optical lines based on LTE and NLTE analyses for these stars [41, 43, 32]. In Fig.6, we compare the [Si/Fe] values determined from infrared and optical lines for our program stars. A comparison of the abundances shows that consistent results are obtained when the NLTE effects included, the differences are less than 0.1 dex for all program stars, while as large as 0.2 dex difference can be found for the LTE results in some cases.

6. Discussion and Conclusions

We have determined silicon abundances for 15 nearby stars, spanning the range $-2.6 < [\text{Fe}/\text{H}] < \sim 0.4$, based on the infrared lines. All abundances are derived from NLTE statistical equilibrium calculations. Fig.7 displays the behaviour of the [Si/Fe] ratio with the metal abundance for all stars considered in this paper. Based on our results we come to the following conclusions:

1. Silicon is overabundant by 0.2-0.3 dex for metal-poor stars, and the LTE results overestimate the Si abundances.
2. The NLTE effects vary with different infrared lines. The weak lines are insensitive to NLTE effects, while the strong lines show large NLTE effects. NLTE leads to enhanced absorption in the line cores and negative abundance corrections over the range of stellar parameters studied here. This effects may depend on the surface gravity, thus tend to be large for giant stars.

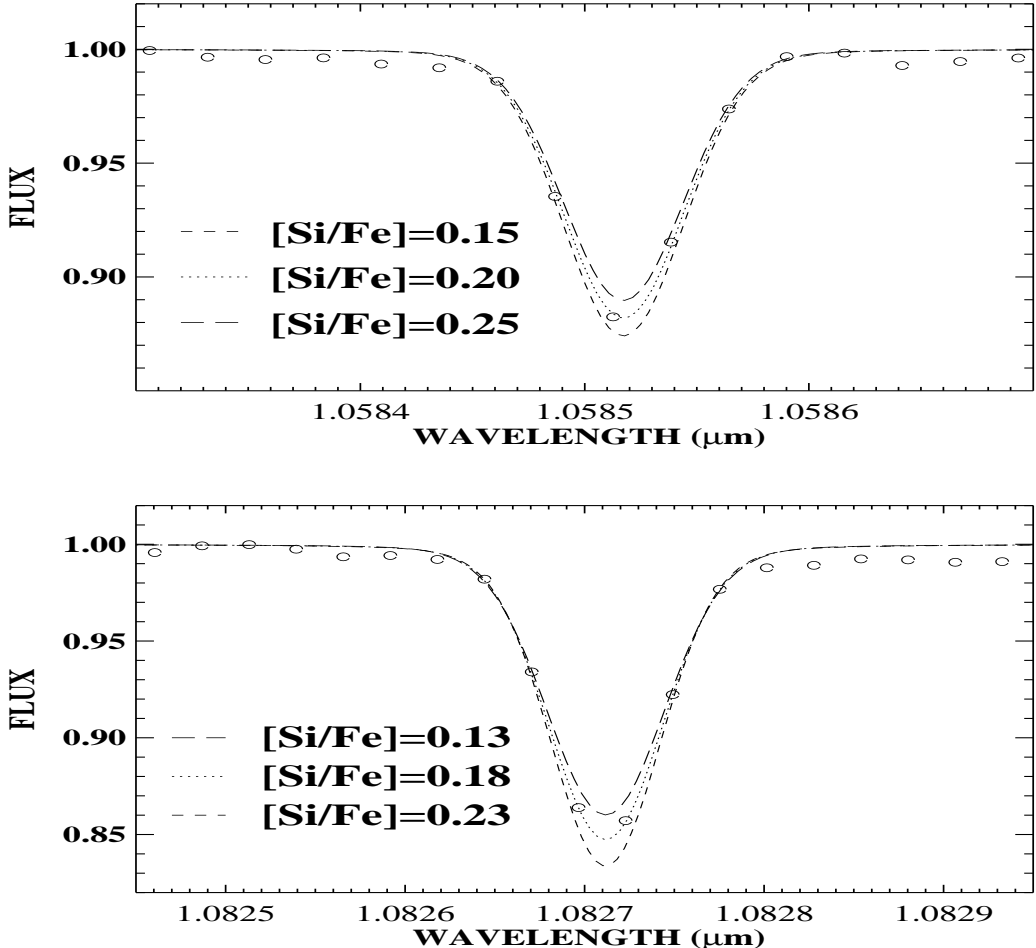


Figure 4: Profile fitting of the Near-infrared Si I lines in the spectrum of our program stars. The open circles are the observational data, the dotted line is the best-fitting synthesis, and the dashed and long dashed lines are synthetic spectra with Si abundances of ± 0.05 dex relative to the best fit.

3. Our results show that NLTE largely removes obvious discrepancies between optical and infrared lines obtained under an LTE assumption.

Thus, it is important to consider the NLTE effects when the silicon abundances determined with the infrared lines.

Prof. H.B. Li and Mr. F. Xiao at Xinglong is thanked for carrying out the service observations. This research was supported by the National Natural Science Foundation of China under grant Nos. 11021504, 10878024, 10973016, 10821061, 10778701 and 11103034, by the foundation of Shandong University at Weihai No. 2010ZRYB003. One of the authors (M. T.-H.) is grateful for a financial support from a Grant-in-Aid for scientific research (C, No. 22540255) from the Japan Society for the Promotion of Science.

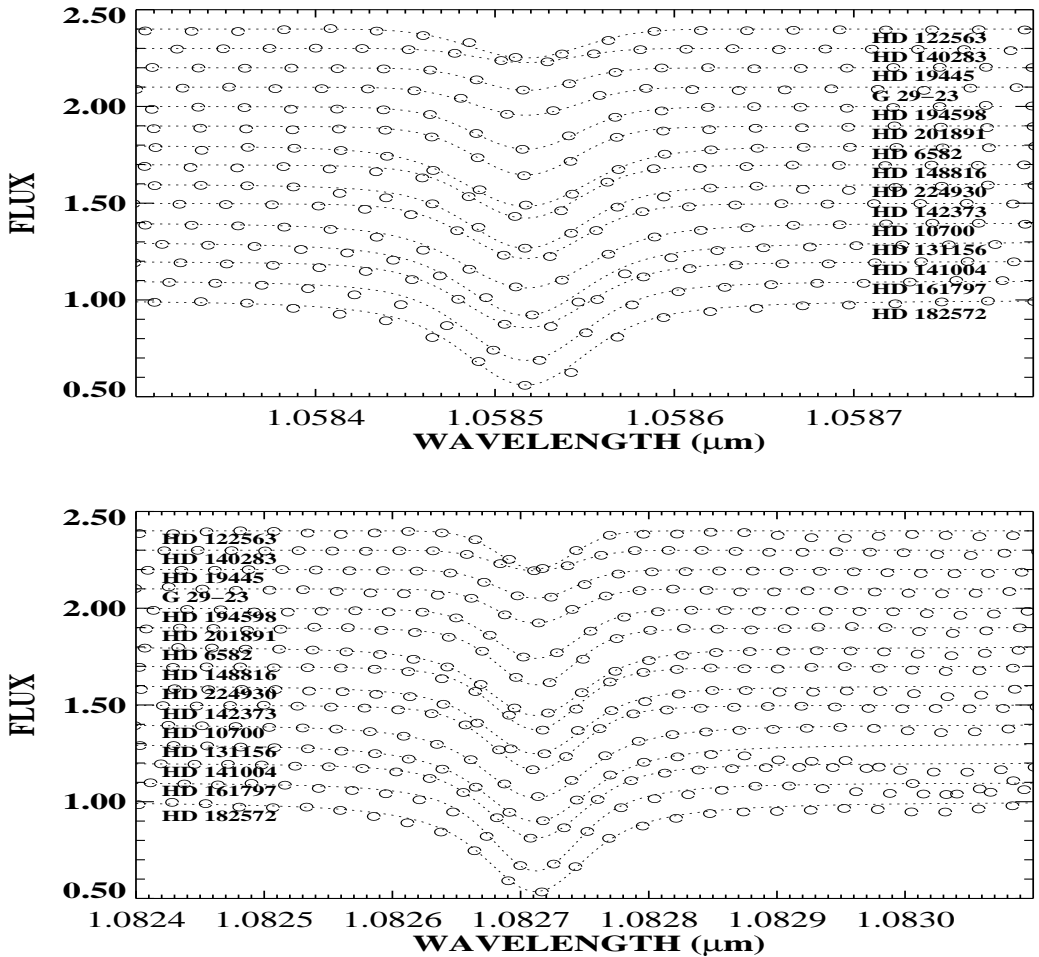


Figure 5: Profile fitting of the Near-infrared SiI lines in the spectrum of our program stars. Observed spectrum - open circles, NLTE profiles - dotted line.

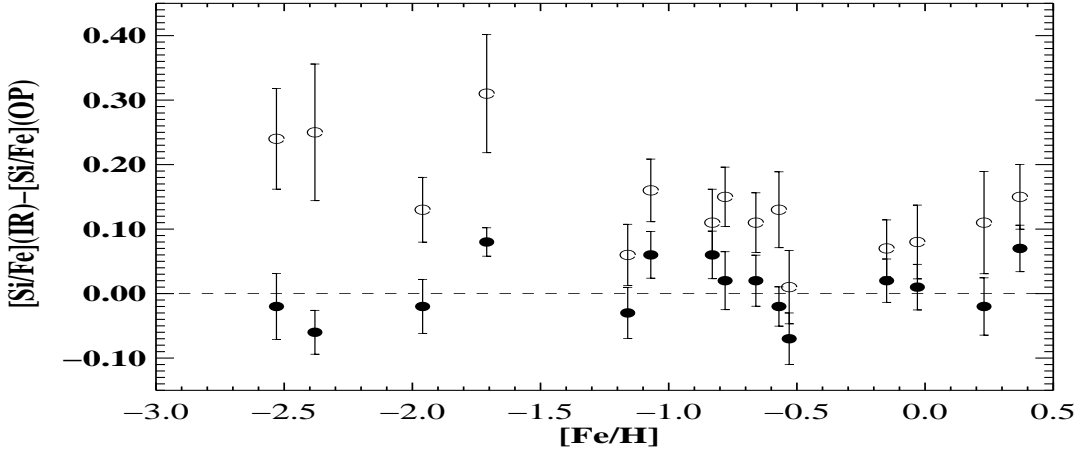


Figure 6: The differences of silicon abundance between the infrared and optical lines. open circles (\circ) are LTE results, while filled circles (\bullet) for NLTE results. It is obviously that the LTE results give large difference between the Si abundances based on optical and infrared lines.

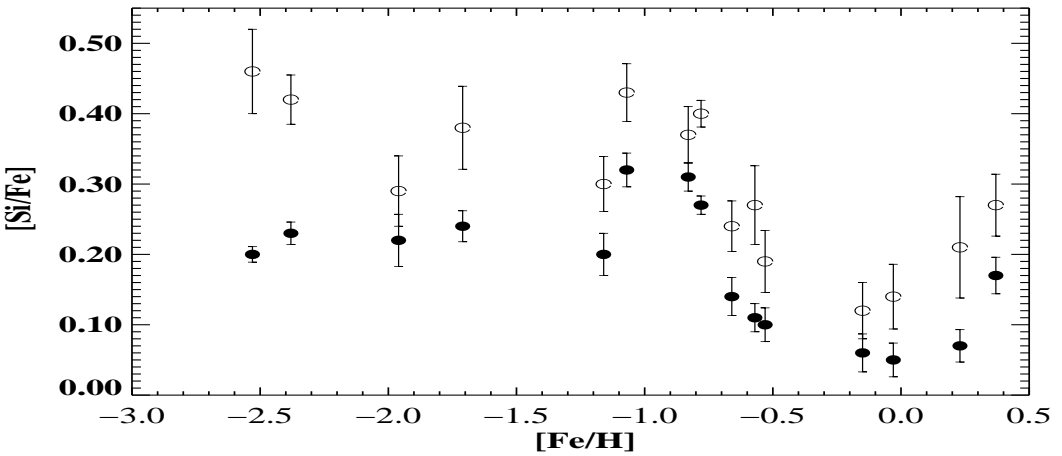


Figure 7: Abundance ratios $[Si/Fe]$ as a function of $[Fe/H]$. Filled circles (\bullet) represent the NLTE results, while open circles (\circ) for LTE results. The LTE results overestimate the Si abundances.

Table 1: Atomic data of silicon infrared lines*.

λ [Å](Air)	Transition	$\log gf$	$\log C_6$	NLTE
10288.90	$4s^3P_0^o - 4p^3S_1$	-1.65	-30.661	-0.02
10371.30	$4s^3P_1^o - 4p^3S_1$	-0.85	-30.659	-0.10
10585.17	$4s^3P_2^o - 4p^3S_1$	-0.14	-30.659	-0.18
10603.45	$4s^3P_1^o - 4p^3P_2$	-0.34	-30.677	-0.09
10627.66	$4p^1P_1 - 4p^3P_2^o$	-0.39	-30.692	-0.15
10661.00	$4s^3P_0^o - 4p^3P_1$	-0.34	-30.687	-0.04
10689.73	$4p^3D_1 - 4d^3F_2^o$	-0.07	-29.964	-0.07
10694.27	$4p^3D_2 - 4d^3F_3^o$	+0.06	-29.944	-0.07
10727.43	$4p^3D_3 - 4d^3F_4^o$	+0.25	-29.907	-0.10
10749.40	$4s^3P_1^o - 4p^3P_1$	-0.20	-30.689	-0.06
10784.57	$4p^3D_2 - 4d^3F_2^o$	-0.69	-29.965	-0.01
10786.88	$4s^3P_1^o - 4p^3P_0$	-0.34	-30.691	-0.05
10827.10	$4s^3P_2^o - 4P^3P_2$	+0.21	-30.677	-0.06
10843.87	$4P^1P_1 - 4d^1D_2^o$	-0.08	-30.145	-0.11
10882.83	$4p^3D_3 - 4d^3F_3^o$	-0.80	-29.945	-0.00
10979.34	$4s^3P_2^o - 4P^3P_1$	-0.55	-30.688	-0.04

* $\log gf$ values have been determined from NLTE solar spectrum fits, and damping constants $\log C_6$ for SiI infrared lines are computed according to the table from [5, 6] and [9].

Table 2: Stellar silicon LTE and NLTE (for each star, the first and the second row, respectively) abundances given relative to the iron LTE abundances derived from the Fe2 lines ([Si/Fe])*.

Name	10 288	10 371	10 585	10 603	10 627	10 661	10 689	10 694	10 727	10 749	10 784	10 786	10 827	10 843	10 882	10 979
G 29-23		0.36	0.46	0.36		0.31			0.41	0.41		0.24	0.46			
		0.27	0.27	0.24		0.23			0.26	0.23		0.20	0.20			
HD 6582	0.30	0.36	0.49	0.38	0.33	0.36	0.38	0.36	0.40	0.39	0.30	0.32	0.46	0.34	0.33	
	0.30	0.32	0.38	0.29	0.28	0.29	0.34	0.31	0.32	0.32	0.30	0.28	0.31	0.27	0.32	
HD 10700	0.10	0.20	0.31	0.13	0.18	0.23	0.20	0.21	0.22	0.20	0.12	0.12	0.22	0.15		
	0.08	0.10	0.12	0.07	0.11	0.12	0.15	0.14	0.11	0.06	0.12	0.07	0.10	0.06		
HD 19445	0.33	0.28	0.24	0.28	0.23		0.23		0.40			0.24	0.36			
	0.28	0.20	0.19	0.26	0.18		0.22		0.28			0.18	0.18			
HD 122563	0.39	0.56	0.44			0.40						0.41	0.53			
	0.21	0.21	0.20			0.20						0.18	0.18			
HD 131156	0.04	0.19	0.24	0.11	0.06	0.16	0.14	0.14	0.11	0.11	0.04	0.11	0.12	0.06	0.10	
	0.02	0.09	0.10	0.05	0.03	0.09	0.09	0.08	0.03	0.03	0.03	0.06	0.08	0.01	0.08	0.08
HD 140283	0.43	0.46	0.36			0.40						0.47				
	0.26	0.22	0.22			0.24						0.21				
HD 141004	0.06	0.19	0.14	0.12	0.09	0.16	0.20	0.20	0.20	0.12	0.03	0.12	0.19	0.19		
	0.05	0.08	0.09	0.06	0.00	0.05	0.06	0.09	0.06	0.02	0.01	0.02	0.08	0.08		
HD 142373	0.12	0.26	0.34	0.26	0.26	0.33	0.32	0.31	0.31	0.26	0.10	0.23	0.36	0.31		
	0.12	0.10	0.14	0.10	0.12	0.12	0.15	0.14	0.11	0.06	0.08	0.06	0.11	0.11		
HD 148816	0.39	0.40	0.36	0.35	0.44	0.41	0.40	0.40	0.40	0.42		0.38	0.40			
	0.27	0.30	0.26	0.28	0.25	0.29	0.26	0.28	0.26	0.26		0.26	0.26			
HD 161797	0.00	0.20	0.31	0.13	0.19	0.26	0.25	0.24	0.29	0.26	0.02	0.20	0.26	0.30		
	0.00	0.05	0.12	0.06	0.06	0.12	0.10	0.06	0.07	0.06	0.02	0.06	0.08	0.06		
HD 182572	0.21	0.35	0.31	0.31	0.26	0.34	0.28	0.26	0.25	0.24	0.18	0.18	0.31	0.24		
	0.21	0.21	0.22	0.16	0.14	0.20	0.19	0.16	0.16	0.16	0.15	0.14	0.14	0.13		
HD 194598	0.31	0.38	0.26	0.24	0.26	0.28	0.30	0.32	0.26		0.29	0.44	0.30			
	0.25	0.16	0.18	0.18	0.18	0.22	0.24	0.21	0.15		0.16	0.23	0.22			
HD 201891	0.46	0.50	0.40	0.39	0.38	0.38	0.46	0.45	0.45	0.38		0.40	0.49			
	0.36	0.31	0.30	0.34	0.31	0.33	0.36	0.35	0.29		0.29	0.30				
HD 224930	0.25	0.35	0.23	0.19	0.21	0.20	0.24	0.30	0.24		0.18	0.25	0.19			
	0.15	0.17	0.13	0.10	0.10	0.15	0.16	0.20	0.13		0.10	0.15	0.10			

* Our NLTE calculations for Fe I/II based on the advanced atomic model [34] support the earlier conclusion of [28] that the NLTE effects for the Fe2 lines are negligible.

Table 3: Stellar silicon LTE and NLTE abundances given relative to the iron LTE abundances derived from the Fe2 lines*.

Name	T_{eff}	$\log g$	[Fe/H]	ξ	[Si I _{LTE} /Fe] (ir)	[Si I _{NLTE} /Fe] (ir)	[Si I _{LTE} /Fe] (opt)	[Si I _{NLTE} /Fe] (opt)
G 29-23	6140	4.04	-1.71	1.50	0.38±0.059	0.24 ± 0.022	0.07±0.07	0.16 ± 0.00
HD 6582	5387	4.45	-0.83	0.89	0.37±0.040	0.31 ± 0.020	0.26±0.033	0.25 ± 0.031
HD 10700	5373	4.54	-0.53	0.80	0.19±0.044	0.10 ± 0.024	0.18±0.036	0.17 ± 0.032
HD 19445	5985	4.39	-1.96	1.50	0.29±0.050	0.22 ± 0.037	0.16±0.005	0.24 ± 0.020
HD 122563	4600	1.50	-2.53	1.90	0.46±0.060	0.20 ± 0.011	0.22±0.05	0.22 ± 0.050
HD 131156	5500	4.55	-0.15	0.80	0.12±0.040	0.06 ± 0.027	0.05±0.019	0.04 ± 0.020
HD 140283	5773	3.66	-2.38	1.50	0.42±0.035	0.23 ± 0.016	0.17±0.10	0.29 ± 0.030
HD 141004	5864	4.09	-0.03	1.05	0.14±0.046	0.05 ± 0.024	0.06±0.034	0.04 ± 0.026
HD 142373	5841	3.84	-0.57	1.24	0.27±0.056	0.11 ± 0.020	0.14±0.018	0.13 ± 0.023
HD 148816	5880	4.07	-0.78	1.20	0.40±0.019	0.27 ± 0.013	0.25±0.042	0.25 ± 0.043
HD 161797	5596	3.93	+0.23	1.17	0.21±0.072	0.07 ± 0.023	0.10±0.033	0.09 ± 0.038
HD 182572	5610	4.19	+0.37	1.01	0.27±0.044	0.17 ± 0.026	0.12±0.024	0.10 ± 0.025
HD 194598	5980	4.27	-1.16	1.60	0.30±0.039	0.20 ± 0.030	0.24±0.027	0.23 ± 0.026
HD 201891	5900	4.22	-1.07	1.20	0.43±0.041	0.32 ± 0.024	0.27±0.026	0.26 ± 0.027
HD 224930	5480	4.45	-0.66	0.90	0.24±0.036	0.14 ± 0.027	0.13±0.029	0.12 ± 0.029

* Our NLTE calculations for Fe I/II based on the advanced atomic model (Mashonkina et al. [34]) support the earlier conclusion of Korn et al. ([28]) that the NLTE effects for the Fe2 lines are negligible.

References

- [1] Allard, N.F., Drira, I., Gerbaldi, M., Koester, D., & Spielfiedel, A. 1998, A&A, 335, 1124.
- [2] Ali, A. W., & Griem, H. R. 1966, Phys. Rev., 144, 366.
- [3] Allen, C. W. 1973, Astrophysical Quantities, 3rd Ed., Athlone Press, London.
- [4] Anders, E., & Grevesse, N. 1989, Geochim. Cosmochim. Acta, 53, 197.
- [5] Anstee, S. D., & O'Mara, B. J. 1991, MNRAS, 253, 549.
- [6] Anstee, S. D., & O'Mara, B. J. 1995, MNRAS, 276, 859.
- [7] Asplund, M. 2005, ARA&A, 43, 381.
- [8] Barklem, P. S., Belyaev, A. K., Spielfiedel, A., Guitou, M., & Feautrier, N. 2012, astroph1203.4877.
- [9] Barklem, P. S., Piskunov, N., & O'Mara, B. J. 2000b, A&AS, 142, 467.
- [10] Baumüller, D., & Gehren, T. 1996, A&A, 307, 961.
- [11] Belyaev, A. K., Barklem, P. S., 2003. Phys. Rev. A, 68, 62703.
- [12] Belyaev, A. K., Grosser, J., Hahne, J., Menzel, T. 1999. Phys. Rev. A, 60, 2151.
- [13] Bergemann, M., & Cescutti, G. 2010 A&A, 522, 9.
- [14] Butler, K., & Giddings, J. Newsletter on the analysis os astronomical spectra No. 9, University of London.
- [15] Dekker, H., Dódorico, S., Kaufer, A., Delabre, B., & Kotzlowski, H. 2000, Proc. SPIE, 4008, 534.
- [16] Drawin, H.W. 1968, Z.Physik 211, 404.
- [17] Drawin, H.W. 1969, Z. Physik 225, 483.
- [18] Fuhrmann, K., Axer, M., & Gehren, T. 1993, A&A, 271, 451.
- [19] Fuhrmann, K., Pfeiffer, M., Frank, C. et al. 1997, A&A, 323, 909.
- [20] Gehren, T., Butler, K., Mashonkina, L., Reetz, J., & Shi, J. R. 2001, A&A, 366, 981.
- [21] Gehren, T., Liang, Y. C., Shi, J. R., Zhang, H. W., & Zhao, G. 2004, A&A, 413, 1045.
- [22] Gehren, T., Shi, J. R., Zhang, H. W., Zhao, G., & Korn, A. J. 2006, A&A, 451, 1065.
- [23] Grupp, F. 2004, A&A 420, 289.
- [24] Iwamoto, K., Brachwitz, F., Nomoto, K., Kishimoto, N., Umeda, H., Hix, W. R., & Thielemann, F.-K. 1999, ApJS, 125, 439.
- [25] Jönsson, H., Ryde, N., Nissen, P. E., Collet, R., Eriksson, K., Asplund, M., & Gustafsson, B. A&A, 2011, 530, 144.
- [26] Kobayashi, N., et al. 2000, Proc. SPIE, 4008, 1056.
- [27] Kobayashi, C., Umeda, H., Nomoto, K., Tominaga, N., & Ohkubo, T., 2006, ApJ, 653, 1145.
- [28] Korn, A., Shi, J. R., & Gehren, T. 2003 A&A, 407, 691.
- [29] Kurucz, R. L. 1979, ApJS, 40, 1.
- [30] Kurucz, R. L. 1992, Rev. Mex. Astron. Astrof. 23, 45.

- [31] Kurucz, R. L., Furenlid, I., Brault, J., et al. 1984, Solar Flux Atlas from 296 to 1300nm, Kitt Peak National Solar Observatory.
- [32] Li, J., Wang, X., Shi, J.R., Gehren, T., & Zhao, G. 2012, in preparation.
- [33] Maeda, K., Röpke, F. K., Fink, M., Hillebrandt, W., Travaglio, C., & Thielemann, F.-K. 2010, ApJ, 712, 624.
- [34] Mashonkina, L., Gehren, T., Shi, J. R., Korn, A., & Gruup, F. 2011, A&A, 528, A87.
- [35] Nahar, S.N., & Pradhan, A. K. 1993, J. Phys. B, 26, 1109.
- [36] Nomoto, K., Iwamoto, K., Nakasato, N., Thielemann, F.-K., Brachwitz, F., Tsujimoto, T., Kubo, Y., & Kishimoto, N. 1997, Nucl. Phys. A, 621, 467c.
- [37] Ohkubo, T., Umeda, H., Maeda, K., Nomoto, K., Suzuki, T., Tsuruta, S., & Rees, M. J. 2006, ApJ, 645, 1352.
- [38] Seaton, M.J. 1962, in Atomic and Molecular Processes, Acad. Press, New York.
- [39] Seaton, M. J., Mihalas, D., & Pradhan, A. K. 1994, MNRAS, 266, 805.
- [40] Shi, J. R., Gehren, T., Butler, K., Mashonkina, L., & Zhao, G. 2008, A&A, 486, 303.
- [41] Shi, J. R., Gehren, T., Mashonkina, L., & Zhao, G. 2009, A&A, 503, 533.
- [42] Shi, J. R., Gehren, T., & Zhao, G. 2004, A&A, 423, 683.
- [43] Shi, J. R., Gehren, T., & Zhao, G. 2011, A&A, 534, A103.
- [44] Steenbock, W., & Holweger, H. 1984, A&A, 130, 319.
- [45] Takeda, Y., & Takada-Hidai, M. 2011a, PASJ, 63, 537.
- [46] Takeda, Y., & Takada-Hidai, M. 2011b, PASJ, 63, 547.
- [47] Thielemann, F. K., Argast, D., Brachwitz, F., Martinez-Pinedo, G., Rauscher, T., Liebend"orfer, M., Mezzacappa, A., H"oflich, P., & Nomoto, K. 2002, ApSS, 281, 25.
- [48] Timmes, F. X., Woosley, S. E., & Weaver, T. A. 1995, ApJS, 98, 617.
- [49] Tokunaga, A. T., et al. 1998, Proc. SPIE, 3354, 512.
- [50] Tsujimoto, T., Nomoto, K., Yoshii, Y., Hashimoto, M., Yanagida, S., & Thielemann, F.-K. 1995, MNRAS, 277, 945.
- [51] van Regemorter, H. 1962, ApJ 136, 906.
- [52] Woosley, S. E., & Weaver, T. A. 1995, ApJS, 101, 181.
- [53] Zhao, G., Butler, K., & Gehren, T. 1998, A&A, 333, 219.

Experimental study of key astrophysical $^{18}\text{Ne}(\alpha, p)^{21}\text{Na}$ reaction

L.Y. Zhang^{1,2,3*}, J.J. He¹, S.W. Xu¹, H. Yamaguchi⁴, S. Kubono⁴, Y. Wakabayashi⁵,
S.Z. Chen^{1,2}, J. Hu¹, P. Ma¹, Y. Togano⁶, T. Hashimoto⁴, D. Kahl⁴, T. Teranishi⁷,
R.F. Chen¹, H.W. Wang⁸, W.D. Tian⁸, B. Guo⁹, S. Hayakawa⁴, N. Iwasa¹⁰,
T. Yamada¹⁰, and T. Komatsubara¹¹

¹*Institute of Modern Physics, CAS, Lanzhou, China*

²*University of Chinese Academy of Sciences, Beijing, China*

³*Lanzhou University, Lanzhou, China*

⁴*Center for Nuclear Study (CNS), University of Tokyo, Japan*

⁵*Advanced Science Research Center, JAEA, Japan*

⁶*RIKEN, 2-1 Hirosawa, Wako, Saitama, Japan*

⁷*Department of Physics, University of Kyushu, Japan*

⁸*Shanghai Institute of Applied Physics, CAS, China*

⁹*China Institute of Atomic Energy (CIAE), Beijing, China*

¹⁰*Department of Physics, University of Tohoku, Japan*

¹¹*Department of Physics, University of Tsukuba, Japan*

Key Issues of Elements Synthesis in Cosmos

December, 2012

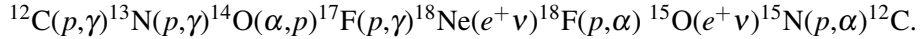
Beijing, China

*Corresponding author.

Explosive hydrogen burning is thought to be the main source of energy generation and a source of nucleosynthesis in X-ray burst and nova[3, 4]. In X-ray burst, for example, at the typical temperature of 0.4-2 GK, the hydrogen burning occurs in the hot CNO cycle:



while the $^{13}\text{N}(e^+ v)^{13}\text{C}$ reaction in the CNO cycle is bypassed by the $^{13}\text{N}(p, \gamma)^{14}\text{O}$ reaction. With the progress of compressing and exothermic nuclear reactions, the temperature of the accretion disk increases. When the temperature reaches about 0.4 GK, the second hot CNO cycle becomes dominant:



It is predicted[3, 4] that the ^{18}Ne waiting point in the second hot CNO cycle can be bypassed by the $^{18}\text{Ne}(\alpha, p)^{21}\text{Na}$ reaction at $T \sim 0.6$ GK, and subsequently, the reaction chain breaks out to the r -process. Hence it is very important to study this reaction rate which is not well understood by so far[1].

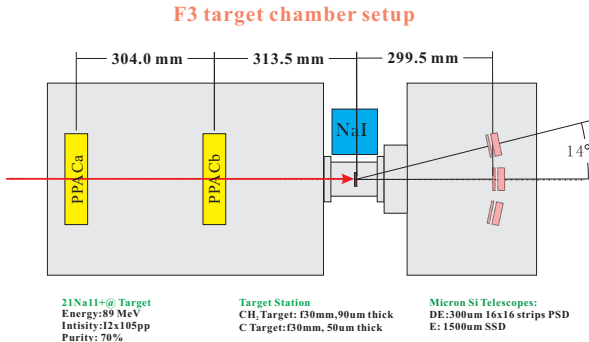


Figure 1: Schematic view of the detector setup.

A nuclear astrophysics experiment was performed at CRIB (CNS Radioactive-Ion Beam separator) in March 2011. An 89 MeV ^{21}Na radioactive beam separated by CRIB bombarded a $93\text{ }\mu\text{m}$ thick polyethylene target (CH_2) with an average intensity of about 2×10^5 pps and a purity of about 70%. As shown in Fig. 1, we utilized two PPACs for measuring the beam counts and directions, and three sets of ΔE -E silicon telescopes for measuring the energies and scattering angles of the recoiled light particles. Fig. 2 shows the typical particle identification plots. ΔE and E signals were measured by the silicon telescopes; TOF were determined by the time of flight between PPACa and ΔE . ΔE -E method identifies those higher energy particles, while the E-TOF method identifies those lower energy ones stopped in the ΔE detector. A NaI array surrounded the chamber in order to detect the decay γ -rays. Several runs with a carbon target were performed for C background subtraction.

The resonant properties (such as J^π, Γ_α , and Γ_p) of the compound ^{22}Mg nucleus were studied by measuring the $^{21}\text{Na}+p$ resonant elastic-scattering differential cross sections. In this study, we mainly focused on the 8.51 and 8.61 MeV resonate states in the compound ^{22}Mg nucleus. In a previous similar experiment[1], we tentatively made the spin-parity assignments for these two states. We think this new experiment can confirm these assignments with much better statistics.

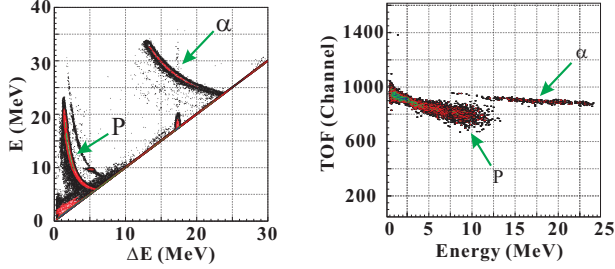


Figure 2: PID plots of ΔE - E and E -TOF methods. The start TOF signal is given by the PPACa, and the stop signal is given by the ΔE detector.

Fig. 3 shows the preliminary R -matrix fitting of the c.m. differential cross section for the resonant elastic scattering of $^{21}\text{Na}+p$ measured at $\theta_{c.m.} \approx 175^\circ$. Those levels colored red in Fig. 3 refer to the ones which have the new spin-parity assignments based on present analysis. Further data analysis is still in progress.

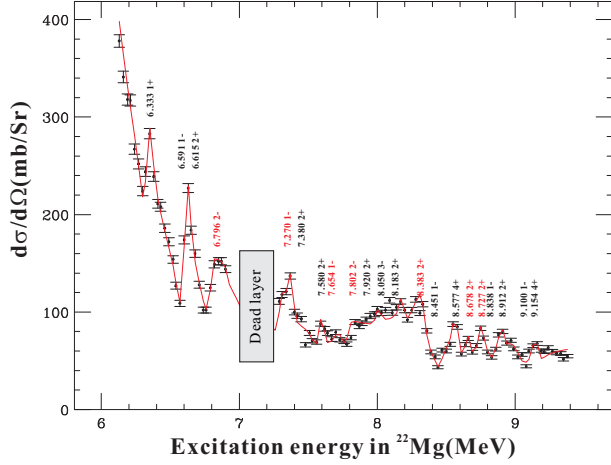


Figure 3: Proton spectrum and preliminary R -matrix fitting result.

References

- [1] J.J. He, *et al.*, Phys. Rev. C **80** (2009) 015801.
- [2] W. Bradfield-Smith, *et al.*, Phys. Rev. C **59** (1999) 3402.
- [3] A. E. Champagne and M. Wiescher, Annu. Rev. Nucl. Part. Sci. **42** (1992) 39.
- [4] M. Wiescher, *et al.*, J. Phys. G: Nucl. Part. Phys. **25** (1999) R133.

群体负责人：柳卫平

群体成员： 李志宏 白希祥 陈永寿

王友宝 唐晓东 施建荣

何建军 郭 冰 连 钢